Utilization of Predictive Analytics & Constrained Metaheuristics to Achieve Optimal Operation of a Liquid-fueled Industrial Process Heater

by

Cody L Prodaniuk

A thesis
presented to the University of Waterloo
in fulfilment of the
thesis requirement for the degree of
Master of Applied Science
in
Mechanical Engineering

Waterloo, Ontario, Canada, 2015

I hereby declare that I am the sole author of this thesis. This is a true copy of the thesis, including any required final revisions, as accepted by my examiners.

I understand that my thesis may be made electronically available to the public.

Cody L Prodaniuk

Abstract

The operation of industrial combustion devices to improve fuel efficiency and reduce emissions, is necessary in many respects. Increasingly stringent environmental regulations and the present volatility of the price of fossil fuels make it necessary to control a combustion device at an optimal operating point while accounting for changes in the environment, heater load, and fuel quality.

In this study, an adaptive and predictive optimal control methodology is developed and tested on a 2.05 MW diesel fueled oilfield process heater. To date, the majority of previous developments and control methodologies have focused on combustion devices either a magnitude larger or smaller, or on gaseous-fueled combustion processes. The present work, which focuses on maximizing the thermodynamic efficiency of an oilfield process heater, is divided into two parts; the first of which is the development of an algorithm that continually regulates and predicts the operating state. The algorithm is comprised of three iterative components: (a) an artificial neural network for adaptivity and prediction; (b) a genetic algorithm for optimization; and (c) a refinement of the search space to complement and restrict the other components. The second part of this work is the physical implementation of the sensors, actuators, and computing hardware necessary for the algorithm. Several challenges encountered during the implementation on the experimental apparatus are discussed, namely involving the diesel flow rate sensor and the actuator for modulating the damper position.

Two experiments were performed, and data were collected and evaluated offline. The first experiment was to initially evaluate performance of the control methodology, and the second was to evaluate the iterative and refinement capabilities of the algorithm. The algorithm optimizes the operating state of the heater and the results agreed with observed trends discovered through the experimentation. Additionally it was discovered that there is a correlation between the optimal operating state and increases to the quantity of heat transferred to the process fluid flowing through the inner coil.

Acknowledgements

To begin with, I owe more than I can express to my supervisor Dr. Kyle J. Daun. Without his encouragement and interminable patience throughout this arduous process (for both of us), I am certain that I would have never completed this work. You have a gift for peering into my chaotic and analphabetic writing style and instilling coherency and even excellence. You helped me overcome my fear of code, complex mathematics, and matrices; something I thought impossible.

I also owe an equal level of gratitude to Garett Cupples, without whose relentless drive to innovate and maintain the role of GenTex Oilfield Manufacturing Inc. as a global leader, this project would not have existed. You have taught me much personally, most keenly (and with fondness) to keep my explanations short.

Throughout these past years working with GenTex, I would like to express my appreciation to Gary Craig and Paul Vandenberk for their aid as this project developed and grew. As well, a thank you to Nima Mohajerin, a fellow graduate student, for his aid in resolving a particularly vexing issue with neural networks.

My gratitude is also extended to my committee members, Dr. Steven L. Waslander and Dr. Serhiy Yarusevych, for scrutinizing my work. Their input and comments are greatly appreciated.

For both my parents Lyle and Laurie, their love and support as I was growing up is beyond any worth I can think of. No one could have asked for better parents. As well, a thank you to my sister Nickole, for not just sharing her home (and cat) with us but for being one of the supporting pillars that has kept me balanced over the years.

While I do not have an endless supply of friends to thank, I want to mention Brian Kettlewell and David Wong as two who have provided a great amount of support and impact to my life as I completed my degrees.

Finally, the generous support of the Natural Sciences and Engineering Research Council of Canada (NSERC) and GenTex Oilfield Manufacturing Inc. is gratefully acknowledged.

Dedication

To the love of my life, my girlfriend Vasti Stephany Montiel, for the commendable (and necessary) ability to put up with me these past (almost) five years. You contributed and gave up more towards the pursuit of this work of knowledge than anyone.

Remember to look up at the stars and not down at your feet. Never give up work. Work gives you meaning and purpose and life is empty without it. If you are lucky enough to find love, remember it is there and don't throw it away.

- Stephen Hawking

Table of Contents

List of Figures

List of Tables

Chapter 1

Introduction

The burning of fossil fuel is vitally important to industrial processes that rely upon combustion to generate mechanical or electrical power or energy in the form of heat. Despite recent drops in the price of oil, long term fuel prices are expected to increase globally; this, together with growing concerns about the impact of fossil fuel combustion on human health and the environment, have motivated improvements in the operation of industrial combustion devices. These improvements have focused on increasing thermodynamic efficiency [1], minimizing harmful environmental emissions [2], [3] or reducing negative combustion dynamics [4]; for example, to ensure stable operation of gas turbines near the lean limit of combustion. At present, there are two distinct strategies to accomplish these goals:

(a) Altering the physical setup of a combustion device encompassing changes to the size and shape of the combustion chamber [5], fuel utilized, or method for fuel introduction [6] and [7], and composition of combustion air including the use of technologies like exhaust/flue gas recirculation [8] and [9], among others.

(b) Altering the controllable operating state(s) of a combustion device encompassing changes made with or without the feedback of relevant information [4], [10], [11].

This thesis is concerned solely with the second of these two strategies, namely the control of an industrial process heater in order to seek an optimal operating point of the process heater.

1.1 Control Classification

Control within the context of an engineering process or system can be thought of as a methodology to affect a desired response within a system by altering one or more inputs [12]. This tacitly assumes an input-output and cause-effect relationship within these systems which may not always be accurate or apparent in complex or physical processes [12]. In all cases, the control of a process or system requires, at minimum, determinable input and output states, and an optional measurement of the process, or part thereof, to assess system performance.

Control methodologies are classically separated into two categories, typically: *open-loop* and *closed-loop* methods. Within *closed-loop* control, there is a feedback mechanism whereby the process is measured and compared to the desired result. The input is then altered from the feedback of information arising from the comparison (*open-loop* control lacks this feedback mechanism). Classic signal diagrams of both open- and closed-loop control can be seen in Figure 1.1. *Closed-loop* control may be further categorized into *online* or *offline* schemas. *Offline control* entails a large temporal delay in the feedback mechanism, while *online* control entails a temporal delay on the order of magnitude of the process itself. A physical system, or mathematical representation thereof, to control is first needed to implement any of these control classifications.

1.2 Physical Process Heater

The industrial process heater used throughout this study is a 70M TEXHEATER, designed and manufactured by GenTex Oilfield Manufacturing Inc. ('GenTex') located in Red Deer, Alberta, Canada. These process heaters support a varied set of oilfield activities including heating fluids used for fracturization (*i.e.*, "fracking") and oil well stimulation.

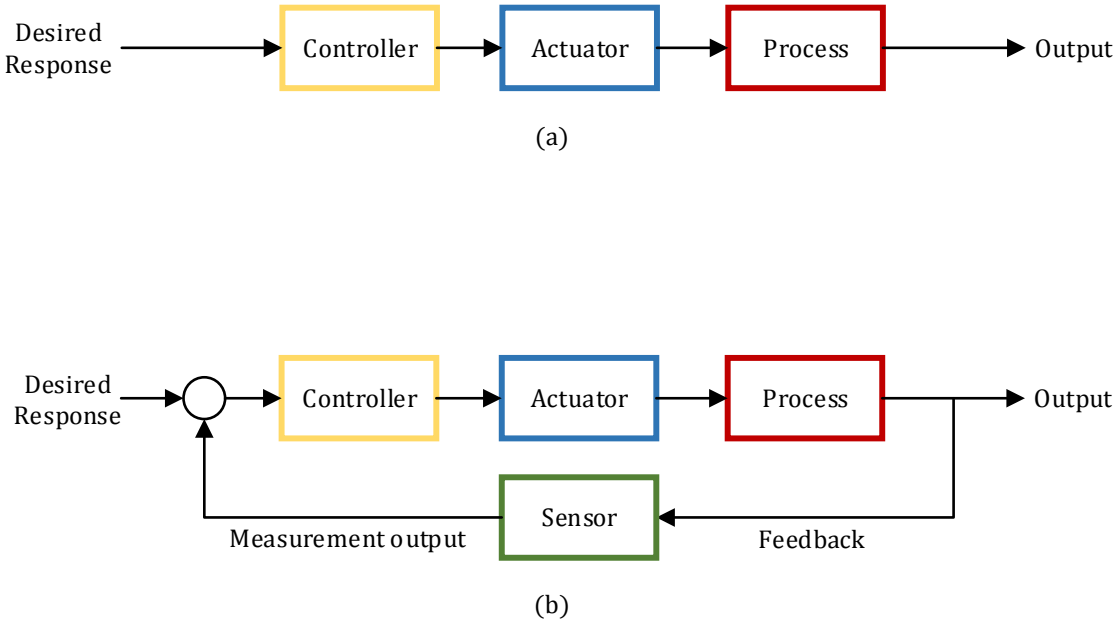

FIGURE 1.1: Classic representations for (a) open and (b) closed-loop control.

The diesel-fueled 70M heating unit, shown in Figure 1.2 with supporting systems, piping, and valving, has a theoretical maximum thermal output of 2.051 MW (7.0×10^6 BTU/hr). A section view of the process heater is shown in Figure 1.3. The heater itself consists of three interconnected coils through which the process fluid flows; the outer and inner coils are concentric while the intermediate coil is slightly staggered. The burner-assembly consists of a Y-type atomizer, fixed-vanes for inducing swirling of the airflow/flame, and various other surfaces to control the input of combustion air flow.

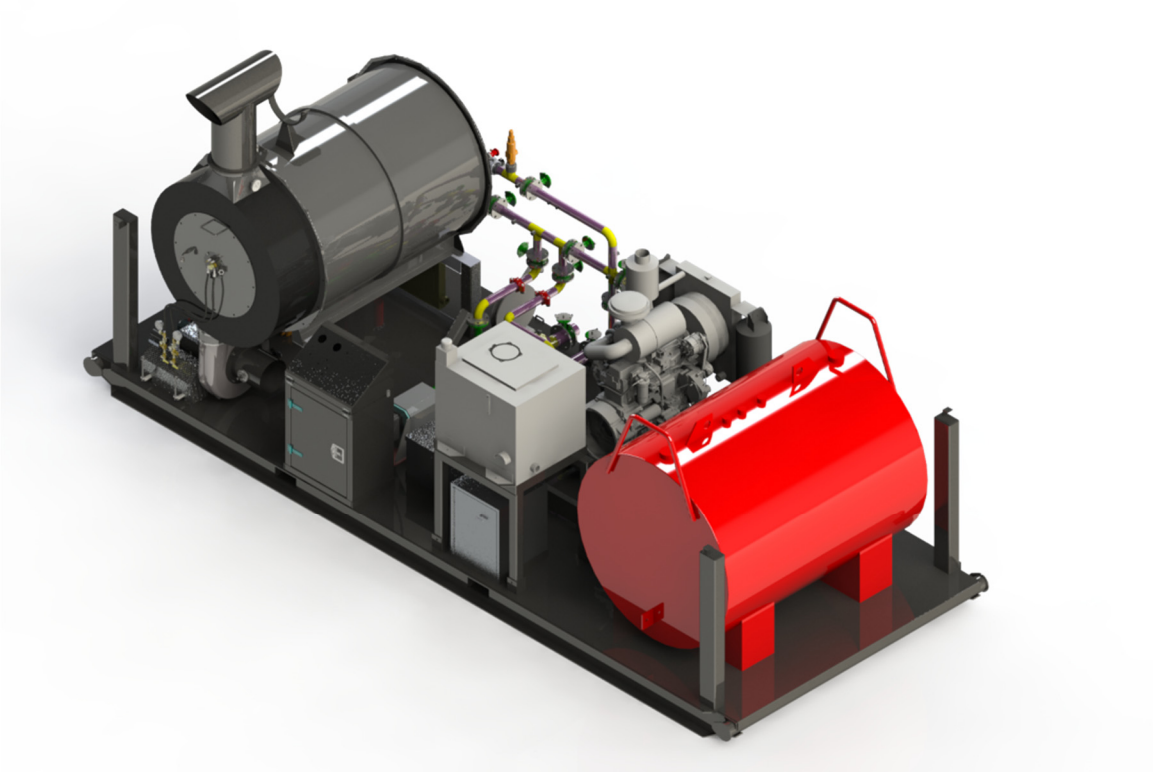

FIGURE 1.2: Rendering of a skid-mounted 70M heating unit.

In a Y-type atomizer, the liquid to be atomized flows through a tube while a high pressure gas (in this case dry compressed air) flows through a passage annular to the tube. At the end of the main tube, the fuel and air passages are subdivided into smaller passages that transect to form mixing chambers; the high kinetic energy of the atomizing gas, combined with the increased shear present in the liquid as it is forced through a smaller passage, breaks up or "atomizes" the liquid into small droplets [13]. The geometry of the atomizer and the supply pressure/flow rates of the fluids controls the patternization and droplet diameter of the liquid fuel [13]. One port on a Y-type atomizer nozzle is illustrated in Figure 1.4.

The process fluid flows sequentially through the outer, intermediate, and inner coils, and then exits the heater. Pumping of the process fluid is typically achieved using a centrifugal or reciprocating triple plunger positive displacement or 'triplex' pump.

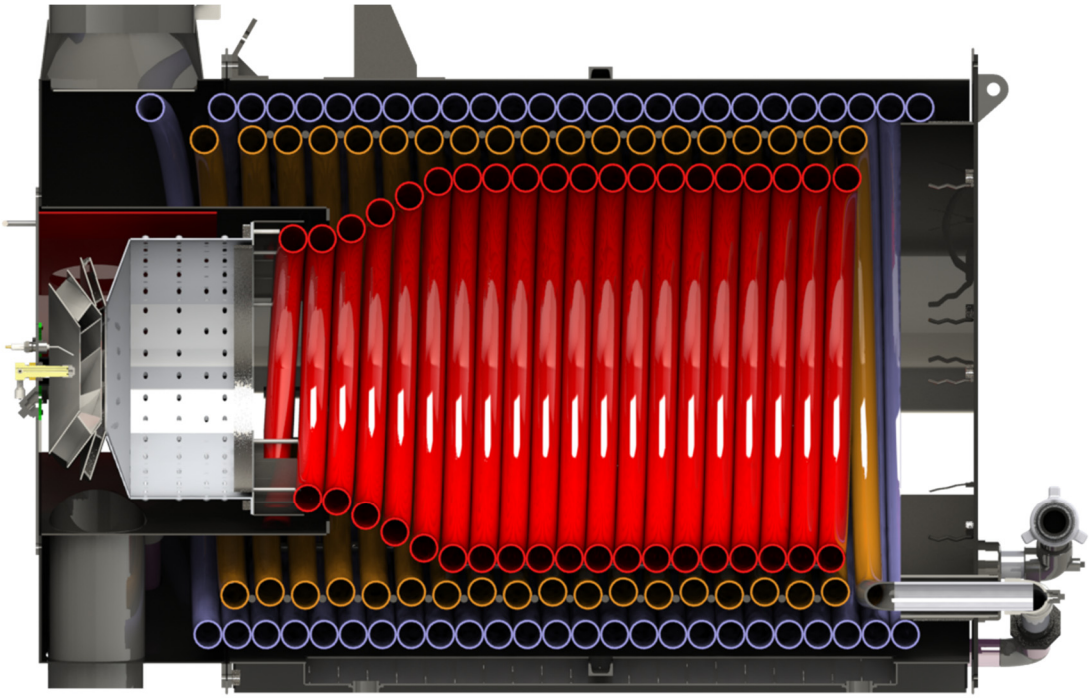

FIGURE 1.3: Rendered section view of a 70M process heater.

A horizontally-fired burner assembly generates a luminous flame within the innermost coil. Make-up combustion air (*i.e.,* combustion air) is provided via a blower fan unit. The hot combustion gases impinge on a refractory surface opposite to the burner, which redirects the gases through an annular passage between the outer and inner coils and over the staggered intermediate coil loop. The combustion gases exit through a stack at the top of the heater to the atmosphere. A complete flow diagram of the process heater is provided in Figure 1.5.

1.3 Operation of the Process Heater

Prior to the beginning of this study, operation of the heating units was entirely manual. The human operator would increase the flow rate of the process fluid above a pre-set minimum flow rate and pressure, and, upon meeting these criteria, the operator would initiate combustion and begin heating.

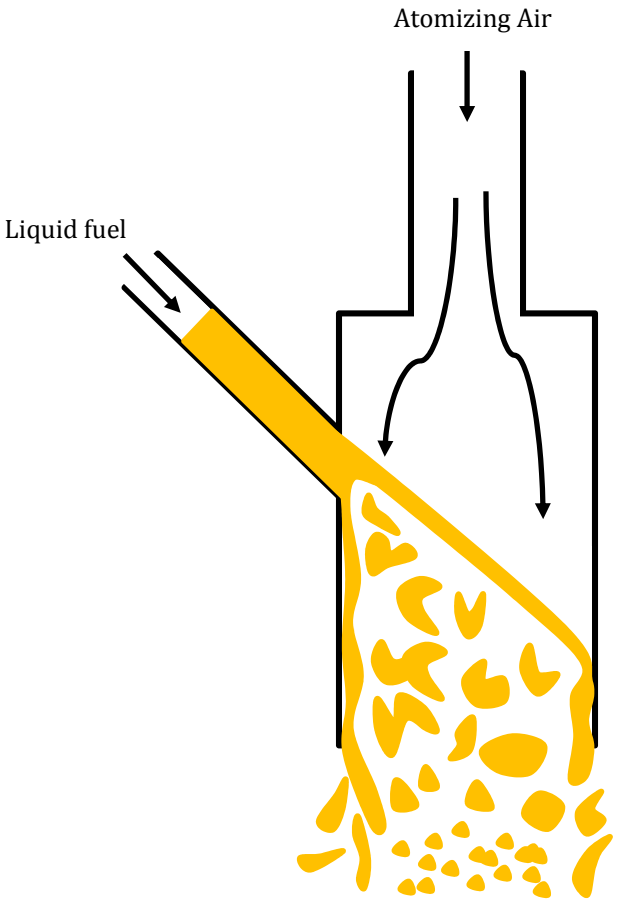

FIGURE 1.4: Y-type atomizer operation, a single port of a typical nozzle [13].

The process heaters are controlled by adjusting three manual inputs: (a) regulation of air pressure into the atomizer through a rotary needle valve; (b) regulation of fuel pressure into the atomizer through a rotary needle valve; and (c) regulation of the combustion air mass flow via the angular position of a damper attached to the inlet of the blower fan. Both the diesel fuel pump and atomizing air compressor pressures are set to maintain preset maximum supply pressures into the needle valves. The blower fan operates at a preset rotational speed.

Combustion control was accomplished by setting the fuel and air pressure for the atomizer to pre-determined recommended set points depending upon the required heating load, and adjusting the damper angular position to an

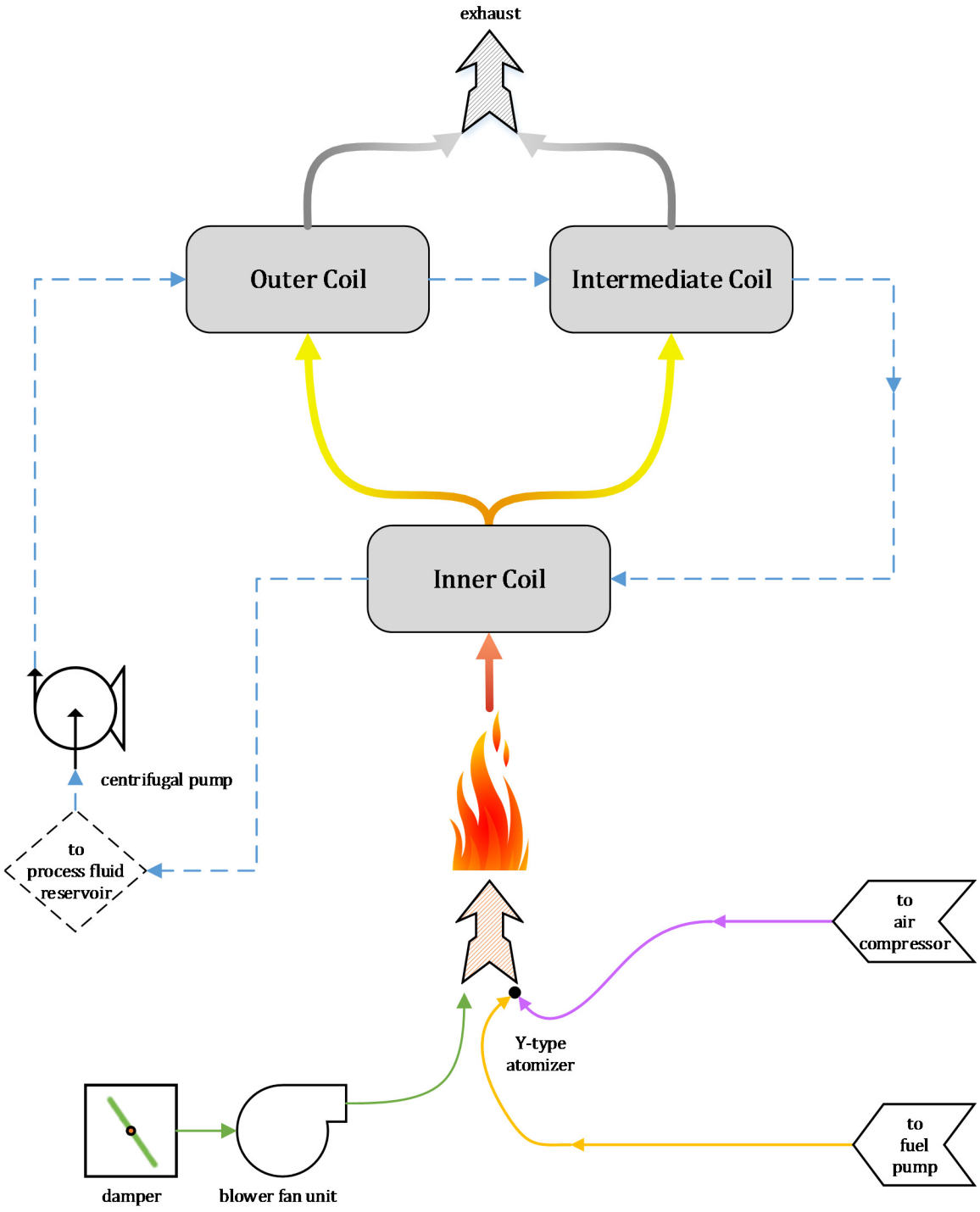

FIGURE 1.5: 70M heating unit process flow diagram.

approximate stoichiometric operating point as visually indicated by the disappearance of soot from the exhaust gases leaving the heater.

1.4 Objectives

This study began with the interest of GenTex in upgrading their existing instrumentation on their production heating units after an experimental unit had been developed with digital controls. This included upgrading from analog mechanical gauges for pressure and temperature to a completely digital system with: a programmable logic controller (PLC); human-machine-interface (HMI) or screen; and sensors to measure temperature, pressure, and flow. The plan was to remove all manual controls for fuel and atomizing air-pressure and damper position and implement them digitally on the human-machine-interface. This centralized-digital-control (CDC) upgrade project was the first-of-its-kind for any oilfield process heater.

The research described in this thesis aims to pioneer a disruptive solution that exploits the in-development CDC system to minimize operator involvement and automatically control the process heater to maximize thermal efficiency and/or minimize pollutant emissions. Building on existing industrial combustion control methodologies, this additional 'layer' of control was to be adaptive to changing environmental conditions and the ever-changing formulations of diesel fuel which varies both seasonally and by supplier.

Within the context of industrial combustion, control methodologies vary from single pre-set control states, to sophisticated and integrated control systems, both with and without feedback mechanisms. One of the most rudimentary ways of achieving a 'good' operating state involves a human operator manually adjusting the operating parameters, usually in a heuristic way, based on the observation of sensor data combined with the operator's experience. Past-operation of GenTex process heating units were operated in this manner. This can be considered an *online* method of control as data gathering and control changes occur virtually

simultaneously with combustion. It also can be considered a pseudo-closed-loop control method as the human operator observes and responds to changes in the operating state in such a way that reinforces positive changes (*e.g.,* an increase in heat output) and counteracts negative changes (*e.g.,* an unstable or sooty flame) [12]. With this simple, human operator-based control, however, the optimal operating point is discovered by accident, or by enumerating all possible operating states. Thus, this method usually results in suboptimal performance, and often regresses to an open-loop control state since an intuitive "feel" of the complex combustion physics is elusive.

An alternative optimization method for combustor operation requires collection of operating data through extensive testing, usually through univariate parametric studies, and then offline post-processing of the gathered data to determine the optimal operating point. Unfortunately, these conclusions usually apply to a specific set of operating conditions and ignore changes that occur in the period of time between data collection and analysis, such as environment (air temperature, humidity), fuel composition, and combustion load. Consequently, there is a need for a control system that can make real-time adjustments to combustor performance to ensure that the device remains near an optimal operating state at all times and in all situations. This thesis focuses on the development, implementation, and testing of such a system through the use of an online predictive optimal control methodology.

Intending to be an evolution from the CDC system, this methodology has two defined objectives/steps:

(a) Implement automated control of the process heater to simplify and reduce operator involvement.

(b) Design and test an adaptive algorithm capable of optimizing the performance (*e.g.,* thermal efficiency) of the process heater.

1.5 Organization of Thesis

The remainder of this thesis is divided into four main chapters.

Chapter 2 is a survey of relevant scientific literature related to the control methodology and experimental apparatus. The chapter is subdivided according to the several aspects that comprise the predictive and optimal algorithm as well as the present-day technologies surrounding the setup of the experimental heating unit.

With the existing and present day state-of-the-art established, Chapter 3 focuses on the physical experimental setup of the process heating unit. Sensor, actuation, computational, and human interface technologies, the four primary components necessary to implement a control experiment, are discussed. Additional safety related features implemented on the heating unit are also included in this section.

Chapter 4 focusses on the general methodology of the predictive-optimal algorithm. The use of neural networks and genetic algorithms and a search-refinement method are presented and discussed. The overall theories of operation and combination together of these methods are examined and presented.

Chapter 5 describes the results of two specific test cases: offline testing of the algorithm from collected data, and partial online testing of the predictive-optimal control methodology. A discussion of these results follows, with operational trends and conclusions derived from the sensor data about the effects of the control algorithm upon combustion and heat transfer to the process fluid.

Finally, Chapter 6 summarizes the outcomes of this study and contains general conclusions arising from this work. More importantly, suggestions for future research with similar opportunities or industrial partnerships is discussed.

1.6 Closure

The thesis and containing subject matter was introduced. An overview of the heating unit and heater itself was discussed with a brief overview of the manual control methodology prior to the beginning of this study. The main objectives of this thesis were also introduced.

Chapter 2

Literature Review

2.1 Introduction

Much has been written about control of industrial combustion and related technologies, both in a research setting and in engineering applications. The majority of these contributions can be categorized as: (a) premixed, gaseous fuel combustors, (b) of laboratory-scale ($<$ 100 kW), (c) power generation-scale ($>$ 100 MW) applications, or (d) internal combustion (IC) engines. The experimental heating unit used within this work is outside of these specific categories, and, accordingly, literature pertaining to the control of these types of combustors is sparse. Nevertheless, past work from the above categories can provide a relevant and valuable insight into the present application; the following text will delve, as needed, into these areas.

2.2 Combustion Control Classification

This section provides a brief overview of the classification of combustion control and the differentiating factors between each class. These classifications are inclusive but otherwise separate from the earlier defined open- and closed-loop control methodologies. Docquier and Candel [11], through their thorough summary of other works in the combustion control field, categorize combustion control into three broad areas: operating point control, active combustion enhancement, and active instability control. Each of these classifications is differentiated based upon the level of control involvement as well as the intended outcome of the control strategy.

Table 2.1 summarizes the typical operating state variables (*i.e.,* the variable or operating setting to be modified/controlled) as well as the typical performance index (*i.e.,* the objective to be measured and/or optimized) for both active instability control and active combustion enhancement. Variables p', q', p', X', T', $\bar{X}$, and $\bar{T}$ are, respectively, the pressure and heat release fluctuations, fluctuations of mole fractions, mean mole fraction, and mean temperature. The control classification and variable summary presented in Table 2.1 is not collectively exhaustive of the spectrum of state variables and performance indices used in combustion control. It does, however, differentiate the two active control classifications and presents a starting point for what are 'typical' controlled/state variables and performance indices for each classification.

TABLE 2.1: Control classification summary by variable [11].

Active control classification	State Variables	Performance Index
Instability Control	p' , q'	$\overline{p'^2}$, $\overline{q'^2}$, $\overline{p'q'}$
Combustion Enhancement	X' , T'	$\bar{X}$, $\bar{T}$, $\overline{X'^2}$, $\overline{T'^2}$

2.2.1 Operating point control

Operating point control is the most common of the three control classifications. Operating point control can be defined by the individual preset control points or states that are altered to achieve a specific outcome. For example, within an extremely basic single-input single-output (SISO) combustion control system, the adjustment of the quantity of fuel, an input, affects the equivalence ratio, an output. Other examples of this type of control for internal combustion engines and gas turbines are provided in [11] and [4], respectively.

Operating point control does not exclude the use of sensor feedback, although, classically, this technique is an open-loop control method. Closed-loop control methodologies use sensor information into a feedback loop to improve the stability, regulation, and the temporal response of the controlled system [4] to

changing inputs as compared to instability or enhancement control where the goal is the improvement of the combustion itself. Examples concerning model development for homogenous charge compression ignition (HCCI) applications, to be discussed further in Section 2.3, can be considered operating point control under this definition [14]–[16].

2.2.2 Instability control

Active instability control specifically deals with actively stabilizing a combustion system. This typically focuses on diminishing the magnitude of pressure oscillations within the system caused by the coupling between acoustic resonance modes and combustion [4], [11]. Controlling this coupling is a major concern and the subject of most advanced development due to the advent of low-nitrogen oxide (NO_x) lean pre-mixed combustors, which are particularly susceptible to instabilities [4], [10], [11], [17].

This control classification is directed towards affecting the relative phase between heat release and pressure oscillations within the combustor. Both [4] and [17] present a detailed review of techniques for active instability control with additional information for both sensor and control methodologies included in [11]. Additional examples can also be seen with a liquid-fueled low-NO_x combustor [18], natural gas burner [19], a 4 MW pre-mixed single nozzle research burner [20], [21], and two simulated gas turbine combustors [22].

2.2.3 Enhancement control

The final classification, active combustion enhancement, is concerned with actively altering the operation of the combustion process specifically by modifying the mixing of reactants to effect combustion efficiency, flame temperature, and pollutant formation as is described by Haile *et al.* [10]. The goal is not to improve stability of the combustion system necessarily (although it may be an ancillary

effect [18]), but to achieve improved and enhanced operation. Examples of active enhancement control are provided in work by Brouwer *et al.* [22], Haile *et al.* [10], Docquier and Candel [11], McManus *et al.* [17], Paschereit *et al.* [23], and St. John and Samuelsen [2] among many others.

Where active instability control is of interest in premixed combustors, instability is of lesser concern with diffusion flames and non-premixed combustors. Instead, combustion enhancement is the primary focus within the latter class of combustors because they are characterized by poor-mixing and long flames with large regions of elevated temperatures [10]. This is not always the case, however; a study by Cohen *et al.* [18] on a non-premixed combustor does have a dual focus of combustion stability and active combustion enhancement.

2.3 Combustion Modeling

System modeling plays an important role in combustion control. Combustion models can be used in a modified version of the closed-loop control seen in Figure 1.1 (b) and further described with different applications in [1], [2], [4], [10] and [24]. As well, combustion modeling is useful for off-line analysis and optimization.

System models may be categorized as white-box or black-box, based upon whether or not they rely on physical theory [25]. White-box models are built from equations describing the underlying physical phenomena, with model parameters that directly relate to physical quantities [25]. The governing physics include heat-transfer and thermodynamics, fluid dynamics and turbulence, chemistry, and even quantum-mechanics [26]. The underlying physics of combustion phenomena are either computationally intensive or intractable to modeling, which usually disallows the white-box approach for an online control application.

Black-box models abandon a physics-based interpretation of the system, and instead rely on abstract mathematical models built on testing data [8]. Techniques for black-box models generally utilize generic structures from system identification

theory, including online parameter estimation [25], [27] and are typically lower-order and simpler models of the equations compared to those which would be used in the white-box approach, but lacking any direct physical interpretation.

Between the white- and black-box models there is also a sub-category, a grey-box model, that makes use of lower-order parameters but remains loosely physics-based, where much of the higher-order dynamics of the combustion process is absent or replaced with approximations and functions fit to experimental data.

2.3.1 Physics-based models

A physics-based model using computational fluid dynamics (CFD) on a smaller-1.47 MW GenTex heating unit was completed by Daun *et al.* [28] and Hajitaheri [29] in 2011. This previous study modelled the droplet spray pattern, flow characteristics, and temperature profile of a 60-degree planar section of the inner coil of the heater. Satisfactory results were obtained by the authors in comparison with experimental values; the cold-spray droplet distribution and centerline temperature distribution showed good agreement with predicted values [28], [29]. Despite only modeling the inner coil of the heater, the computational time was much greater than the typical operating time for the heating unit [29], thus rendering such an advanced physics-based model impractical in an online control-related application.

A standalone example of a white-box model control is presented by Shaver *et al.*, who used their physics based model to operate a HCCI IC engine [14]–[16]. They utilize an Arrhenius-rate approach integrated with thermodynamic approximations and reactant concentrations to represent the lower order combustion physics [14], [16]. Utilizing a feedback linearization control, this method was able to successfully control the required engine outputs using propane, a relatively non-complex fuel compared to diesel. Widd *et al.* [15] also employ an Arrhenius-based approach for modeling that incorporated an in-cylinder heat

transfer model and wall-temperature prediction to link between each combustion cycle.

2.3.2 Non-physics-based models

Several approaches exist for modeling combustion processes without incorporating or having an understanding of the underlying physics. Model-predictive control is the standard method of advanced control for many chemical and petro-chemical processes [1], [30] and has also seen some limited use in combustion applications [1]. These models are generally lower-order linearized models of the controlled process and are based upon collected empirical data but have no direct true physical interpretation.

Another black-box model in recent use is the artificial neural network (ANN). Artificial neural networks are able to approximate any non-linear function by mapping the input-output relationship of the process and are trained using varied sets of collected data [31]. The complexity of the approximation is controlled by the structure of the neural network; higher-order functions and system behavior can be modelled and incorporated by increasing the complexity and interconnectivity of the ANN [31]. Blonbour *et al.* [24], Chu *et al.* [32], and Allen *et al.* [33] provide a varied collection of work where artificial neural network are utilized in combustion control applications.

2.4 Combustion Diagnostics

Both modeling and control require some indication of the state of the combustion process; for this heater these are provided by the sensors in a later figure, Figure 3.1. Determining the state, efficacy, or quality of combustion is an especially difficult task due to the high temperatures and/or pressures within and surrounding the combustion environment, as well as the timescale of the combustion events in some applications. Only a few flame parameters may be observed directly with

varying degrees of spatial and temporal resolution and accuracy [11] with any diagnostic method. Also, only a subset of these specific flame parameters are easily usable for control applications, and, even then, require filtration of the noisy signals recovered [2].

With the exception of ion-current sensors, a primarily upstream diagnostic technique, applicable diagnostics of the combustion process mainly infer the state of combustion from the data collected on the flue/exhaust gas downstream of combustion [11]. These downstream techniques are divided into the three primary categories as described below.

2.4.1 Solid-state gas sensors

Electrochemical solid-state sensors are extensively used in automotive IC engines to detect species mole fractions in the exhaust gases. The robustness and relatively low-cost of these sensors, has enabled widespread use at the sacrifice of some absolute measurement accuracy. Current sensor technologies are able to detect variable amounts of oxygen, nitrogen oxides, unburned hydrocarbons, or carbon monoxide [11], although they are mainly used to measure oxygen content in the combustion exhaust gases [11], [34].

Typical electrochemical solid-state sensors rely on some form of ceramic matrix, either zirconium, titanium, or tin oxides, doped with other oxides to effect species selectivity and performance of the diagnostic sensor. Past solid-state technologies utilized these metal oxides or pairs of catalyzed resistance temperature detectors but have since been replaced by Nernstian-driven zirconium cells due to their selectivity and robustness at elevated temperatures [11]. The multiple configurations of a zirconium-based solid-state sensor as well as the operation of such a sensor is explored in-depth by Benammar [34] and Ivers-Tiffée *et al.* [35].

As mentioned above, in addition to measuring oxygen, zirconium-based sensors can also be used to measure carbon monoxide and nitrogen oxide mole

fractions within the exhaust/flue gas [11]. This technology, however, is relatively immature, slower to respond, and more complex, as the measurement results have a cross-sensitivity to oxygen.

Oxygen sensors are ubiquitous in automotive applications, and are occasionally used in industrial combustion [36]. de Lima *et al.* [36] utilized both heated and unheated automotive oxygen sensors in the flue gas of a model 50 kW burner. The authors reported relatively good response and accuracy within the range required by industrial applications.

2.4.2 Optical sensors

Optical techniques feature good spatial and temporal resolution and are generally non-intrusive; all of which are excellent features for combustion diagnostics. Optical diagnostic techniques are based upon monitoring of the emission, absorption, scattered light, or fluorescence of both the flame or flue gas, depending upon the parameters of interest [11]. Docquier and Candel [11] provide an excellent overview regarding the placement, diagnostic principles, and detectable quantity of interest for optical diagnostic techniques.

Optical techniques requires some form of optical access into the combustion process, either a window or sight-glass, and this may be difficult to incorporate into most combustion devices [11]. The optical sensors must be capable of withstanding the high temperatures and pressures typical of combustion, and, consequently, continual cooling of the window is usually required. The robustness of these solutions is also questionable due to fouling by soot and particulate matter. However, Demayo *et al.* [19] was able to compensate, within the control methodology, for highly fouled windows with their in-situ measuring of ultraviolet chemiluminescent intensity experiments.

2.4.3 Extractive techniques

Extractive diagnostic techniques and devices, while not directly sensors, bear mentioning because they are an important category of continuous emissions monitoring systems. Typically, they are composed of electrochemical and optical sensors for individual flue gas species measurement where the flue gas is extracted from the in-situ process and analyzed simultaneously.

Extractive techniques are highly precise and accurate, and consequently they are the method of choice for assessing regulatory compliance. They are not suited for most industrial control applications, however, as they are often large, expensive, and require a water trap, rendering them unsuitable for harsh-environments, and often have slow response times [11].

2.4.4 Ion-current sensors

Ion current sensors are a diagnostic technique developed to fill the niche where optical access or other measurement techniques are impractical or detection of exceptionally quick transient events are required [11]. Ion-current probes detect ions produced through chemi-ionization in flames; using a minimum of two electrodes, an electrical potential may be induced across at least part of the flame and the responding current may be measured [37]. Further work into the precise mechanism of operation and relevant chemical radicals are provided in [11] and [37]. This technique has seen use in laboratory-scaled burners, IC engines, and simulated gas turbine combustors [11], [37] and while the signals are difficult to interpret, correlations exist for equivalence ratio, pressure, and flame presence in a variety of applications.

2.5 Actuation Methods

The actuator is critically important to the overall control methodology and the choice of actuator largely depends on the physical phenomenon or characteristic of combustion to be affected [10]. Actuators are similar to sensing/diagnostic technologies in that they are the physical link between the controller and the combustor but differ in that they affect a change instead of measuring an outcome of the combustion process. Their function within an overall control methodology can be seen in Figure 1.1. Within this study, actuation methods are subdivided into the three broad categories relevant to this study and are differentiated by what components they modify within the combustion process.

2.5.1 Atomizing air modulation

The first category, modulation of the atomizing air, involves directly changing the pressure or mass flow rate of the air going into the nozzle. Both Brouwer *et al.* [22] and Allen *et al.* [33] utilize a direct modulating actuator in a liquid-fueled model gas turbine combustor and a utility boiler respectively. Both sets of authors use a servovalve actuator to alter the air flow rate to air-assisted fuel nozzles; there are many similarities between these combustors and the combustion assembly within the GenTex 70M process heater. A similar example by St. John and Samuelsen [2] used magnetic valves to control the quantity of excess air and swirl intensity for an industrial natural gas burner. Delabroy *et al.* [3] actuated the atomizing air through the use of a rotary valve on the supply atomizing air line to pulse the atomizing air pressure at a frequency proportional to the rotary speed of the valve.

2.5.2 Fuel modulation

Differing from atomizing air modulating actuators, the fuel mass flow rate or fuel line pressures are modified. Büche *et al.* [38], [39] use a series of eight analog valves to control the fuel mass flow in an open-atmosphere model turbine combustor

can/chamber. Each of the valves controls a single adjacent pair of ports in the fuel nozzle (16 total ports) and to reduce the number of free variables for optimization in their experiment, the total fuel flow rate was fixed.

Using the earlier control classifications, the control objectives from Büche *et al.* [38], [39] would be considered combustion enhancement control. However, fuel modulation is extensively used in instability control as well. This can be attributed to the sizable energy density of hydrocarbon fuels and that only a small portion of this energy is necessary to drive oscillations in susceptible combustion systems (*i.e.,* weakly damped combustion chamber designs) [4]. One of the most studied instability control actuation methodologies is to pulse, with changeable frequencies, the fuel flow rate to counter the oscillations, which places the energy and pressure oscillation out of phase [6], [40]. Haile *et al.* [6], Hermann *et al.* [41], and Hantschk *et al.* [7] provide examples of this with a bespoke 'electro-valve' and 'piezo-actuator', and direct-drive servo-valve actuators respectively.

2.5.3 Other modulation

As mentioned at the beginning of this section, actuator selection depends largely on the specific target outcome from the combustion system and the specific configuration of the combustor. While a wide range of potential actuators fall into this category, only flue-gas recirculation as a modulation/actuation method will be discussed in this research.

Flue-gas recirculation (FGR, also called exhaust-gas recirculation or EGR in automotive/other applications) has a niche role in regards to actuation methods and bears mentioning here. It does have potential for future developments beyond this study and it was considered as a possible option at the beginning of the project. Ignoring the passive or inactive form of FGR, this actuation method is generally controlled by altering the position of a valve to alter the mass of already burned flue gas to be recycled into the combustor [42]–[44]. The incoming fresh air is diluted by the flue gases, effectively lowering the flame temperature and preheating

the incoming air. The resulting decrease in NOx emissions can be significant with an accompanying possible increase in thermal efficiency.

2.6 Optimization

A *true* optimization process requires the definition of a quantitative value or objective function that quantifies the performance of a state, and then seeks to find an extremum (maximum or minimum) of that value. A multitude of methods is available and can be performed in-situ with the process, for example as in [2], or ex-situ as with [32]. Relating to the employment of a control method, an optimization process may follow a series of steps as in Chu *et al.* [32] including: collection/acquisition of data, model creation, and then optimization which may or may not take place in a closed-loop as seen in Figure 1.1.

As discussed in the Introduction, this study will presently be concerned with fuel efficiency as the sole objective function. Absolute thermal heat output, or equivalently the thermal rise of the process fluid across the heater, regardless of fuel input/efficiency, is important to the customer or operator of these process heaters will be given consideration as a secondary objective at a later time. Pollutants, while important within the global scope and within this project manifest, are reserved for future work. Examples of optimization within the realm of combustion control are included below.

Past research, such as work by St. John and Samuelsen [2] optimized both nitrogen monoxide (NO) levels and thermal efficiency. The authors minimized the objective function using a direction-set search algorithm, and separately a genetic algorithm, with similar conclusions. The control objective used by Delabroy *et al.* [3] was to minimize the pollutant levels, nitrogen oxides (NOx) and carbon monoxide (CO), in the exhaust gas of both a 20 kW single nozzle burner and an 800 kW combustion system. Büche *et al.* [38], [39] and Paschereit *et al.* [23] use a multi-objective evolutionary algorithm to optimize both NO_x levels and pulsation simultaneously. The two objectives within these studies are conflicting and

corresponding manifest as a Pareto front, a common occurrence in multi-objective optimization studies. Chu *et al.* [32] utilized an optimization method that married several different search and minimization concepts together to optimize thermal efficiency. These methods included, random searching, fuzzy c-means clustering, and the minimization of information free energy. Similar to the other examples, Padmanabhan *et al.* [45] minimizes, using a downhill simplex algorithm, the pressure fluctuations of a laboratory scale combustor, but accordingly they also seek to maximize the volumetric heat release rate.

2.7 Closure

This chapter has covered a review of relevant past research relating to the subject of this study. A discussion of a few salient subject areas has also been completed in addition to explaining the categorization of these areas.

Chapter 3

Experimental Apparatus

3.1 Introduction

This chapter discusses the intertwined experimental setup, components, and controls of both the centralized-digital-control (CDC) system and the optimal control methodology. Both the CDC system and the optimal control strategy were developed simultaneously since these two systems are strongly interrelated. This development was guided based on the literature review presented in the previous chapter and internal GenTex industry experience.

The 'components' added to the existing process heater, to accomplish the two objectives outlined in Section 1.4, are divided into three functional groups:

(i) computing, data storage, and human-interface hardware;

(ii) sensor technologies used to measure the important physical quantities input/output to/from the process heater; and

(iii) actuators which modify the operation of the process heater by effecting a change in the input operating state.

This chapter is divided along these three broad categories. A complete diagram of all sensors/meters and actuators discussed and their placement on the process heater can be observed in Figure 3.1 on the next page.

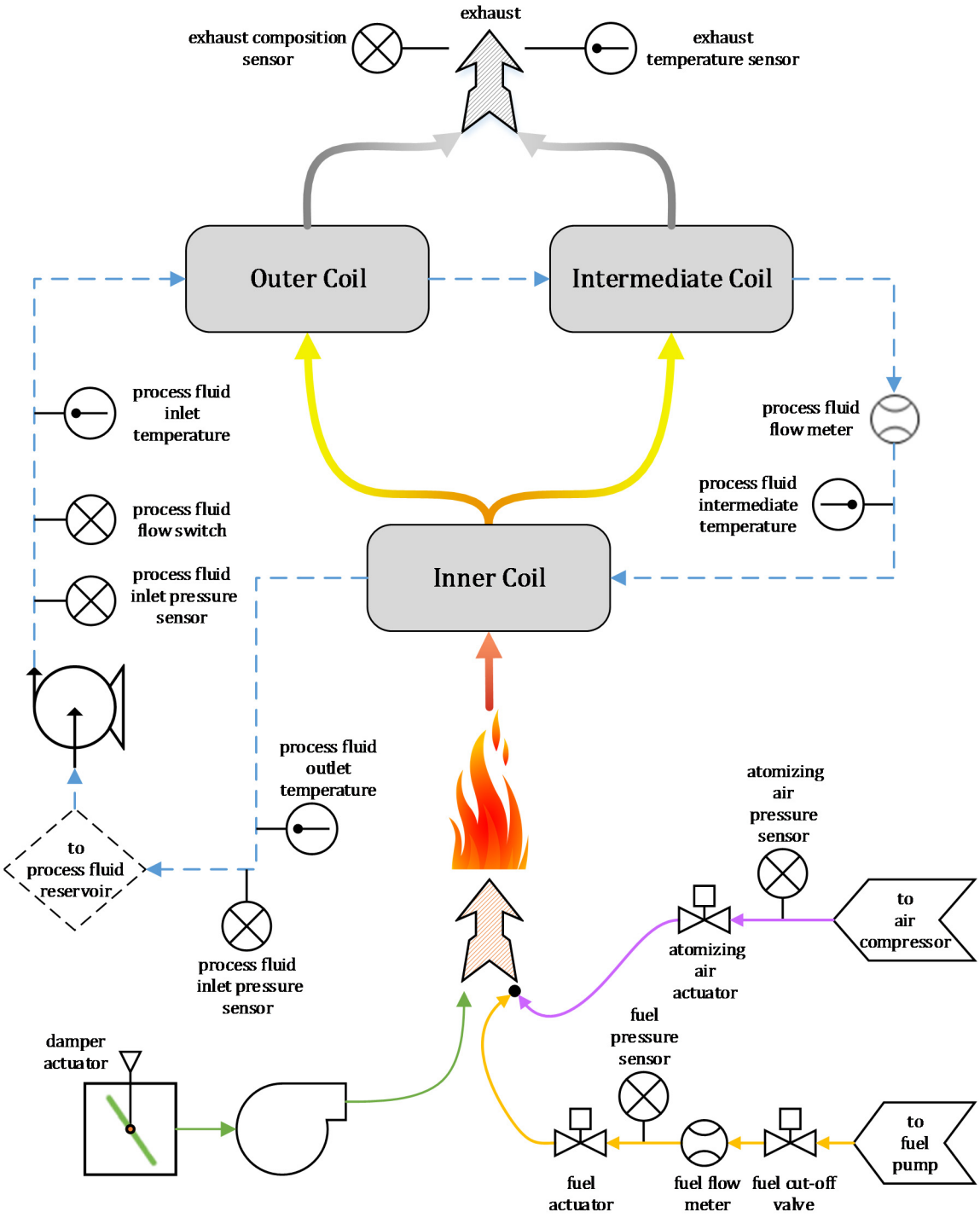

FIGURE 3.1: Sensors and actuator on the experimental apparatus.

All sensors, actuator, and hardware technologies realized within this experimental apparatus must conform to three primary requirements defined by typical operating environments of the oilfield:

1) an ambient temperature range of 233.15 K to 313.15 K (-40 °C to +40 °C);
2) utilize 12 V DC power as it is a mobile platform. 24 V DC and 120 V AC power are available through the use of transformers and inverters respectively, but are greatly discouraged due to the added complexity and cost; and
3) a minimum rating of IP65[1] with additional physical covering/shielding for water ingress during wash-down or IP67 without additional shielding.

3.2 Hardware

The computing and human interface hardware used on the 70M TEXHEATER heating unit and CDC system was selected prior to the commencement of the study and is considered as a constraint; all further work must make use of this or directly interchangeable hardware. However, the use of interfacing and complimentary hardware is possible. The reasoning for the constrained hardware and computing architecture is:

- the CDC system hardware is currently standardized across a portion of GenTex production heating and pumping units with an eventual rollout for the full range of GenTex products;

[1] The Degrees of Protection Provided by Enclosures (IP Code) published as ANSI/IEC 60529, classifies the degrees of ingress protection for electronic enclosures to solid foreign objects (first designating number) and water (second designating number).

- the research and developments, or a portion thereof, that began within this study are to be utilized within future internal GenTex research projects; and
- all safety controls, a necessary component of the process heaters, are implemented electronically within this architecture and cannot be overridden or displaced.

The majority of this architecture is sourced from *ifm electronic GmbH,* a firm that provides automation hardware and technologies with a unique product line dedicated to mobile control applications.

Data sheets outlining all of the hardware used within this study are included in Appendix A. The hardware is classified according to the function of the hardware: computing, human interface, and data acquisition/other uses.

3.2.1 Computing hardware

The backbone of the computing hardware is a programmable logic controller (PLC). The PLC utilized is an *ifm electronic* CR0232 mobile controller with a 32-bit processor at 150 MHz with 32 digital and analog inputs, 48 digital outputs, and 4 CAN (Controller Area Network) interfaces. The PLC is programmed using the CoDeSys 2.3 development environment, which conforms to the IEC 61131-3 international programming standard, in the Structured Text (ST) and Function Block diagram (FB) languages.

The majority of operating functions and all safety controls were implemented on the CR0232 controller, shown in Figure 3.2, which is a 'hard' real-time system. This means that, inherent within the PLC in the underlying Linux operating system, there is a watchdog function that will hard-restart the controller if a single process unit exceeds the 100 ms execution time, which prevents stalling or 'freezing' of the PLC. Otherwise, the possibility of a stalled or slowed PLC

presents a serious safety hazard. All sensor input signals, both analog and digital, and actuator output signals were handled by the controller.

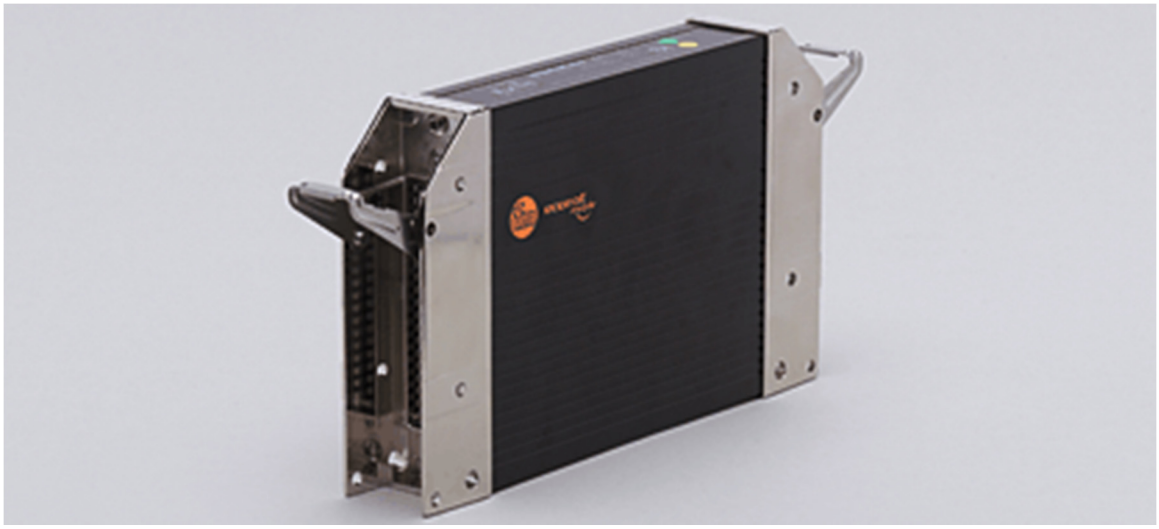

FIGURE 3.2: ifm electronic CR0232 programmable logic controller (Source: *ifm electronic GmbH*).

3.2.2 Human interface

The human machine interface (HMI) provides the visual link between the operator and the PLC. Prior implementations of a touch-screen HMI on non-*ifm* hardware had been attempted by GenTex, but resulted in unsatisfactory feedback from operators. As a result, an *ifm electronic* CR1081 process and dialogue module with a 400 MHz 32-bit processor and 1 Gbyte internal storage was used. The HMI has a 7 inch colour display, nine programmable function keys, an additional four-way rocker switch, and pushbutton toggle. The CR1081 interface has no inherent input-output capability with the exception of a USB interface and four CAN interfaces, one of which is used to facilitate 2-way communication with the CR0232 controller. A second CAN interface was used to communicate with the data acquisition device. A picture of the HMI is provided in Figure 3.3.

FIGURE 3.3: ifm electronic CR1081 human machine interface (Source: *ifm electronic GmbH*).

While all safety functionality, sensor, and actuator signal input/output (I/O) was handled by the CR0232, all user interface control was performed using the CR1081. As stated in Section 3.1, pursuant to the goals of the CDC, all analog gauges were replaced and made viewable on the CR1081 with digital readouts of temperatures, flow rates, pressures, and other measurement quantities. As well, all previous manual control functions were moved to the HMI and enabled by the function keys, toggle, and pushbutton. A user interface (UI) was designed by this author; sensor readouts and certain operating set points selectable by the operator are displayed in the HMI shown in Figure 3.4.

3.2.3 Additional hardware

Two other pieces of additional hardware are worth mentioning in this section: an electronic and wiring housing, and the data acquisition (DAQ) or data logger system.

To ensure ingress protection from water, dirt, and oils, all electrical connections were made using M12 industry standard connectors to a housing used to distribute all of the connections. Inside the housing are one- and two-layer DIN

rail terminal blocks and fuse holders for individual actuator/hardware circuits. The housing also contains the PLC and all associated wiring, connectors, and signal converters.

FIGURE 3.4: As-mounted configuration of the CR1081 screen with sample UI.

Similar to the PLC and HMI, the data logger, a CR3101 or CANmem unit, was supplied by *ifm electronics*. Communicating with the PLC directly through another one of the CAN interfaces, the data was recorded directly to a 2 GB Secure Digital (SD) memory card with a programmable recording rate. While communicating between CANopen devices, an industrial automation communication protocol used by most *ifm electronic* devices, is theoretically simple, setting up the communication between the PLC and the CANmem unit required a large amount of time to resolve. In contrast, enabling CAN communication between the PLC and HMI was quick and relatively simple. Additional difficulties were encountered due to the undocumented and unknown (even by *ifm electronic* support) necessity of the CR3101 requiring a pre-2006 SD

card with a storage capacity of less than 4 GB instead of the newer and commonly available SDHC or SDXC memory cards.

3.3 Physical Sensors

Physical sensors convert physical quantities into signals useable by the PLC and are generally categorized by the physical quantities they measure: temperature, pressure, and fluid flow rate among others. Due to its robustness to outside signal noise and interference, ease of setup, and troubleshooting in comparison to non-current loop methods, the output of most physical sensors use a 4-20 mA output. These became a desired feature for all sensors with any exceptions to this noted in the proceeding relevant sections. Table 3.1 displays the expected ranges for most of the relevant sensor quantities, based on the expected operating range of the 70M TEXHEATER. All sensors and their locations on the heating unit are summarized in Figure 3.1.

TABLE 3.1: Expected physical quantity ranges for sensor selection.

Physical Quantity	Lower Range	Upper Range	Units
Process Fluid Pressure	0.0	1250.0	kPa
Process Fluid Temperature	258.15	398.15	K
Process Fluid Flow Rate	0.0	9.2	L s^{-1}
Fuel Flow Rate	0.000	0.095	L s^{-1}
Fuel Pressure	0.0	620.0	kPa
Atomizing Air Pressure	0.0	520.0	kPa
Exhaust Gas Temperature	258.15	1023.15	K

3.3.1 Temperature

Process fluid temperature is measured at three points on the heater: (a) at the inlet to the outer coil, (b) between the intermediate and inner coils and, (c) at the outlet of the inner coil/heater. All three of these sensors are PT1000 resistance

temperature detectors (RTD) with an *ifm electronic* model number TA3333. It has a measuring range of 255.35 K to 422.05 K (-17.8 °C to +148.9 °C).

One item to note, a deviation from the above ranges, is the manufacture's recommended minimum operating temperature is -25 °C for the TA3333. This is obviously higher than the required minimum temperature specification stated earlier and is a typical minimum operating temperature specification for the majority of *ifm* products. After telephone conversations with an *ifm electronic* representative, the product was assured to operate reliably beyond this specification; a fact that has been confirmed through several seasons of harsh Canadian winters on GenTex equipment operated by customers. These temperature measurement requirements are necessary as a water-glycol mixture typically replaces pure water during below 0 °C weather.

Two additional temperature sensors are necessary on the process heating unit. The first is a probe on the process fluid outlet that extends inside of the inner coil, which is necessary for safety purposes (*e.g.,* the presence of an ice plug within the heater). This sensor is referred to as a Kimray sensor and is named after the pneumatic-over-mechanical-over-temperature shutdown system it partially replaced. The second is a sensor on the exhaust stack to measure the temperature of the exhaust gases exiting the heater. These two probes are PT100 RTD sensors manufactured by Omega Engineering (model number PR-26B). An additional sending unit was required for these sensors to convert to a 4-20 mA signal with a user settable programmable range appropriate to the location of the probe (Omega Engineering, model TX-M12-RTD-C-1.)

The above two temperature sensors were the second attempt at measuring temperature of the exhaust gas and process fluid within the heater. The first consisted of two Type K thermocouples in 9.5 mm stainless steel thermowells/sheaths. The temperature signal was resolved into a 4-20 mA signal with a PR Electronics 5334A transmitter. The sensors and transmitters were replaced after multiple failures which troubleshooting could not resolve.

3.3.2 Pressure

Process fluid pressure was measured at the inlet and outlet to the heater and are used to determine correct operation of the process heater with additional safety concerns described in Section 3.5. PT3553 pressure transducers manufactured by *ifm electronic* were used with a measuring range of 0 kPa to 2500 kPa (0.0 to 362.6 psi) gauge pressure. Similar to the TA3333 temperature sensors mentioned previously, extensive testing has proven that the PT3553 pressure transducers are able to operate beyond the stated ambient temperature range.

The same pressure sensors were also utilized on the atomizer input fluids (diesel fuel and atomizing air).

3.3.3 Process fluid flow rate

The process fluid flow rate, together with the temperature measurements and fuel flow rate are needed to measure the thermal efficiency of the heater. A Simark 38mm turbine flow meter mounted on the external piping between the intermediate and inner coils was initially considered and which has a measuring range of 0.95 to 11.35 litres per second. A magnetic pickup on the flow meter body was used to receive and transmit a frequency signal to the PLC. Due to the small tolerances between the turbine and the housing of the flow meter, the meter was liable to become jammed with large particulates and choke the process fluid flow through the heater. This represented a significant safety hazard, and consequently another solution was necessary for development.

A less invasive flow meter was found in the GPI DP490 insertion-type paddlewheel flow meter with all high temperature options and a NPN open collector pick-up. This sensor proved more resilient to particulate matter, but outputs, at least in this configurations a noisier output signal. The combination of digital and moving average filters implemented on the PLC reduced the noise to acceptable levels.

3.3.4 Fuel flow rate

Within this study, and of all of the sensors, the measurement of diesel flow rate proved to be the most troublesome, due to the changing viscosity of the diesel fuel within the typical operating temperature range of the process heater. The fuel viscosity (and other properties to a lesser degree) changes due to seasonal, geographic, and supplier variance of diesel fuel blends to ensure that the diesel fuel does not wax or crystallize at low temperatures. Commercial data on diesel seasonal blends [46] as well as research by Yuan *et al.* [47] illustrate the extremely wide range of diesel kinematic viscosities over the desired temperature range of 233.15 K to 313.15 K (-40.0 °C to +40.0 °C). Using the data in the above works and extrapolating for the lower limit, the kinematic viscosity is estimated to be between 2.5 and 25 cSt. Most commercially-available flow rate meters cannot operate at these kinematic viscosities; the two typical sensor choices, turbine and gear-type flow meters, either have intolerably high errors bounds or excessive pressure losses at the lower and higher viscosity limits, respectively. These typical high error bounds may be reduced through the use of dimensionless numbers in the below analysis.

Traditionally turbine flow meters correlate the measurable signal of frequency, f, in units of Hz and the volumetric flow rate, Q, in units of L s^{-1} through the use of a K-factor, K, with units of pulses or cycles per litre,

$$K = \frac{f}{Q} \tag{1}$$

As mentioned above, the performance of the turbine flow meter is sensitive to the kinematic viscosity of the measured fluid. This is seen in Figure 3.5 [48], which displays significant deviations from linearized behavior at low flow ranges and an increasingly narrow linear flow range with increasing viscosities.

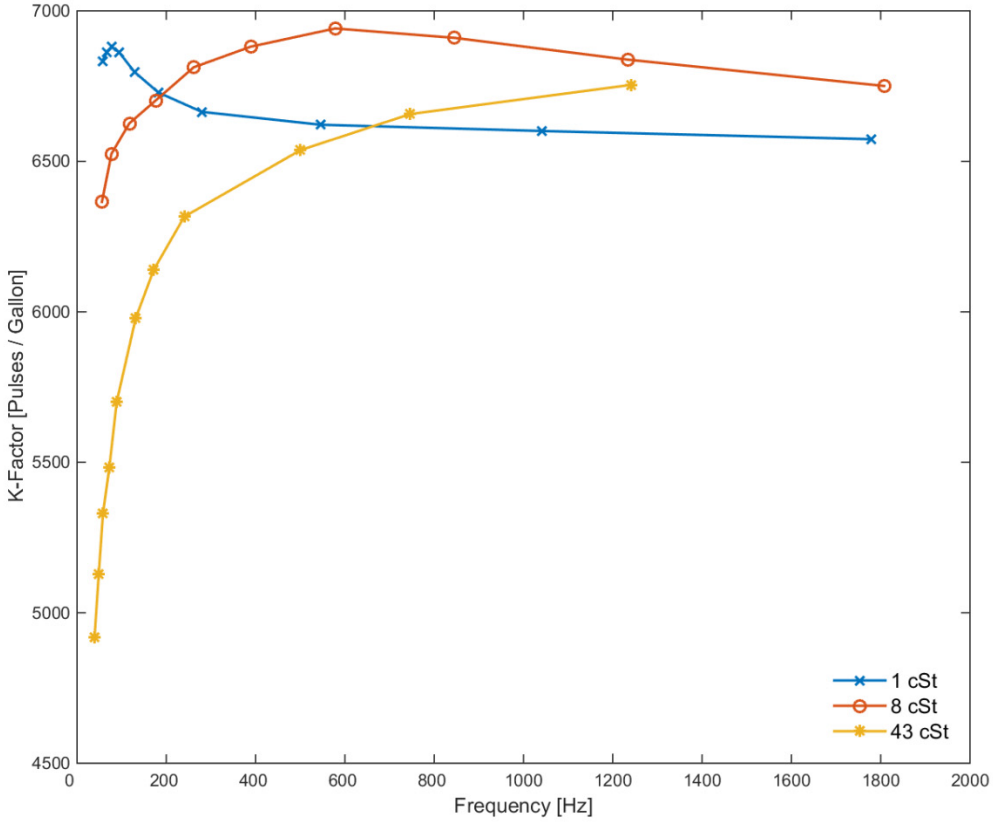

FIGURE 3.5: Plot of frequency versus K-factor at different fluid viscosities.

A better method of representing the data, with practical uses in flow measurement, is through the use of a universal viscosity curve (UVC) shown in Figure 3.6 for the same data set. The UVC does not use frequency as the independent variable but instead uses a modified Reynolds number, in the form of a ratio of frequency and kinematic viscosity.

The UVC accounts for changes in viscosity, usually performed through testing different fluids with different viscosities at a constant temperature. This is necessitated through the physical fact that, assuming a null change of viscosity with pressure and that it behaves as a Newtonian fluid, viscosity is a unique function of temperature. Accordingly the UVC does not account for temperature

changes in environment/fluid medium and previous studies have shown inaccuracies of 0.03% per 12.2 K from as calibrated temperatures [48], [49].

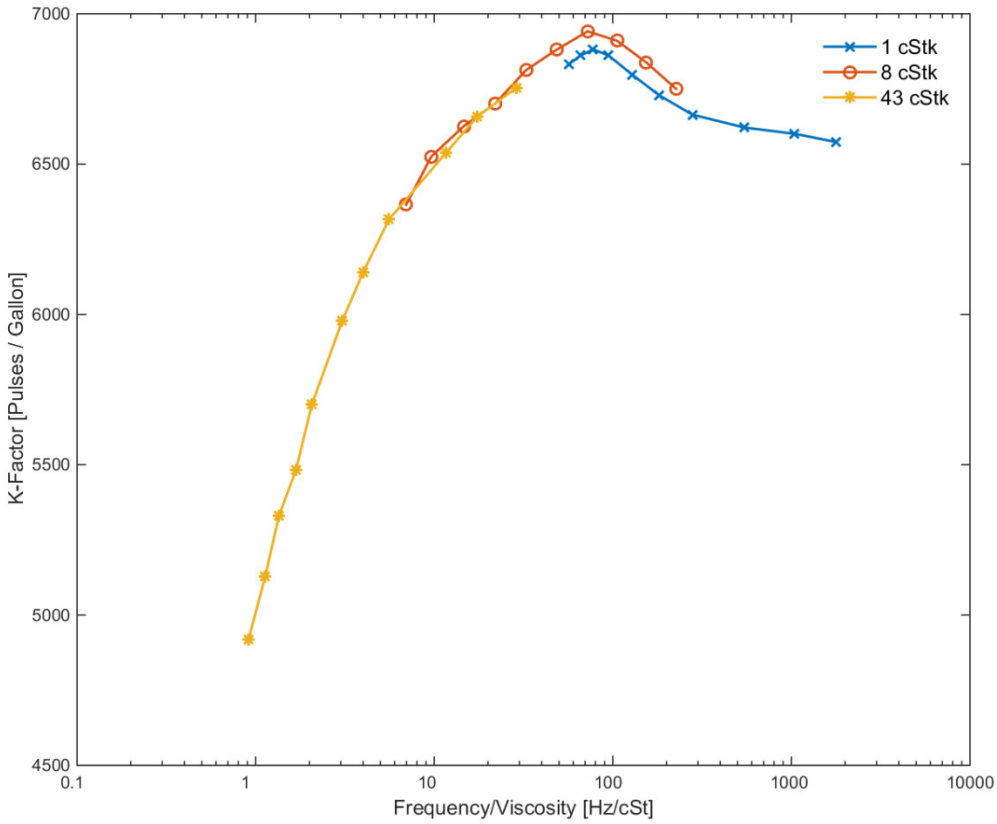

FIGURE 3.6: Universal viscosity curve (UVC) for flow measurement.

These errors are significant for the temperature and viscosity range of this study when compared to the typical stated values of a turbine flow meter of ±0.1% and ±0.02% for absolute accuracy and repeatability, respectively. The use of two dimensionless numbers, the Strouhal Number (St) as a function of the Roshko Number (Ro), accounts for this effect in differing temperatures. The forms of these dimensionless numbers used for this purpose can are defined below where α is the coefficient of thermal expansion of the material comprising the body of the turbine flow meter and ΔT is the difference in degrees from the calibrated fluid temperature [48]–[50]. Sample calibration curves formed using the two dimensionless parameters

is shown in Figure 3.7, with the same data as before but with a reference temperature of 294.2 K.

$$St = \frac{f}{Q}\left(1+3\alpha\Delta T\right) = K\left(1+3\alpha\Delta T\right) \tag{2}$$

$$Ro = \frac{f}{\nu}\left[1+2\alpha\Delta T\right] \tag{3}$$

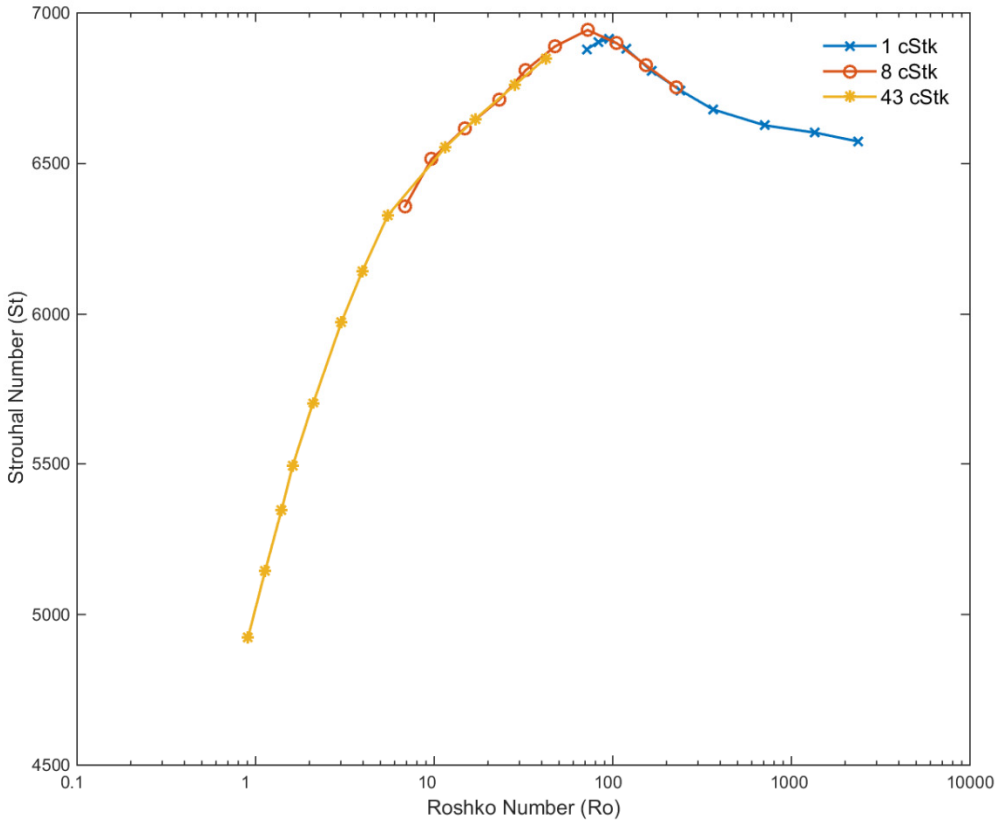

FIGURE 3.7: Roshko versus Strouhal Number calibration curve.

A Cox Exact Turbine Flow Meter, manufactured by Badger Meter, was considered for this application. This meter makes use of hydraulically coupled dual helical axial turbines to extend the usable range of the flowmeter as necessitated by the desired flow range and dynamic viscosity range of the diesel fuel. It is widely used

to measure the fuel flow rate to turbine jet engines [51], an application that requires slightly more stringent hardware standards than the present application. The expense of this system and the additional component count and cost through the necessary use of a secondary flow computer (making use of the Ro/St analysis above) and flow straighteners (both upstream and downstream of the turbine) excluded this method from practical use in this study.

The sensor ultimately chosen to measure the diesel fuel flow rate is a Model 214 flow meter manufactured by Max Machinery. This flow meter meets all accuracy requirements regardless of the changeable dynamic viscosities and fluid temperature. The model 214 is a positive displacement flow meter with four axisymmetric pistons and connecting rods attached to a common crankshaft as is seen in Figure 3.8 below. As it is a positive displacement flow meter, the fluid volume measured is exactly the swept/displaced volume of the piston in the meter and the output signal is proportional to the rotational frequency of the crankshaft. The model used in this work has an analog transmitter, converting the rotational frequency to a 4-20 mA output. Additionally for further improvements in accuracy, it is possible to incorporate the above Roshko versus Strouhal analysis within future work.

3.3.5 Exhaust composition

As discussed in Section 2.4.1 the use of Nernstian solid-state oxygen cells is a proven technology to measure oxygen content in exhaust gas streams. An oxygen sensor operates as a solid electrolyte allowing the transporting oxygen ions across the cell; however this process only becomes effective above about 590 K [11]. The transport of the oxygen ions produces a measureable electromotive voltage while conversely providing a voltage to the cell causing the zirconium electrolyte to operate as an electrochemical oxygen pump [11].

FIGURE 3.8: Max Machinery 214 piston flow meter. (Source: *Max Machinery, Inc.*).

More complex oxygen sensors exist by combining two of these cells to maintain an oxygen balance in a reference chamber, allowing the sensor to measure exhaust gases with both excess and deficient oxygen contents, rich and lean combustion states respectively.

Exhaust composition on the process heater was measured using a wide-band automotive oxygen sensor, a Bosch LSU 4.9 probe. The concept of using an automotive oxygen sensor as a reasonable cost, rugged oxygen sensor had been previously explored by de Lima *et al.* [36]. To control the electrical heater within the sensor and interpret the signal of the Nernstian oxygen cells, a LCU-One lambda controller manufactured by AiM Sports, typically used in automotive and

kart racing, was used. The converted units of measurement from this sensor within this study are percent excess-oxygen (%-EA).

3.4 Actuation Methods

Similar to the previous section on physical sensing, actuation methods are categorized according to what is being actuated, which, in this study are: the process fluid flow rate, atomization air pressure, diesel fuel pressure, and quantity of combustion air.

While additional control/actuation may improve combustor performance (*e.g.,* slow pulsation of the fuel pressure for alternating rich/lean combustion zones), using more actuators leads to increasing complexity in the control algorithm. For example, altering only the frequency and magnitude/position of an actuator, results in a minimum number of independent variable of $2n$–1 with n actuators [10]. Consequently, the selection of actuated parameters must be chosen with care in order to obtain a reasonable trade-off between performance and complexity. All actuators and their locations on the heating unit were summarized in Figure 3.1.

3.4.1 Process fluid flow rate

While the process fluid flow rate remains constant in typical operation, this parameter is controlled by the CDC system through the CR1081 and CR0232 hardware modules. A pulse width modulated (PWM) signal from a high current H-bridge output on the CR0232 PLC was input to the Sauer Danfoss hydraulic motor that powers the centrifugal pump.

3.4.2 Atomization air pressure

Sourcing an appropriate sensor for controlling atomizing air pressure, and implementing it on the heating unit, was a particularly challenging undertaking. An analog input signal was required for closed-loop control of the atomizing air pressure. However, the majority of analog pressure valves either did not conform to the minimum ingress protection rating, or would not operate at the lowest temperatures expected for oilfield operation. Ultimately, however, a Norgren VP10-series electronic pressure regulator was identified that satisfied these requirements.

While the CR0232 PLC does not have any direct analogue outputs with the exception a PWM signal, which is still technically a digital output, it can be programmed to output a desired current or voltage output. Attempts to have the PLC output a 4-20 mA signal failed as the valve functioned as an on-off valve when the desired current control signal was changed within the PLC. It was ultimately determined that the current output of the PLC, owing to transistor leakage within the PLC, does not allow the required fine control of a 4-20 mA signal. To overcome this challenge an Axiomatic Technologies AX130201 DIN rail mounted PWM to 4-20 mA signal converter was placed within the housing containing the wiring and fuses.

The atomizing air pressure was controlled using a closed-loop PID (proportional-integral-derivative) controller implemented within the PLC with input from the atomizing air pressure sensor. This allowed for selection of the atomizing air pressure directly, as opposed to controlling the output signal, either directly PWM or indirectly the current signal. Further benefits were observed in tolerance to error or 'drifting' of the output as the air pressure source fluctuated when the air storage tank was being charged by the on-board air compressor or being discharged.

3.4.3 Fuel pressure

Actuating the fuel pressure was far less troublesome as an appropriate actuator was readily available to enable closed-loop control of the fuel pressure. A Sun Hydraulics Corporation FPCC-DBN normally closed electro-proportional flow control cartridge valve with a 212 coil was used. The cartridge valve was mounted in a 2-port stainless steel valve block and controlled with a PWM signal from the PLC with the manufacturer recommended control frequency and dither values. Similar to the previous section, a PID control loop was used in combination with the fuel pressure sensor.

3.4.4 Combustion air

The control of the amount of combustion air introduced into the heater was the most difficult actuator to implement in this study. All combustion air actuators altered the angular position of the butterfly damper on the inlet to the blower fan unit, from fully closed to fully open, a 90 degree rotation. Two actuators were implemented and were found to either work incorrectly or not meet the accuracy requirements before a solution was found and implemented with success.

The first actuator trialed was the Electrak Pro-Series DC-powered linear actuator manufactured by Thomson Industries with a 150 mm stroke length and an integral linear potentiometer for absolute position sensing. As shown in Figure 3.9, this actuator (blue) was mounted to the experimental apparatus using a clevis (green) mounted to the skid and actuator base and another clevis (yellow) on the damper shaft connecting to the rod-end on the actuator.

The actuator is controlled by a dual pole input, controlling extension or retraction of the actuator rod and implemented using three relays controlled by the PLC. A form of bang-bang control [52] with a deadband was implemented by monitoring the position of the actuator through the potentiometer and disabling extension/retraction of the actuator rod when the deadband was reached. Due to

the significant inertia of the DC motor and actuator rod, the control would 'coast' outside of the deadband and then reverse direction. This process would complete several times before the actuator would stop moving and remain within the deadband. Increasing the size of the deadband did not completely solve the issue as the actuator possessed a large amount of hysteresis and would not 'coast' the same amount each time motion was triggered. The obvious solution of using PWM control to control the time averaged voltage and thus rotational speed of the DC motor was specifically not allowed by the manufacturer with warning that damage to internal electronics would occur. After much experimentation, the DC stopped responding to input commands from the PLC and would 'stick' at a given position. A new solution was necessary with a greater accuracy of operation and robustness.

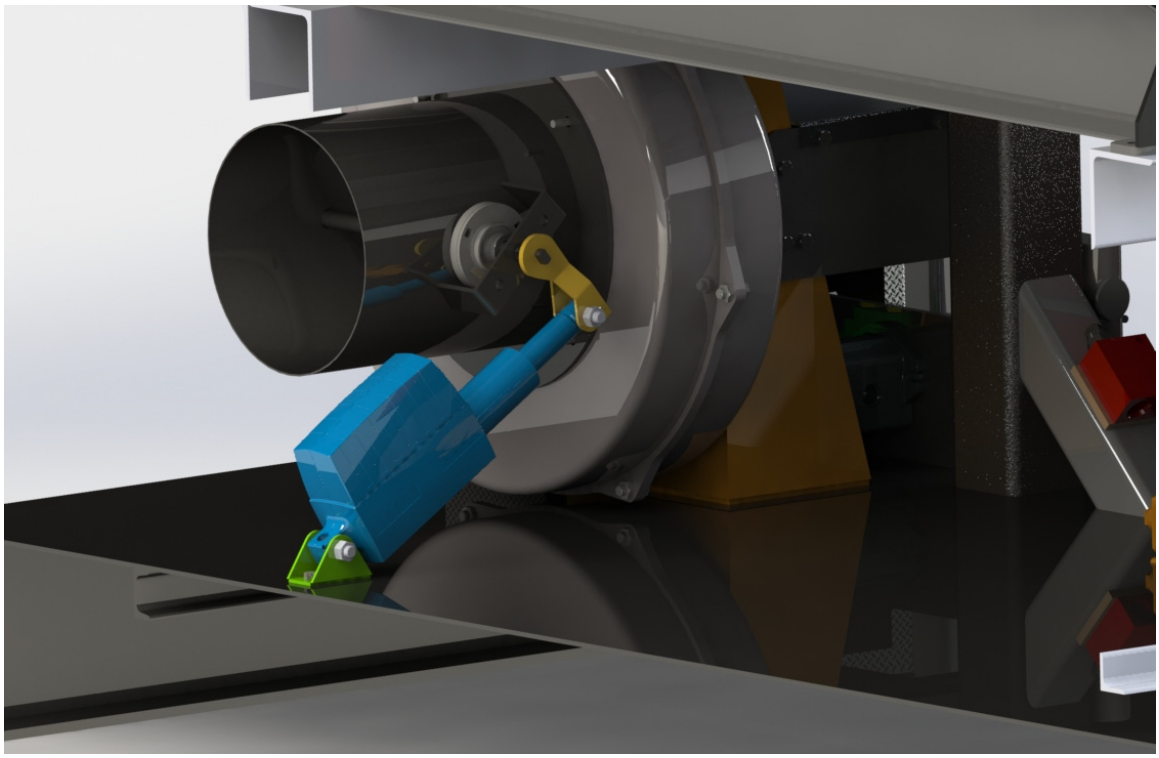

FIGURE 3.9: Rendering of the first combustion air actuator attempt.

The second actuator evaluated was an IP65 rated stepper motor manufactured by Applied Motion Products, model number HW23-754, with an additional 5:1 planetary gearset to increase the torque output. The stepper driver

used was a Lin Engineering R1025 stepper motor driver. The motor and gearset were coupled to the damper shaft using a Lovejoy Jaw coupler and the motor was mounted to a vertical steel plate bolted to the heater skid. As this actuator does not have an absolute position sensor, it is necessary to determine a reference position first. An *ifm electronic* IFC246 inductive proximity sensor referenced a bolt perpendicular to the axis of rotation on the Lovejoy coupler to determine the fully-closed position each time the system was powered on. The rising trigger of an output from the PLC to the R1025 would cause the motor to step a single step or microstep with a second digital input to the R1025 controlling clockwise or counterclockwise rotation. Ultimately, the stepper motor was deemed unsuitable because it would constantly resonate about a given control point. Additional problems were encountered with hysteresis in stepping clockwise and then immediately counterclockwise. This manifested in missed steps or microsteps. Email conversations with Lin Engineering [53] determined that due to the high inductance of the motor, it may not commutate properly in the speed range of 0-0.75 rotations per second. This is the desired operational range, so another solution was necessary.

The final implemented method of controlling the combustion air damper position was with a Curtiss-Wright Exlar Tritex II RDG060 DC rotary servomotor with a 10:1 gearbox and the low-temperature grease option. The mounted solution can be seen in Figure 3.10. Very few issues were encountered with this method during implementation. The servomotor utilized the same style of mounting solution and reference point control as was used with the stepper motor solution. As well, the same rising trigger signal indicated that the servomotor should step a finite degree increment, programmable by the user inside the servomotor, with an estimated absolute rotary position tracking completed by the PLC.

A third closed-loop PID controller was used with the combustion air actuator to set the desired quantity of excess oxygen in the exhaust gases. The

wide-band automotive lambda sensor was used to feedback the quantity of excess-oxygen detected.

FIGURE 3.10: RDG060 servomotor as installed to control combustion air.

A steady state value of excess oxygen was not reached using a PID loop; the measured value instead oscillated about the desired value. This is hypothesized to occur due to the PID loop being inherently unable to compensate for the non-linear effect a non-significant time-delay. Two specific contributors to the time delays are present: (1) the dwell time of the combustion air as it travels through the combustor until reaching the oxygen-sensor; and (2) the time delay of the two Nernst-cells within the oxygen sensor.

3.5 Safety Controls

Several safety controls are implemented on the PLC for 70M TEXHEATER process heater. These controls are coded implementations of legacy guidelines and safety equipment that predate the CDC project described in this thesis.

These legacy safety limits, implemented in code, include an automatic shutdown of fuel to the process heater if a preset temperature of 394.25 K (121.1 °C) was exceeded, measured by the Kimray temperature sensor, or if the process fluid flow rate dropped below a specific set point, measured by the flow switch discussed below. Additional legacy operating guidelines implemented in the PLC include: (a) a maximum heater inlet pressure of 517.1 kPa (75 psi); (b) a minimum heater outlet pressure of 103.4 kPa (15 psi); and (c) a maximum inlet temperature of 333.15 K (60 °C) to the heater. If any of the safety limits or operating guideline limits are violated, the PLC will cut all fuel supply if the heater is operating and/or not allow the fuel pressure to rise above 0 kPa.

The fuel cut-off was enabled using a Magnatrol Valve Corporation normally closed (NC) solenoid 'guillotine' valve on the diesel fuel line downstream from the fuel pump, but upstream from the fuel flow rate actuator. The mechanical flow switch redundantly verifies process fluid flow together with the pressure sensors limits, discussed earlier, in the case of a blockage or partial-blockage within the heater coils. In that case, the pressure limits on the heater inlet and outlet may not be violated but the mechanical flow switch would sense that there is no fluid flow. The mechanical flow switch is a FSW-41A solenoid switch with an adjustable fluid velocity set point as manufactured by Omega Engineering.

3.6 Closure

The complete sensor and actuation package on the experimental apparatus has been presented and is summarized in Figure 3.1. Challenges encountered during

implementation of specific sensing and actuation methods have been covered for use in future work subsequent to the conclusion of this study.

Chapter 4

Algorithm Methodology

4.1 Introduction

While the sensor and actuator package alters and senses the physical operating state of the heater, an algorithm to predict and optimize the state of the heater in an 'intelligent' manner is required. This chapter describes the complete operation, setup, and specifics of the predictive-optimal algorithm employed to optimize the thermal efficiency of the process heater. The components were selected and incorporated based on the literature review presented in Chapter 2.

Given the sensors and actuators selected in Chapter 3, Table 4.1 below, outlines the controllable inputs and responding output, which collectively define the operating state of the heater.

TABLE 4.1: Expected physical quantity ranges for sensor selection.

Physical Quantity	Symbol	Units
Fuel Pressure	p_f	kPa
Atomizing Air Pressure	p_a	kPa
Exhaust Composition (O_2)	γ	%-excess air
Thermal Efficiency	η_{th}	%

The output state, the thermal efficiency, is calculated according to

$$\eta_{th} = \frac{\rho_f Q_f LHV_f}{\rho_w Q_w c_{p,w} \left(T_o - T_i\right)} \tag{4}$$

where ρ_f and ρ_w are the density of the fuel and process fluid (generally water) respectively, Q_f and Q_w are the flow rates of the diesel fuel and process fluid respectively, LHV_f is the lower heating value of the diesel fuel, $c_{p,w}$ is the specific heat capacity of the process fluid, and finally T_o and T_i are the respective outlet and inlet temperatures of the process fluid from the heater.

The quantities in Table 4.1 and equation (4) are the respective input and outputs variables for all components of the algorithm.

4.2 Algorithm Components

Within the predictive-optimal algorithm, there are three primary components: (1) modeling of the process heater using a neural network; (2) optimization using a genetic algorithm; and (3) the refinement of the search space for both the neural network and the genetic algorithm. The iteration and process flow of the algorithm using these three components shall presented in Section 4.6.

4.3 Neural Network

An artificial neural network (ANN), is a black-box technique whose theory is motivated on the complex, nonlinear, and parallel computation capabilities [31] of the biological brain. The ANN functionality resembles that of the brain in two ways: knowledge/data can be acquired via a learning process; and knowledge/data can be stored [31]. Artificial neural networks offer many useful computational properties including: nonlinearity; input-output mapping; adaptivity; fault tolerance; and evidential response [31]. Despite these capabilities, they require fewer adjustable parameters compared to classical approximation methods like Fourier transforms, spline functions, and linear or polynomial regressions [54].

The ANN itself is classified by: (i) the components and functions within the computational neuron (typically held constant within a given layer); (ii) the

number and size of layers (input, hidden, and output generally); (iii) how each layer is connected/structured; (iv) and finally, how the network learns [31]. It should be noted, however, that these classifications themselves are not always exclusively determined. For example, the structure and learning process of the network are intimately linked and if one is fixed, the other has a limited subset of available options [31].

4.3.1 Computational neuron

An ANN is composed of multiple layers of an interconnected, basic computational unit, the neuron. A computational neuron, ("neuron" or "node"), is composed of three parts as shown in Figure 4.1: (i) a set of synapses/connections, characterized by a weight value, $w_{ji}^{(l)}$, which connects neuron j in layer l which in turn receives inputs from neuron i in layer $l-1$; (ii) a summation unit that adds the input signals together, weighted appropriately by their synaptic weights; and (iii) an activation/squashing function, $\vartheta_j(\cdot)$, which maps and/or limits the output signal of the neuron to a finite value. There is also an optional external bias, $b_j^{(l)}$, that increases or decreases the input to the activation function. The j^{th} neuron (in layer l) is described by

$$v_j^{(l)} = \sum_{i=1}^{m} w_{ji}^{(l)} y_i^{(l-1)} \tag{5}$$

and

$$y_j^{(l)} = \vartheta_j\left(v_j^{(l)} + b_j^{(l)}\right) \tag{6}$$

The activation function in equation (5) is typically either a sigmoid function, a piecewise- or straight- linear function, a threshold function, or a Gaussian function [31]. In all equations regarding artificial neural networks in this work, the subscript notation is that: (i) the j^{th} subscript notation indicates the layer of current concern/calculation; and (ii) the i^{th} and k^{th} layers are immediately adjacent to the

left and right (or backwards and forwards), respectively, of the current j^{th} layer assuming a signal propagation from left to right.

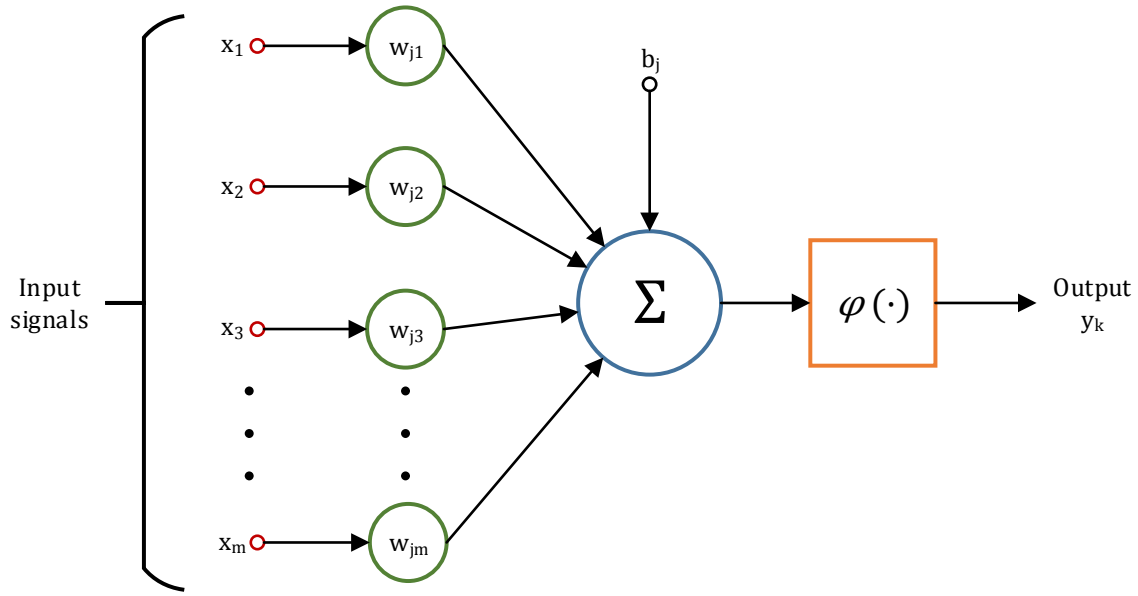

FIGURE 4.1: Computational model of a neuron for an ANN.

4.3.2 Network structure

Neural networks are classified according to their structure or architecture, which ranges from a single neuron, as seen in Figure 4.1, to multiple neurons divided into more than one layer. The layer, l, of nodes that receive the input signal or input vector is known as the input layer and usually does not contain any computational neurons [31]. Conversely, the final layer, L, often consists of a singular computational neuron that outputs the response to the supplied input pattern/vector; this layer is known as the "output layer." The layers between the

input and output layer are colloquially known as hidden layers. One or more hidden layers, not directly system inputs or outputs, enable the neural network to extract higher-order statistics which would otherwise be missed with simpler structures [31]. Figures 4.2 (a) and (b) illustrate a neural network with a single input layer with three neurons, a single hidden layer with five neurons, and an output layer with just one neuron. The lines connecting neurons represent a signal path or connection between neurons.

Neural networks are also classified according to how the neurons are connected; they can connect to each and every neuron in the next adjacent layer (fully-connected) or be selectively connected, as shown in Figures 4.2 (a) and (b), respectively [31], [55]. Additionally the neurons can feedforward to the next layer, or be recurrently connected to a previous layer in a feedback loop as shown in Figure 4.2 (a) and (c), respectively. A recurrent ANN with feedback loops can involve the use of a unit-delay element/operator as denoted by z^{-1}. Figure 4.2 (c) shows the feedforward of the input signal and the feedback of one of the output signals which is accordingly used as an input signal.

With a feedforward type of network, the output from each preceding layer forms the inputs for the next adjacent layer of neurons. A common exception for this (which also holds for most network structure classifications) is the input layer, which does not transform the input signal as there is no previous layer. Instead the signal is received and transformed by the computational neurons in the next adjacent layer.

In most ANN forms, the number of neurons in the hidden layer determines the learning 'capability' of the network [56]. Using too many or too few neurons in the hidden layer causes under- and over- generalization of the problem, respectively [56]. It therefore becomes a process of trial and error to determine a 'good' number of neurons in the hidden layer although empirical formulae provide a starting point, as in

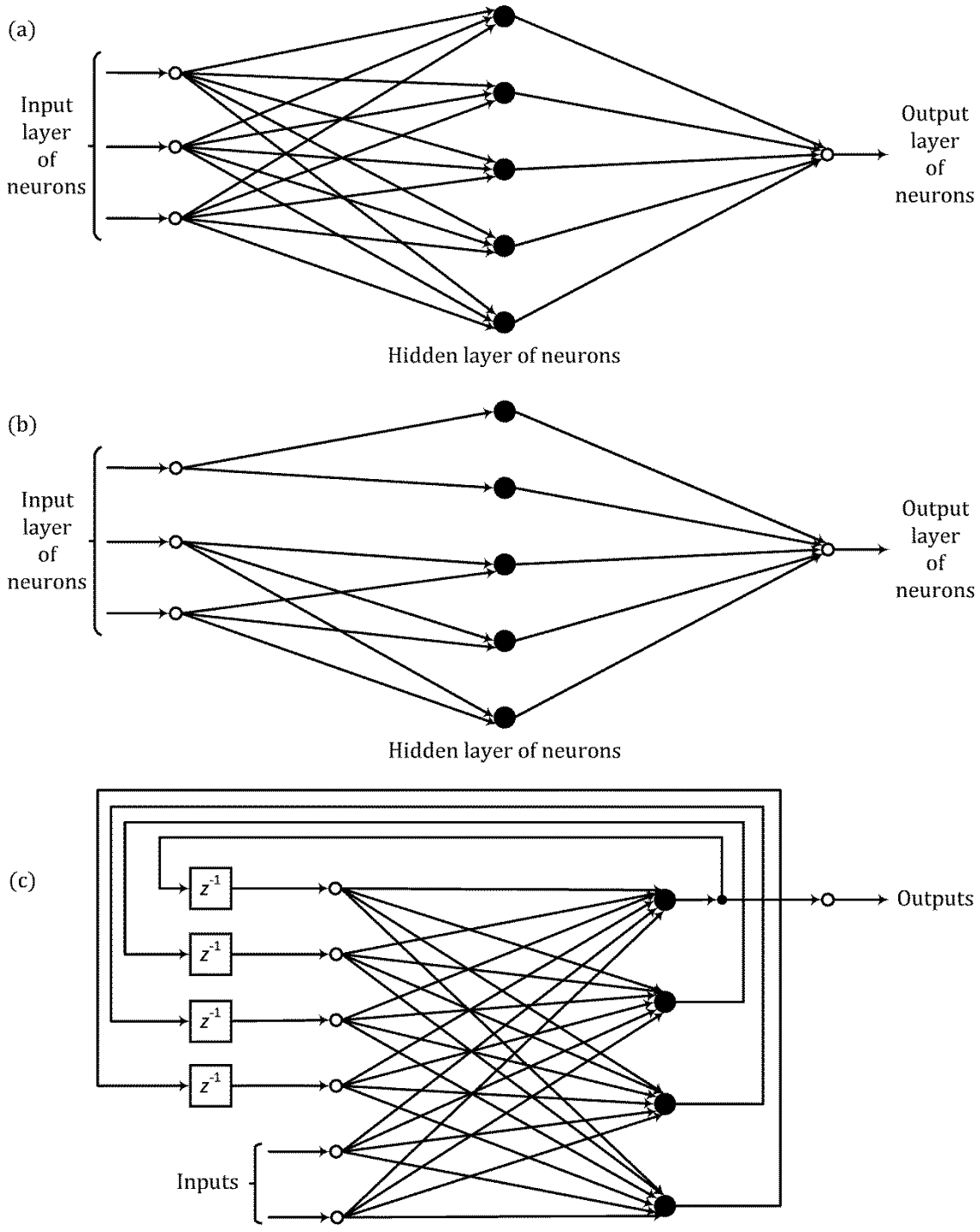

FIGURE 4.2: Classifications of neural network structures.

$$N = \frac{I + O}{2} + \sqrt{P_i} \tag{7}$$

where N is the number of neurons in the hidden layer, I is the number of input nodes, O is the number of output neurons and P_i is the number of training patterns [57].

Within this work, all explanations regarding the operation and training of artificial neural networks will be performed with a fully connected feedforward neural network with one or more hidden layers; a type of structure that is more commonly known as a multi-layer perceptron (MLP). It is one of the most commonly used ANN structures [54].

4.3.3 Network learning

Once the ANN architecture has been defined, the weights and biases, known as the *free parameters*, of each neuron must be adjusted so that that the ANN correctly relates the input to the outputs; this adjustment process is referred to as "training" the ANN. A large set of reference data must be generated, which is then divided into subsets of data for use in training. The division and use of these sets is further described in Section 4.3.4. The training data is presented to the network with each exposure/iteration of the complete set of training data is colloquially called an *epoch*.

Training of the ANN amounts to finding the free parameters that minimizes the discrepancy between the desired output, from the reference data set, and the actual output observed from the ANN [31], [55]. One of the most common and efficient ways to train the network and allow the ANN to learn the patterns presented, is through back-propagation (BP) [31]. BP involves two distinct operations, proceeding forwards and then backwards through the layers of the network. The error is calculated (forwards) from the training data presented to the input neurons, and then later the output neurons, which is then transmitted

(backwards) through subsequent layers from the output neurons [31]. Typically the free parameters start as random values in an interval typically chosen to be primarily on the transition between the linear and saturated ranges of the activation functions with a unity input [31]. The forward pass is detailed below for a fully connected MLP.

Given that vector $\mathbf{x}(n)$ is the n^{th} training data pattern applied to the input layer, $\mathbf{d}(n)$ is the n^{th} training data/desired output vector, $y_j^L(n)$ is the observed output signals (layer $l = L$) for pattern n, and $e_j(n)$ is the error calculated for the j^{th} neuron, then the mean square error (MSE) for the entire network, E, may be calculated by

$$E(\mathbf{d}, \mathbf{w}, \mathbf{x}) = \frac{1}{N} \sum_{j=1}^{N} e_j{}^2 \tag{8}$$

and

$$e_j(\mathbf{d}, \mathbf{w}, \mathbf{x}) = d_j - y_j^L(n) \tag{9}$$

The root-mean-squared error (RMSE) or sum-squared error (SSE) may also be used in place of equation (8). Together these equations [31] define a multivariate minimization that can be solved by non-linear programming (NLP) or a metaheuristic.

The simplest and most common form of the back propagation algorithm utilizes the first-order steepest descent algorithm to minimize the total error. Each free parameter may be thought of as a dimension in a multi-dimensional error space (with the number of dimensions equal to the number of free parameters), where each free parameter is an independent variable collectively producing an error hyper-surface given by equation (8) and the training data set [55]. A minimum error function can be found by translating along the vector produced by the negative gradient of the error function with respect to the free parameters. This

principle provides the basis for how to adjust the free parameters (backwards pass), in sequential training mode, and is given by

$$w_{ji}(n+1) = w_{ji}(n) + \Delta w_{ji}(n) \tag{10}$$

and a simple version of the *delta* or *Widrow-Hoff rule*,

$$\begin{pmatrix} \text{weight} \\ \text{correction} \\ w_{ji}(n) \end{pmatrix} = \begin{pmatrix} \text{learning-rate} \\ \text{parameter} \\ \eta \end{pmatrix} \times \begin{pmatrix} \text{local} \\ \text{gradient} \\ \delta_j(n) \end{pmatrix} \times \begin{pmatrix} \text{input signal} \\ \text{of neuron } j \\ y_i(n) \end{pmatrix} \tag{11}$$

In equation (10) the local error gradient, δ_{ji} is calculated differently for the output layer and the hidden layers.

$$\begin{aligned} \delta_j^{(l)}(n) &= \frac{\partial E}{\partial w_j} \\ &= \begin{cases} e_j^{(L)}(n)\,\vartheta_j'\left(v_j^{(L)}(n)\right) & \text{for neuron } j \text{ in output layer } L \\ \vartheta_j'\left(v_j^{(l)}(n)\right)\sum_k \delta_k^{(l+1)}(n)\,w_{kj}^{(l+1)}(n) & \text{for neuron } j \text{ in hidden layer } l \end{cases} \end{aligned} \tag{12}$$

From these equations it becomes obvious that the activation function must be differentiable. These computations, both the forward and backwards passes, are performed iteratively for multiple epochs until a specific criterion, a minimum mean-square error or other quantity as discussed later, is satisfied.

The steepest-descent method is characterized by asymptotic convergence; in areas of low curvature (*e.g.,* approaching the solution or an "error valley") the speed of convergence is slow. However, convergence to minima is stable and guaranteed in unimodal functions. A logical and common evolution from the steepest descent method for resolving the error hyper-surface is in the use of the Levenberg-Marquadt (L-M) algorithm, which can be thought of as a combination of the steepest descent and Gauss-Newton algorithms, the latter accounting for the second-order curvature of the objective function [55]. The Levenberg-Marquadt algorithm as extended to traversing the error space of an ANN is represented by

$$\mathbf{w}(n+1) = \mathbf{w}(n) + (\mathbf{J}^T\mathbf{J} + \lambda\mathbf{I})^{-1}\mathbf{J}\mathbf{e}(n) \tag{13}$$

where λ is the regularization parameter and $\mathbf{I}$ is the identity matrix. The matrix $\mathbf{J} \in \Re^{(Q\times Z)}$ is the Jacobian as calculated by

$$\mathbf{J} = \frac{\partial e_q}{\partial w_{ji}} \tag{14}$$

for the q^{th} training data set presented for the full set of Z free parameters [55].

Training can occur in two distinct modes. Within each epoch, the training can occur *sequentially* with the weights being updated after each and every data point presentation [31]. Alternatively, in *batch* training (which is used throughout this work), the weights are updated only after presentation of the complete training data set [31].

The data used to train the ANN is contaminated with measurement noise, so it is important to avoid "over-fitting" the free parameters to noisy data/outliers when determining the weights [58]. A solution to both issues exists by incorporating some filtering into the L-M algorithm through Bayesian regularization, which adds very little computational overhead to L-M minimization. As proposed by MacKay [58] the cost function C is given by

$$C = \beta \mathrm{E}_d + \alpha \mathrm{E}_w \tag{15}$$

where E_d is the "error function" term given by the SSE and E_w is the "weight energy" term given the below equation.

$$\mathrm{E}_w = \sum_z \frac{1}{2} w_z^{\,2} \tag{16}$$

Both β and α are heuristics, and the latter should not be confused with the momentum term often included (but not shown) in equation (10). Similar to typical operation of a L-M algorithm, if the cost function decreases in a given epoch, the recently updated free parameters are discarded and the regularization

parameter in equation (13) is increased by a specified step and vice versa for if the cost function increases. However, instead of updating λ from equation (13) using only a single error quantity, Bayesian regularization uses equation (15) with the non-constant β and α. Rules for updating β and α are provided by MacKay [58] and Poland [59].

A complete flow chart for the L-M method with Bayesian regularization can be seen in Figure 4.3.

4.3.4 Network training and verification

As was mentioned earlier, the data collected to train the ANN may be split into three separate categories divided upon their purpose: training, validation, and testing.

The first of these, the training data subset, takes up the bulk of the collected data set, typically 70% or more. Utilized in the algorithms outlined in Section 4.3.3, the training data subset is used to compute the gradients of the error hyper-surface and to update the free parameters. The validation and testing data sets have similar functions and are used to "test" the performance of the ANN and/or to prevent over-training [31].

Lastly, some pre-processing (and accompanying post-processing) of the input and output data is required to increase the efficiency of the training described in Section 4.3.3. The input and output can be normalized to fall within the range of -1 and 1 or have a mean of zero and a unity variance. The post-processing stage is simply the inverse operation of the normalization calculation used in pre-processing.

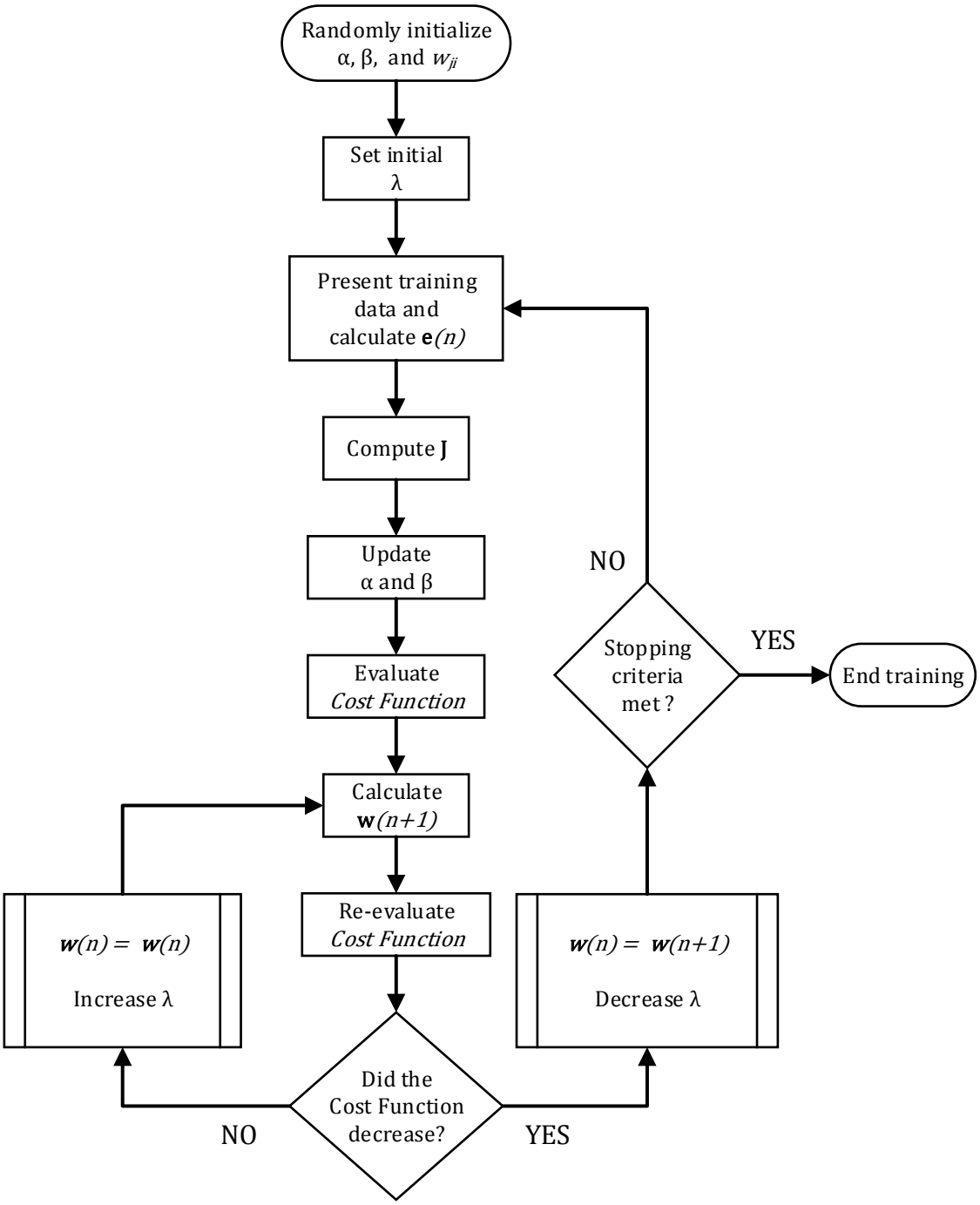

FIGURE 4.3: Flowchart for training an ANN using the L-M algorithm with Bayesian regularization.

4.4 Genetic Algorithm

Once the ANN has been completely trained, it can then be used to simulate the industrial process heater in order to identify an optimal operating state; this is the predictive portion of the algorithm. While it is possible to choose an operating state from univariate parametric plots generated with the ANN model, this process can be computationally expensive for large dimension problems, and more importantly, neglects nonlinear effects between operating parameters. A more rigorous approach is to find the optimal operating point through nonlinear programming, such as the L-M algorithm, but convergence to a global optimum state is not guaranteed if the objective function is multimodal.

Instead, metaheuristic algorithms provide a more thorough search of the operating state space, and are more likely to find the global maximum; the present work utilizes a genetic algorithm (GA). Whereas NLP algorithms update the operating parameters based on the curvature of an objective function at one point on the operating state space, GAs can analyze a large operating state space at each iteration [60], [61]. A GA begins with a population of N possible randomly created solutions, subject to any constraints that define the search-space and corresponding valid operating states. Each iteration effectively searches $\mathrm{O}\left(N^3\right)$ actual solutions [60], allowing efficient searching of large solution spaces with a relatively small population. Randomness and random number operations, inherent in even the initial selection of the initial population, is a core process that continues throughout the entire genetic algorithm.

A genetic algorithm has roots in the real-world process of natural selection and the genetic make-up of organisms [60]. The processes described in the following sections parallels a biological process seen in nature and evolutionary theory.

4.4.1 Fitness function

As discussed in Section 2.6, a quantitative value or objective function, to be minimized (or maximized), is required for optimization. This value, the thermal efficiency defined in equation (4), is one of the most important components of the genetic algorithm; it is used directly to determine the fitness of each member of the population during optimization [60]. The biological equivalent of the fitness function is the literal fitness to survive, as compared to peers of the same generation, in the sense of Darwinian natural selection.

From the aforementioned random initial population, the artificial neural network simulates the process heater, and for each set of input states that comprise one individual member of the population, a single predicted thermal efficiency is computed. As most genetic algorithms only minimize the objective function value, within this work it is therefore necessary to multiply the efficiency by -1.

While the fitness value can be simply set equal to the objective function, it is possible for a select few extraordinary individuals to immediately dominate future generations and thus blunt or undermine the searching capabilities of the genetic algorithm to locate the global optima [60]. Accordingly, scaling of the fitness values is necessary to slow down the possibility of premature convergence, which can be accomplished by mapping the fitness values linearly or with a specified statistical function.

4.4.2 Phenotypes & Genotypes

Before implementing the genetic algorithm on the population of each generation, each input and output state must be encoded in a form usable by the genetic algorithm. Continuing with the parallels with biological evolution, each input and output state, as real numbers or integers, is known as a *phenotype* and is encoded as genetic material or *genotype*. The system model provided by the artificial neural

network utilizes the decoded phenotypes while the genetic algorithm operates solely on the encoded genotypes.

With some forms of genetic algorithms, there is no encoding process; genotypes and phenotypes are the same, and all operations are performed on real/integer numbers. Paralleling the work by Goldberg [60], and to simplify the explanation of the accompanying operations, this work will use binary strings to encode genetic information. Each input state to the artificial neural network is encoded separately to a binary string and is grouped in a genotype structure. All genetic algorithm operations are performed on this structure of individual strings and the resultant structure is decoded back to individual genotypes then phenotypes and used in conjunction with the neural network to output a predicted thermal efficiency. This process is observed in Figure 4.4 below.

4.4.3 Operations

Most genetic algorithms have three simple operations/operators used to create the children of the next generation from the current generation [60]. The three operations are:

(a) Reproduction
(b) Crossover
(c) Mutation

The reproduction operator selects parents from the current population that will go on to produce "children," or members of the next generation. Typically, this is carried out in a manner proportional to the scaled fitness values described by

$$F_i = \frac{f_i}{\sum f_i} \tag{17}$$

where F_i is the probability of selection for the i^{th} member of the population and the denominator is the sum of all the scaled fitness values in a given generation.

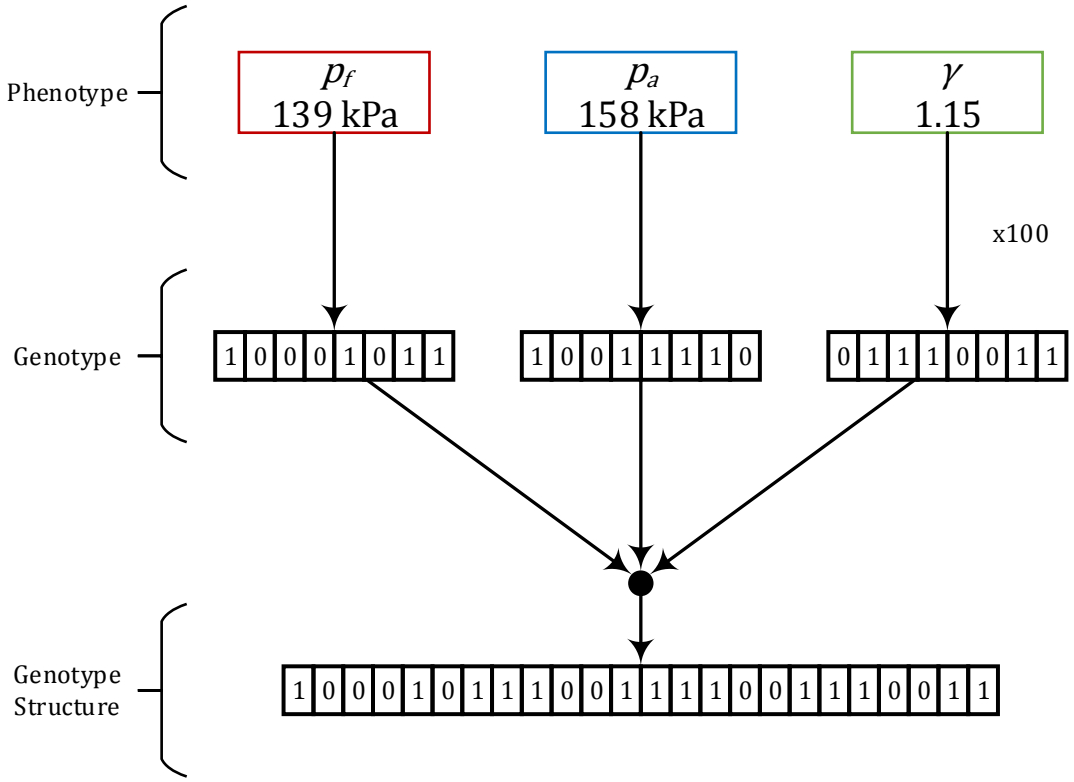

FIGURE 4.4: Genotype and Phenotype conversion process.

An example of this is seen in Figure 4.5 below with a roulette wheel style of reproduction as described by Goldberg [60]. In the figure, a small sample population of just four members is shown on the roulette wheel. The roulette wheel is spun a given number of times, within the limits of the population, to satisfy an adjustable criterion, typically there is an elite count or a minimum number of 'fittest' members that are guaranteed to advance to the next generation (not shown in the example within Figure 4.5). The probability of selection, and 'size' of each member on the roulette wheel, is determined by equation (17) above.

The crossover operator exchanges encoded genetic material between two members of the current generation to form a child for the next generation. The amount of information received by the child, the crossover point, from each parent

is randomly determined. The operation is rather simple for binary genotypes and can be observed in Figure 4.6 (a).

Population Member Number	f_i	F_i [%]
1	408	42.2
2	63	6.5
3	379	39.2
4	117	12.1
Total	967	100

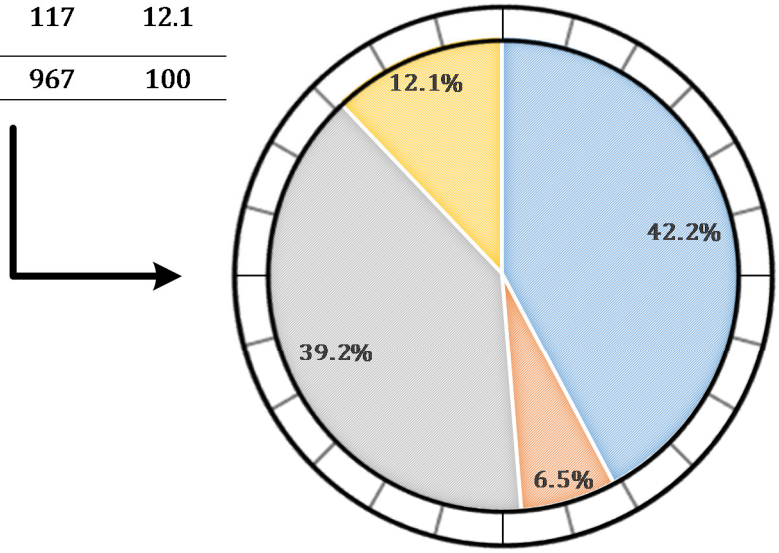

FIGURE 4.5: Roulette wheel reproduction operation.

The final operation, mutation, randomly perturbs the encoded strings of a random member/child of the current generation. For binary encoded strings, this is especially simple as can be seen in Figure 4.6 (b). Mutation and crossover operations are applied at random to members of the population, with a frequency that is set as a parameter of the genetic algorithm.

A complete flow chart for the operation of the genetic algorithm is displayed in Figure 4.7 below.

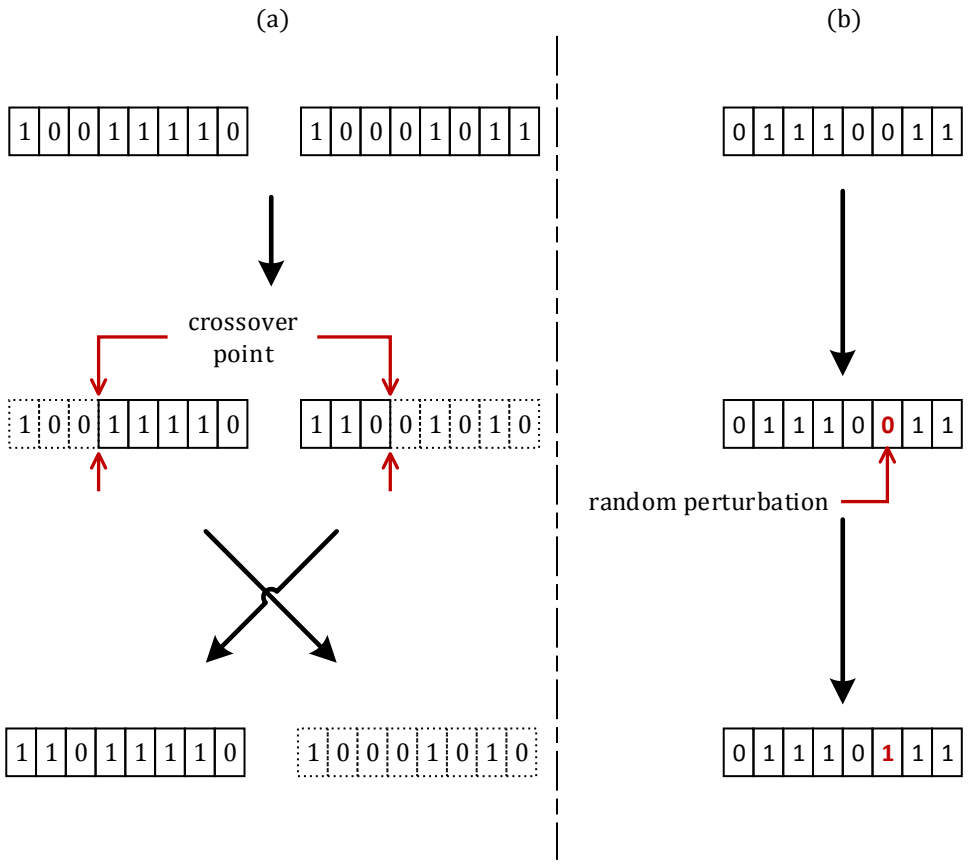

FIGURE 4.6: Genetic algorithm (a) crossover and (b) mutation operations.

4.5 Search Space Refinement

Both the parameters to be optimized and the data collected to train the artificial neural network are constrained to fall within a feasible region defined by a set of constraints. The necessity of these constraints is three-fold. First, the process heater has a known safe operational range of input values determined for equipment life and operator safety. Second, constraining the search space should make the ANN approximation more exact (with less interpolation/extrapolation), resulting in a more well defined topology. Third, constraining the search space reduces the likelihood of the genetic algorithm from "extrapolating," (*i.e.,* evaluating the ANN

model outside of data points that define neural network topology) where it may fail to capture the true problem physics.

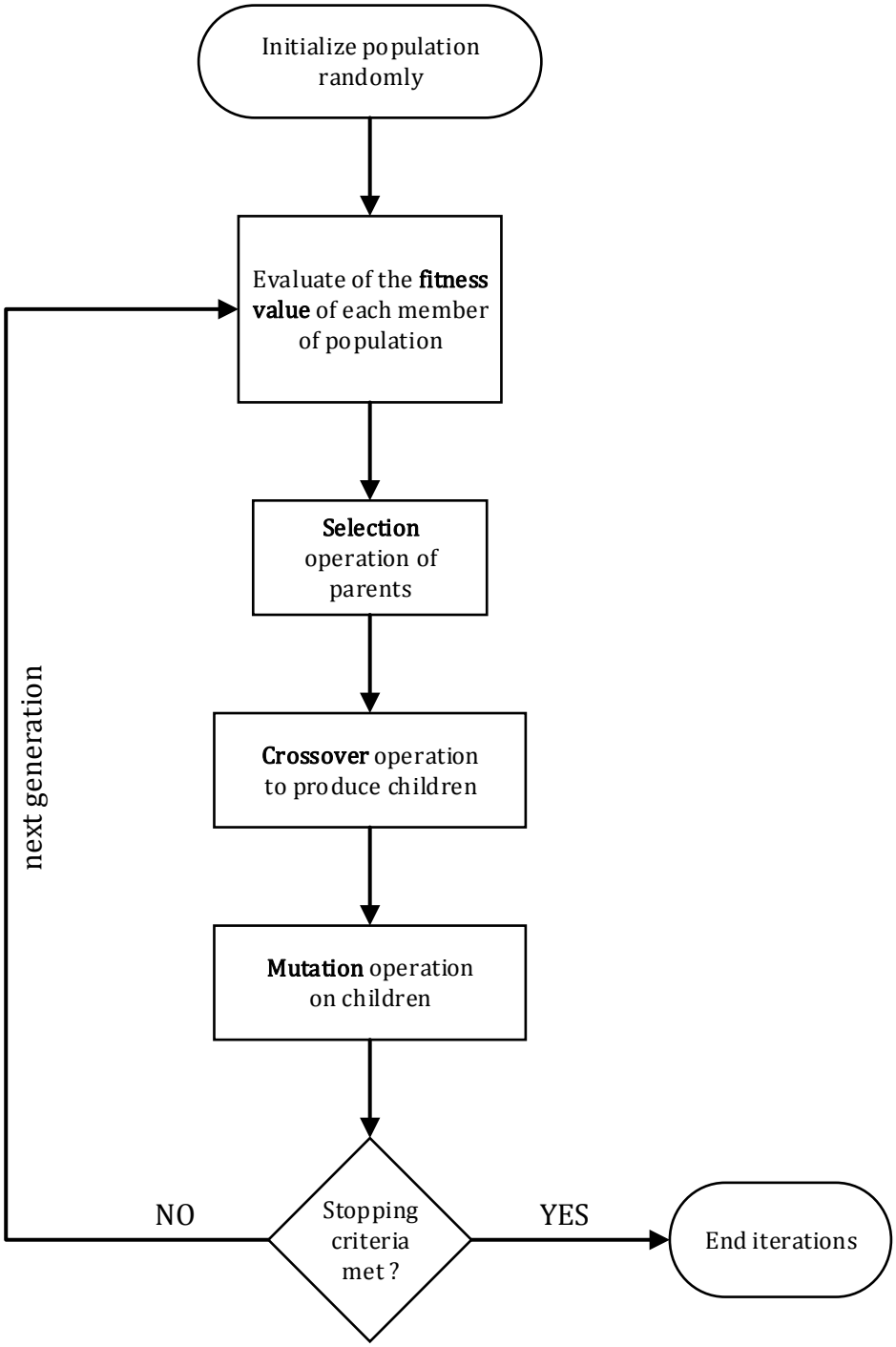

FIGURE 4.7: Genetic algorithm operations flow chart.

The efficacy of constraining the search space can improved by progressively constraining the search space and iterating the three components of the algorithm repeatedly. The control algorithm also adapts to changing environmental and operating conditions (*e.g.,* ambient temperature, fuel composition, heating load), and the performance of the coupled ANN/GA should improve as the neural network is continuously re-trained and updated with new data.

4.5.1 Global constraints

The search space is defined by absolute global constraints, listed in Table 4.2, that cannot be exceeded and bound each stage of the search space refinement.

TABLE 4.2: Global search space constraints

Physical Quantity	Constraint	Units
Fuel Pressure	$p_f \in [138, 414]$	kPa
Atomizing Air Pressure	$p_a \in [138, 448]$	kPa
Exhaust Composition (O_2)	$\gamma \in [1.15, 1.30]$	%-excess air

4.5.2 Refinement operation

The refinement operation borrows a technique of constrained optimization within the response surface modeling (RSM) optimization methods [62]. At each iteration, the constraints imposed on the search space are reduced by a scale factor $Q \in [0,1]$ and re-centered about the predicted best solution, which is the current highest fitness genetic algorithm solution. The initial constraints remain as absolute limits to the problem, while the new constraints are composed of whichever is more restrictive of both the global and new constraints. An example of this is shown in Figure 4.8 for a two-dimensional search space.

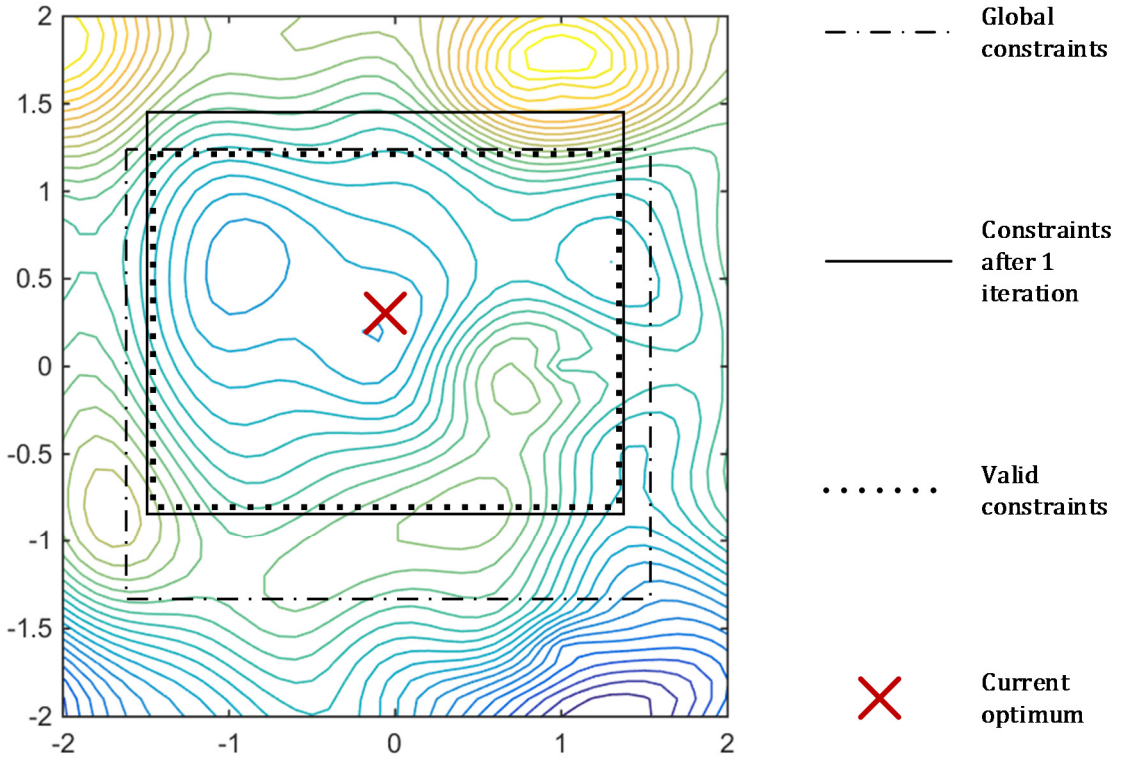

FIGURE 4.8: Example constrained search space after a single iteration.

4.6 Iteration

The complete algorithm is run iteratively. A flow chart describing this iterative process is shown in Figure 4.9. Due to the large length of time necessary to gather data for one single iteration, the refinement operation stops after three iterations. Further investigation is necessary to evaluate alternative stopping criteria similar to that used in the genetic algorithm.

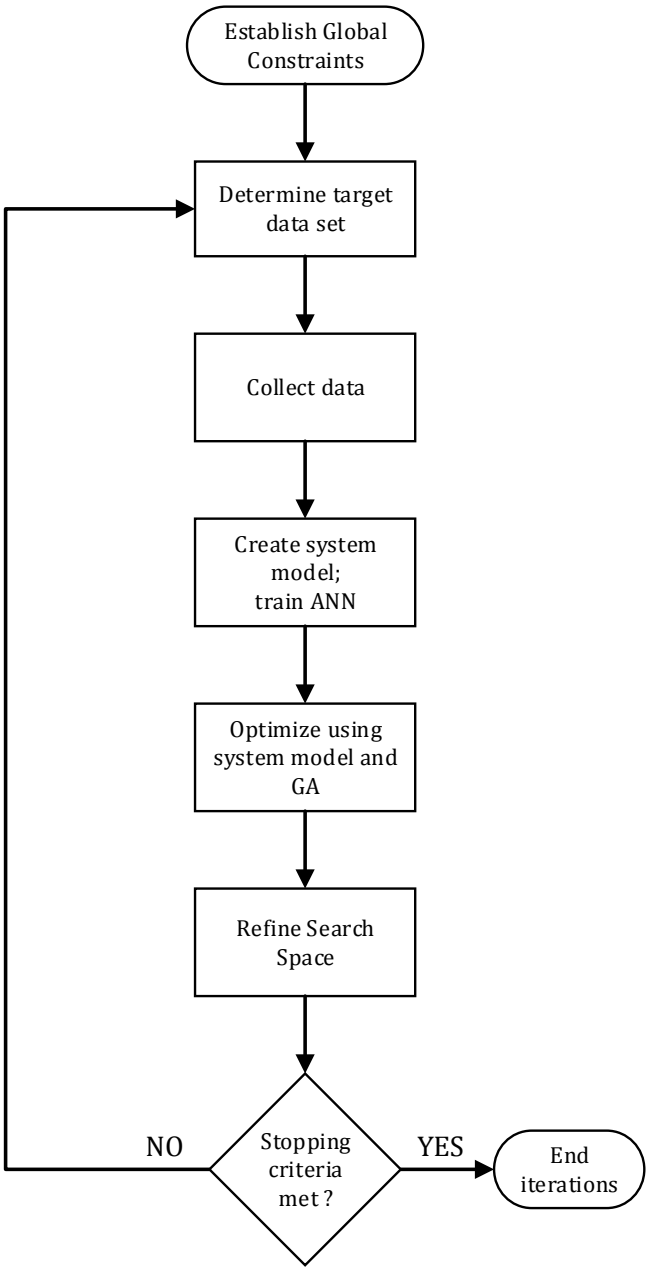

FIGURE 4.9: Complete algorithm process flow chart.

4.7 Closure

Chapter 4 has summarized the three components of the algorithm used to simulate and optimize the operation of the process heater. Each component and the relevant theory/mathematics has been highlighted with the additional explanation of the

continual refinement and adaption of the algorithm. The efficacy of this algorithm will be demonstrated with testing on the process heater in the next Chapter.

Chapter 5

Testing & Results

5.1 Introduction

With the design and implementation of the experimental apparatus (Chapter 3) and the proposed algorithm operation outlined (Chapter 4), the operation and efficacy of both the apparatus and algorithm together requires evaluation. This chapter describes the implementation of the predictive-optimal algorithm and the resulting data recorded from the process heater operation. The algorithm is implemented on the *ifm electronic GmbH* hardware and evaluated in two distinct experiments. Within the first experiment, data is collected and a single iteration of the algorithm is implemented *offline* on a laptop computer. This step serves as a proof of concept of the control and optimization methodology before beginning complete implementation on the PLC controllers. The second experiment, evolving from the previous one and incorporating an online component in the search space refinement from Section 4.5, was carried out *offline* using a laptop computer.

Several physical parameters are needed to calculate the thermal efficiency of the process heater as given in Equation (4). These constants are summarized in Table 5.1.

All testing was performed at GenTex's facilities, located at an approximate elevation of 900 meters above mean sea level.

TABLE 5.1: Summary of physical constants.

Parameter	Value	Units
ρ_w	989	$kg\ m^{-3}$
ρ_f	852.5	$kg\ m^{-3}$
LHV_f	43.2×10^6	$J\ kg^{-1}$

5.2 Offline Experiment

All heat generated from the first experiment was transferred to a 33.3 m^3 tank filled with the process fluid consisting of water and an uncertain and varying quantity of glycol, which is modeled as pure water. The tank is located outdoors and the testing was performed in mid-April; it is worth noting that approximately half of the total volume of this tank was frozen at the beginning of testing. As the experiment progressed, the useable process fluid volume increased as the fluid was heated and the ice melted), but this also altered the water/glycol ratio of the tank. Accordingly, variation to the process heater operating physics is expected but not explicitly addressed in the algorithm. Nevertheless, varying conditions such as varying working fluid composition, as well as changes to the ambient temperature, pressure, and fuel composition, can be accommodated since the ANN is continuously retrained during optimization, as noted in Section 4.5.

The ambient air temperature, atmospheric pressure, and relative humidity ($\overline{T}_{amb}$, $\overline{P}_{amb}$, and $\overline{\phi}$ respectively) are averaged across the entire experiment and displayed in Table 5.2 below. The temperature profile and relative humidity during the first experiment are shown in Figure 5.1; the atmospheric pressure remained approximately constant throughout the test and is not graphed.

For this experiment, the testing was completed at a set of 8 random operating states, within the imposed constraints (see Table 4.2), and the process was allowed to reach a quasi-steady state before data collection. The process fluid flow rate was held approximately constant while the fuel pressure, atomizing air pressure and equivalence ratio were altered for each operating state. The control

TABLE 5.2: Averaged atmospheric conditions during first experiment [63].

Condition	Value	Units
$\overline{T}_{amb}$	272.31	K
$\overline{P}_{amb}$	91.22	kPa
$\overline{\phi}$	82.85	%

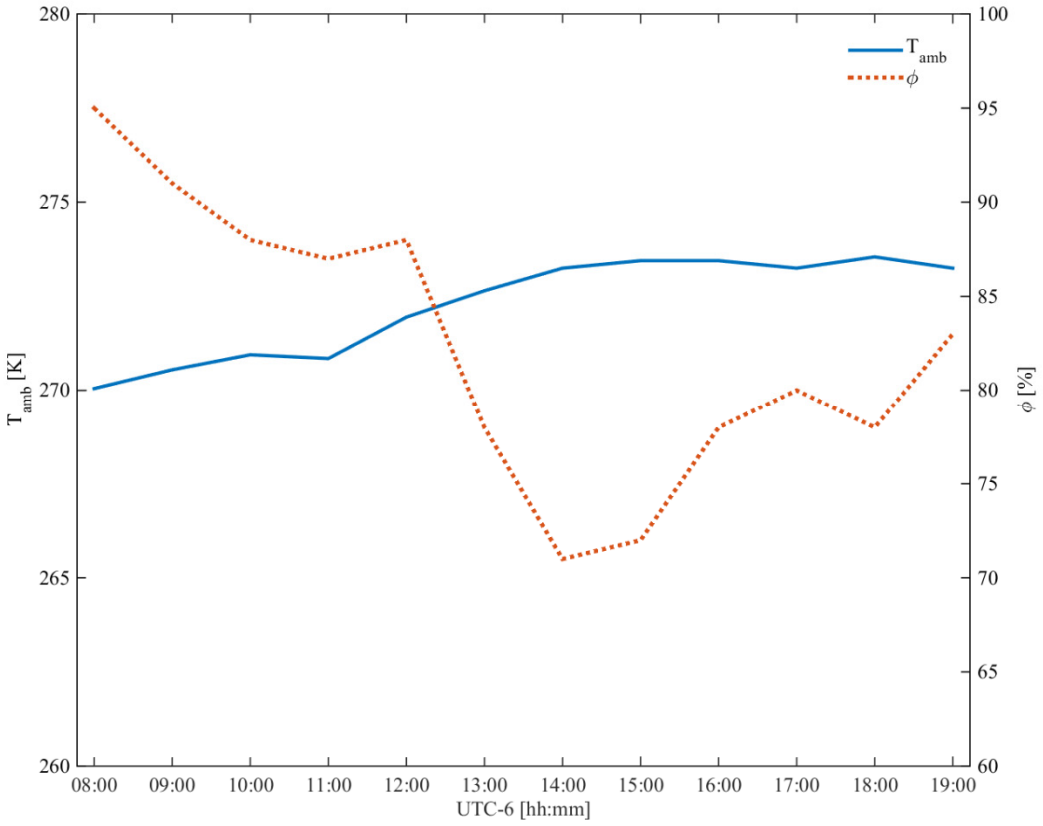

FIGURE 5.1: Atmospheric conditions during testing, offline experiment [63].

inputs were done electronically on the HMI with the exception of the target excess air. At this point in the process heater development, the damper angular position was coarsely controlled by toggling the linear actuator digital inputs while fuel and air pressure were controlled with a PID loop. The linear actuator was controlled manually to obtain the desired exhaust excess air. Data was collected at 10 Hz for

all values and an equal-weighted moving average filter of 25 and 300 data points was utilized for the fuel flow and process fluid flow rates. All other values remain unfiltered post-data acquisition.

5.2.1 Artificial neural network

Using the MATLAB Neural Network Toolbox [64], the artificial neural network is configured with a sigmoid activation function in the hidden layer and an unbounded linear activation function in the output layer. Each input operating state is formed by the three input variables to the neural network, P_f, P_a, and γ, while the predicted output variables are Q_f, Q_w, T_o, and T_i. The intermediate coil temperature is the final predicted variable. The input and output data is pre-processed, as discussed in Section 4.3.2, to have a unity variance and a zero mean. The user controllable settings/parameters for the artificial neural network, as discussed in Section 4.3, are summarized in Table 5.3.

TABLE 5.3: Artificial neural network configuration parameters.

Parameter	Value
Training data set percentage	80
Validation data set percentage	10
Testing data set percentage	10
Maximum number of epochs	1000
Stopping criteria (MSE target)	1.0×10^{-5}

For a neural network with 36 neurons in the hidden layer, the training performance with the above settings is plotted in Figure 5.2; it is observed that the training data did not reach the MSE target criteria and instead stopped after the maximum of 1000 epochs. This will be discussed later.

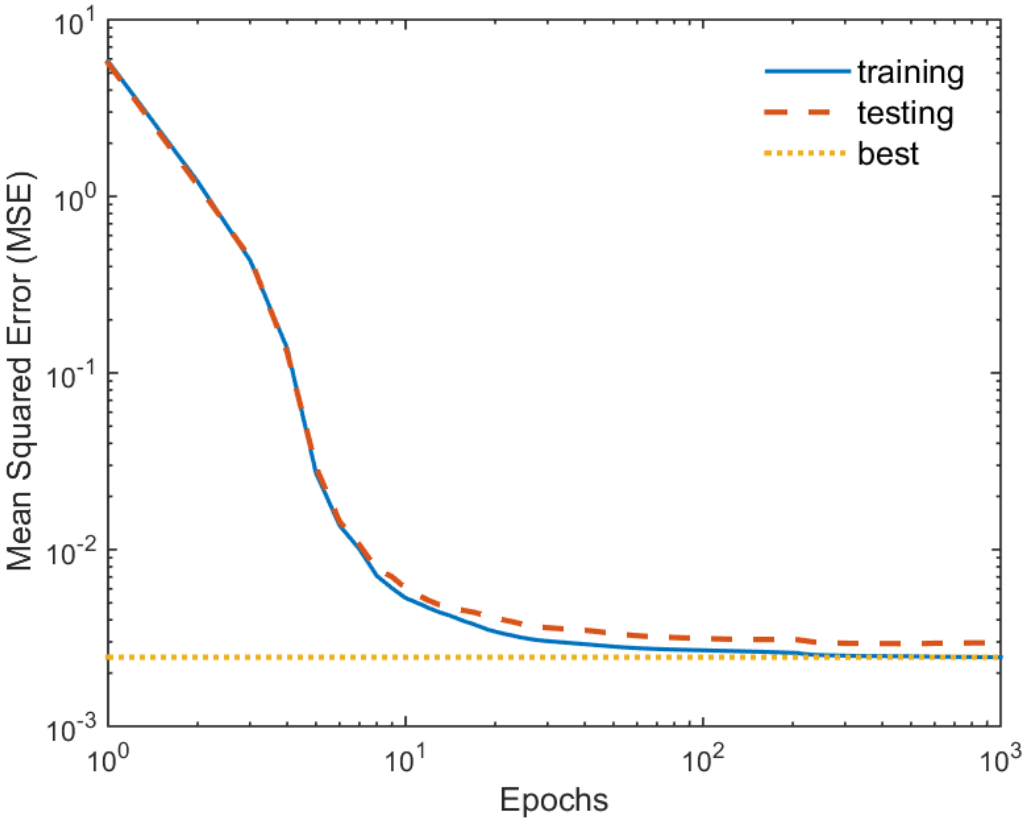

FIGURE 5.2: Example ANN training performance using 36 neurons in the hidden layer.

The number of neurons in the hidden layer affects the predictive capabilities of the ANN; Figure 5.3 (a) and (b) plots the measured and predicted thermal efficiencies using 4 and 36 neurons in the hidden layer respectively. As was mentioned in Section 4.3, larger numbers of neurons in the hidden layer enhance the ability of the ANN to capture higher order patterns, which is needed to emulate the combustion physics, and consequently the predicted thermal efficiency. The increase in prediction accuracy for 36 hidden neurons is shown in Figure 5.3. Through trial and error, 36 neurons in the hidden layer was chosen to provide a balance between computational time and the prediction accuracy.

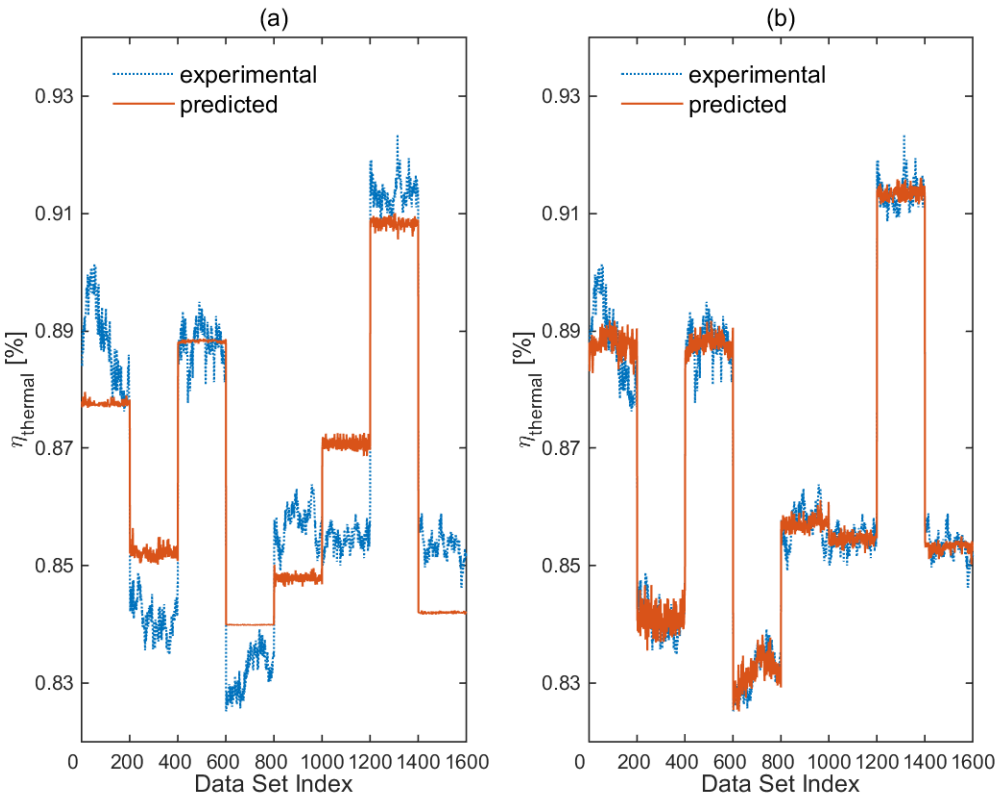

FIGURE 5.3: Experimental and predicted efficiency with (a) 4 neurons and (b) 36 neurons in the hidden layer.

5.2.2 Genetic algorithm

Now that the artificial neural network is completely trained, the genetic algorithm, making use of the global optimization toolbox in MATLAB [64], is initialized with a population of 75 candidate random operating states, determined to be sufficient through trial and error. Each member of the population is made up of the three individual input parameters of the trained artificial neural network. The output variables, from the prior trained artificial neuron network, are used to calculate the thermal efficiency defined in equation (4). This is value is then optimized by the genetic algorithm.

The genetic algorithm heuristics, as described in Chapter 4, are included in Table 5.4 below. Additionally, beginning with the initially generated population

and at all times after with every operation of the genetic algorithm, the input operating states are constrained to fall within the feasible region defined by Table 4.2.

TABLE 5.4: Genetic algorithm configuration parameters.

Parameter	Value
Maximum number of generations	100
Probability of crossover	0.7
Probability of mutations	0.01

Figure 5.4 displays the progress of the genetic algorithm in terms of the objective function, $F(x)$, which is set equal to $-\eta_{thermal}$, so the minimum of $F(x)$ corresponds to the maximum thermal efficiency. Figure 5.5 presents the evolution of the input operating parameters as the optimization progresses. It is worth noting that the genetic algorithm is non-deterministic and the output of the optimization will vary with each optimization using a given or fixed ANN/data set.

The first thing to note is that the predicted values exceed 1.0 (-1.0 in the figure due to the GA minimization), which is obviously nonphysical. The accuracy of the ANN is limited by the finite number of sampled values presented to the network, and, as noted above, is subject to uncertainties in operating parameters. This limitation has a minimal impact on the outcome of GA minimization, however, since the relative performance of the algorithm is important to improving the operating efficiency of the heater, and not the predicted absolute values. In other words, the true efficiency of the heater is not crucial; rather, only the relative magnitude of the efficiency at each operating point is required to 'trend' towards the real optimum efficiency. Regardless of the predicted thermal efficiency, the input operating states are still bound by the constraints outlined before.

In an attempt to address the non-physical predicted thermal efficiency for later testing, it was hypothesized that there is a deficiency in the training data set and that the training data does not adequately cover the relevant state space. From

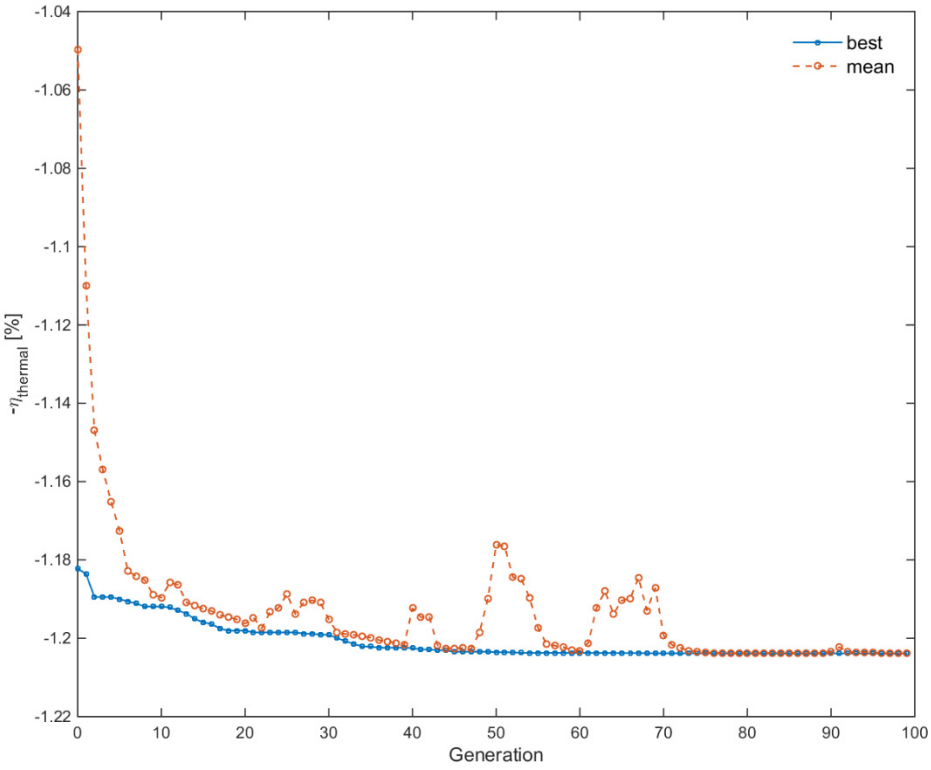

FIGURE 5.4: Progress of genetic algorithm optimization, offline results.

gathered experiential knowledge, this first test had a relatively small number of unique data points relative to the number of free parameters within the ANN. Specifically, the 1600 data points being used for training only represents 8 unique operating states. While these operating state are each comprised of 200 data points, there are still only 8 unique operating states. Consequently, the hypersurface produced by the artificial neural network is being trained/fit to the 200 data points of noise/variance at each of the given 8 operating states. The ANN is therefore being trained to predict the variance at each of these unique operating states instead of the state itself. The above hypothesis and reasoning is supported by results obtained from the next round of testing in Section 5.3. The final optimized input parameters output from the algorithm, despite the deficiencies noted above, still trend with what is known by GenTex personnel to produce 'good' efficiencies

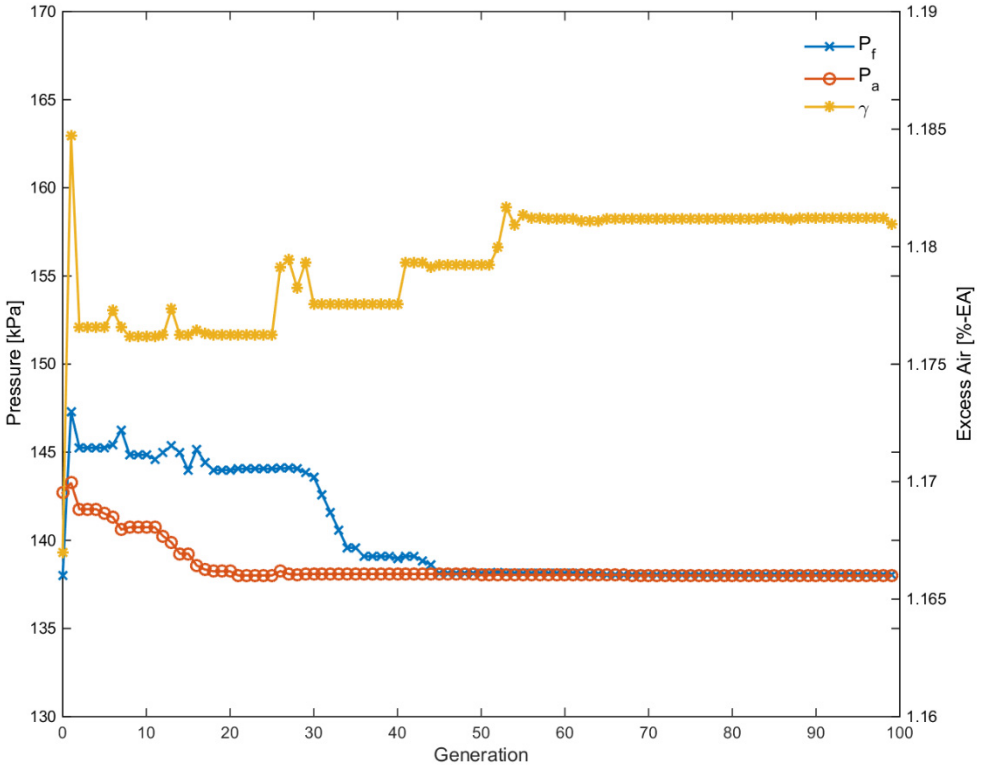

FIGURE 5.5: Evolution of the input parameters during optimization, offline results.

based on empirical experience. Thus, it was decided to continue using the artificial neural network to predict the operation of the process heater. As noted above, however, both the predictive capabilities of the ANN and the quality of the optimal state identified with the genetic algorithm will improve by increasing the number of experimental operating states used for training per iteration.

Testing time on the dynamometer is limited because the process heater is incorporated into a closed loop of working fluid (*i.e.,* recirculating water to and from a tank) and due to the large thermal output of the heater, the process fluid increases in temperature rapidly. As was mentioned in the context of the safety controls, the process heaters have a maximum inlet temperature. Even with typical use in customer applications, there is a finite amount of time available to cycle through the three components of the algorithm. Thus, it is necessary to maximize

the number of training states in a fixed testing time period. The characteristic rise time for the process heater, as a whole system, to settle to an approximately steady state value when the input parameters change is unknown, but was previously estimated to be above 300 seconds. This is the range used to collect data up to this point in Section 5.2. Characterizing this time is necessary to maximize and/or validate the rate of data collection for the artificial neural network.

5.2.3 Characterizing the time response

The time for the process heater to reach steady state after the operating parameters have been changed must be established in order to maximize the number of distinct set of data available to train the ANN. Six operating states were selected for testing to produce five time responses for analysis. The input operating states for time response testing are shown in Table 5.5 below. The process fluid flow rate was held constant during this experiment at a typical value and the fuel and atomizing air pressures were set equal. The operating states change were performed sequentially in the order in Table 5.5, and the operating state was held for a minimum of 300 seconds before changing to the next data point to allow the unit to reach an approximately steady state output.

TABLE 5.5: Time response experiment input operating states.

Operating State Number	P_f / P_a [kPa]	γ [%-EA]
1	138	1.4
2	207	1.19
3	276	1.19
4	207	1.19
5	138	1.36
6	276	1.16

The calculated thermal efficiency was used as the system response to determine whether or not process heater had reached steady state. The time to

reach 95% of this value was taken to be the response time of the system. The results of these calculations are shown in Table 5.6; the mean response time is approximately 138 seconds.

TABLE 5.6: Measured time response experiment results.

Experiment Number	Response Time [s]
1	145
2	140
3	117
4	129
5	161

5.3 Offline-Online Experiment

As mentioned at the beginning of this Chapter, this second experiment is an evolutionary step from the first described in Section 5.2; among other refinements, it incorporates an *online* component in the form of the search space refinement from Section 4.5. Experimentation was performed with the aid of an *offline* laptop computer to complete the artificial neural network calculations and genetic algorithm optimization.

Originally, this experiment was to be performed fully *online* with the algorithm implemented on the *ifm electronic GmbH* CR0232 PLC. A PLC is not designed to be a computing engine and instead is setup to control industrial processes according to simple pre-programmed logical step instructions. At the onset of the project, the manufacturer claimed that the CR0232 PLC would be capable of the task of operating as a computing engine. Unfortunately, it was discovered, during implementation at this stage of the project, that the PLC is equipped with the watchdog function described in Section 3.2.1. This represents a serious impediment to implementing the ANN as all calculations performed within typical programming statements, including 'for', 'while', 'do', and 'if', must be

executed in less than the maximum time specified by the watchdog function. These statements are a necessary part of the repeated calculations performed in all three components of the algorithm. After conversations with *ifm* support personnel, it was discovered that the watchdog function could not be circumvented due to the necessary safety functionality it provides; it is an integral and inseparable part of the operating system on the PLC.

Two potential solutions this issue were examined. The first involved implementing the algorithm within the Linux kernel on the CR0232, but outside of the PLC itself; this was where the algorithm was to be implemented during the early stages of the project. However, implementing any code on the Linux kernel but outside of the operating system on the CR0232 is not supported nor is there any clear method to do this. Because of the above reasons, and the proximity of this portion of the testing to conclusion of the project, it was decided to abandon this avenue.

A second impediment to implementing the ANN is that the PLC does not store the measured operating parameters within its internal memory between loops. To overcome this, the second solution involves storing the data that is used within the aforementioned programming statements (*e.g.,* 'for' loop statements) on retained global variables that hold and retain their value outside of a given program. This solution replicates the internal functionality of these programming statements using external global retain variables; each 'loop' is one occurrence of the program. Passing variables to and from memory like this was expected to slow computation time significantly but still allow implementation. Unfortunately, midway thorough implementation, it was discovered that the CR0232 only has 64 kB of total allocated memory available to all retain variables, which precludes this second avenue as useful solution. At this point, it was decided to implement a partial *offline* solution of the algorithm instead and search for a way to implement the full algorithm *online* at a later date.

The *offline-online* solution, differing from Section 5.2, was performed on a 450 m^3 water tank which was assumed to contain pure water. The experiment was performed over two days with the average environmental conditions summarized in Table 5.7 and the environmental condition profiles shown in Figure 5.6.

TABLE 5.7: Averaged atmospheric conditions, offline-online experiment [63].

Condition		Value	Units
Day 1			
	$\overline{T}_{amb}$	285.61	K
	$\overline{P}_{amb}$	91.72	kPa
	$\overline{\phi}$	68.69	%
Day 2			
	$\overline{T}_{amb}$	285.22	K
	$\overline{P}_{amb}$	92.12	kPa
	$\overline{\phi}$	65.15	%

For this experiment, the first iteration of testing was completed using 12 random operating states, within the same imposed constraints as before. These 12 data points were sampled randomly from user controlled limits on fuel pressure, atomizing air pressure, and exhaust composition. These limits were changed each iteration and new random data points were produced. Each operating state was programed as the target state into the PLC, which automatically adjusted the actuators until the state was reached. Each subsequent online iteration of the search space component of the algorithm requires user intervention to input the optimum value calculated by the offline ANN and GA components.

Data sampling collected for each state after 300 seconds based on the analysis described in Section 5.2.1, and only a single data point was collected consisting of a moving average from the most recent 5 seconds for each quantity. These twelve data points were pooled with values calculated from the 8 data points in the previous experiment. This total of 20 data points form the complete data set used to train the artificial neural network for the first iteration in this

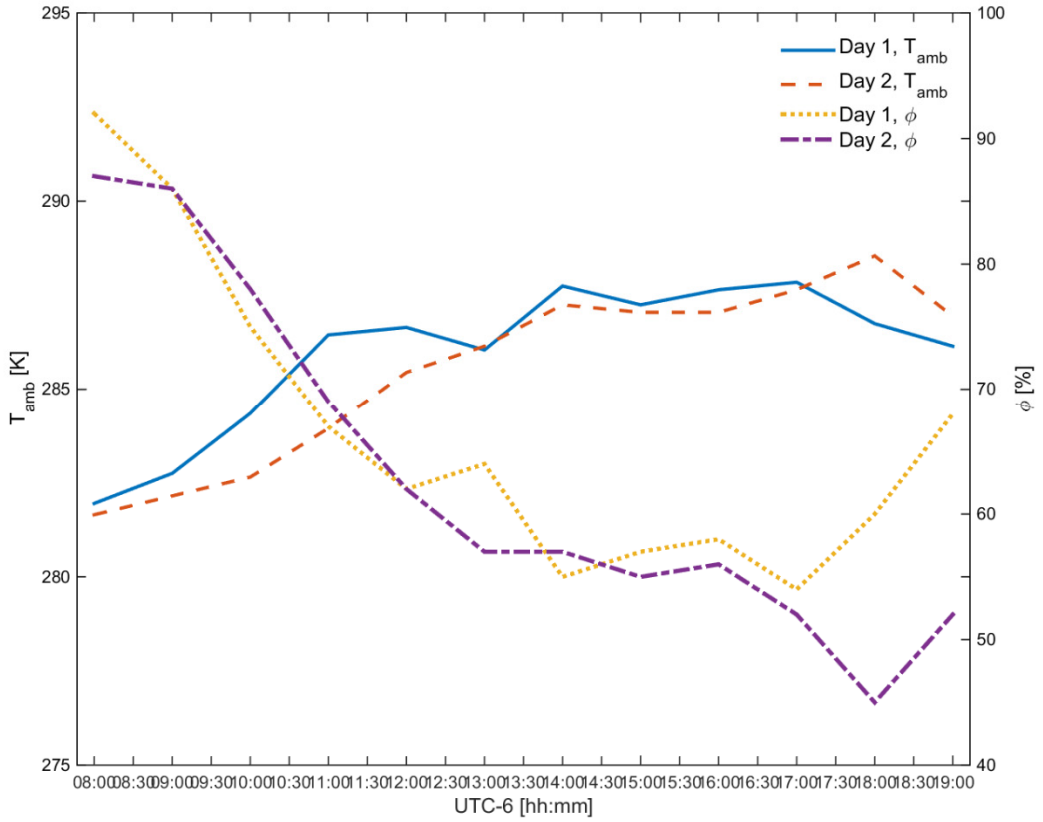

FIGURE 5.6: Local atmospheric conditions during testing, offline-online experiment [63].

experiment. Data was collected at 2 Hz in this experiment, as the previous 10 Hz data rate offered no advantages to this study after post processing the acquired data from Section 5.2. All other setting remain the same as in the offline experiment unless noted. A graphical example of the input operating states and calculated thermal efficiency during the first iteration is shown in Figure 5.7.

The first two iterations were performed on the first day and the third iteration was performed on the third day. All further experimentation was stopped after this point as the testing tank temperature, measured at the inlet of the process heater, had exceeded 323.15 K, a predetermined stopping criterion, since the increasing fluid temperature reduces the heat transfer between the hot combustion gases and the coils, which alter the operating physics of the heater trending towards

a safety limit. As noted above, however, these changing operating physics are also expected under operating conditions, and can be accommodated through the continuous ANN training.

Two items are of note in Figure 5.7. The first is the calculated irregular 'spikes' in the efficiencies. This is an artifact stemming from when the fuel flow rate suddenly drops between operating states, while the thermal output of the heater has a slower response, resulting in an abrupt 'spike' in the thermal efficiency. The second is the noisy exhaust composition signal. As was mentioned earlier in this work, the PID loop control signal on the blower damper position is the target excess air value. There is, however, a significant time delay between a change in the damper angular position at the 'beginning' of the process heater and the response from the exhaust probe at the 'end' of the process heater. The PID loop, as a linear control method, has great difficulty compensating for the non-linearity this rather large time delay causes.

5.3.1 Artificial neural network

Again using the MATLAB Neural Network Toolbox [64], the artificial neural network is configured as described in Section 5.2.1, with three exceptions. First, the efficiency was calculated within the PLC; in this experiment there are 3 input nodes (the same as before) but only 1 output node (the thermal efficiency). This structure would now allow the use of a radial basis function (RBF), a different form of the ANN not discussed within this work to model the process heater [31], [55]. However, it was decided to remain with the existing MLP architecture for direct similarity and continuity between the two experiments.

The second departure from the previous experiment is the 80:20:0 split between the training, validation, and testing data sets. With such a small data set, the use of a testing data set may significantly detract from the overall performance of the artificial neural network by removing data from the training data set. The third departure is in the decrease of the number of hidden layer neurons to

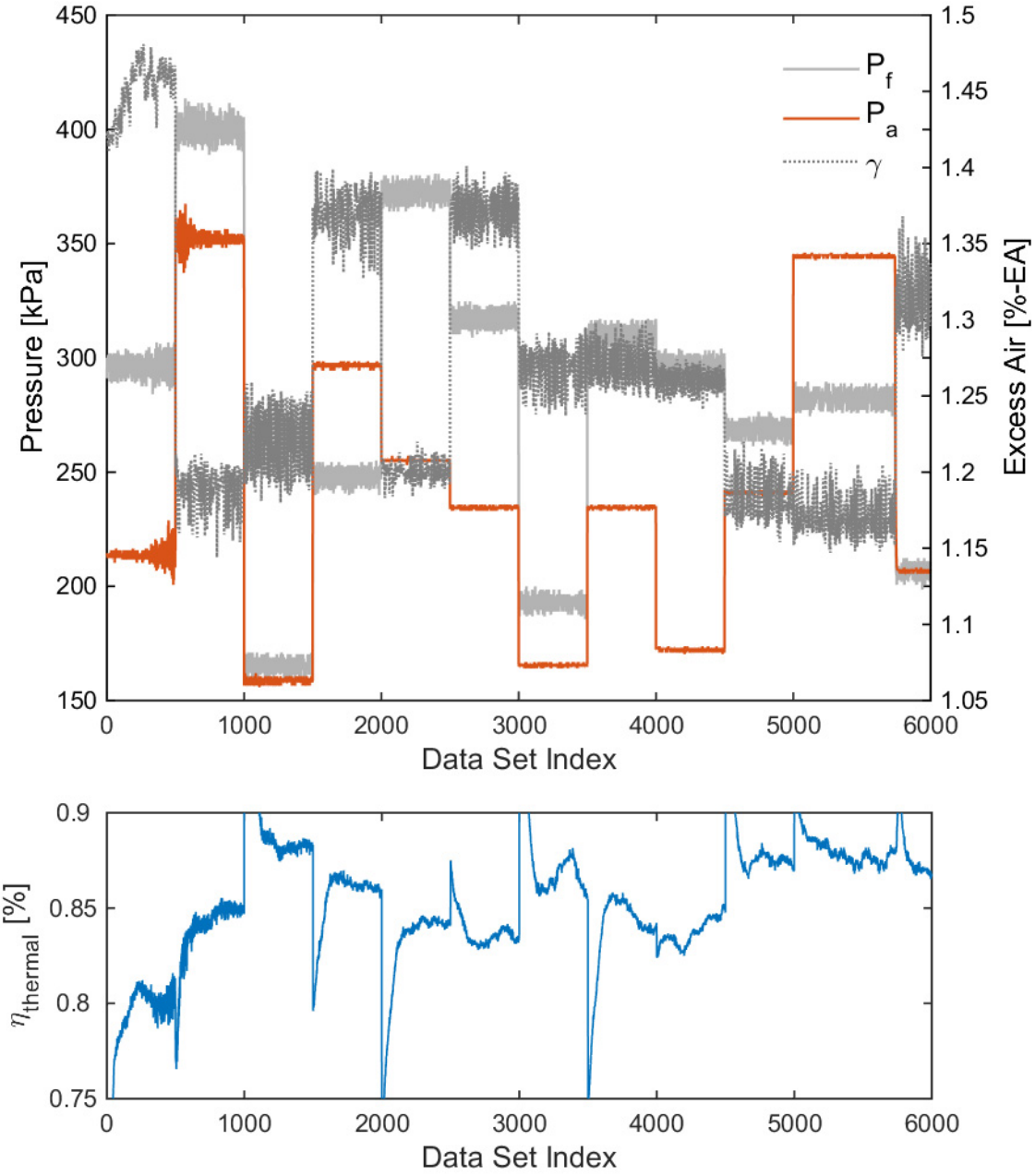

FIGURE 5.7: Data for the first iteration, offline-online experiment.

16 in response to the decreased number of output nodes. This number was again determined through a trial and error process.

The training performance of the artificial neural network with 16 neurons in the hidden layer is shown in Figure 5.8. It is noted that training was stopped before the maximum number of epochs and the target MSE value was reached. Another stopping criterion, the minimum gradient magnitude, was achieved when the gradient of the MSE value dropped below a threshold of $1.0x10^{-5}$ for six consecutive epochs.

5.3.2 Genetic algorithm

Utilizing MATLAB as before, the genetic algorithm is configured with a reduced population size of 15, when compared to the offline experiment. When increasing the population size beyond this value it is observed that the evolution of optimized values, as in the earlier Figure 5.5, would remain perfectly flat across each generation. This indicates that the initial population size is too large, and that the genetic algorithm becomes an enumeration of candidate values instead of a heuristic optimization.

The genetic algorithm progress and evolution of parameters are shown in Figure 5.9 and Figure 5.10 below. The optimized values from this first iteration are 143.0 and 157.0 for fuel and atomizing air pressure respectively and an excess air value of +15 percent. This aligns with two key observations made during the length of this study:

(a) operating the process heater with atomizing air pressure higher than that of the fuel pressure increases thermal efficiency.

(b) decreasing the total heat input directly correlates with a decreases in fuel flow rate and hence fuel pressure, which increases the thermal efficiency on the TEXHEATER 70M process heater.

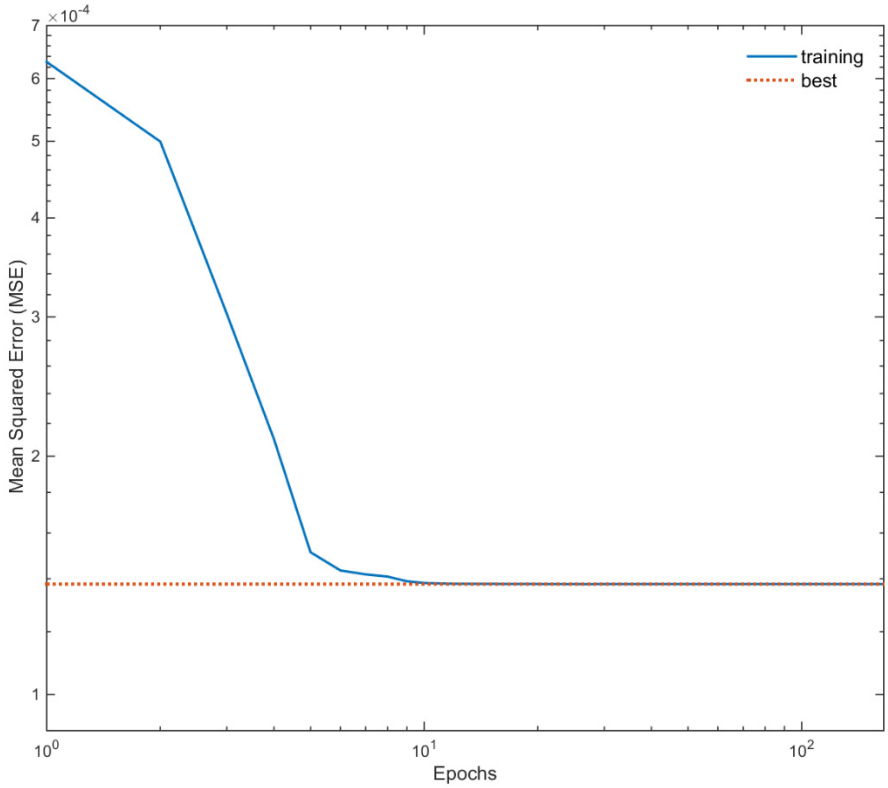

FIGURE 5.8: ANN training performance during 1st iteration of offline-online experiment.

5.3.3 Iterations

With a scale factor Q equal to 0.8 and with a linear reduction of each constraint, the new search space constraints for the next iteration are summarized in Table 5.8. All further iterations are performed with the same algorithm parameters as discussed in Section 5.3.1 and 5.3.2. Each subsequent iteration collects an additional 12 random data points, subject to the updated constraints from the optimum value determined in previous iteration.

The artificial neural network in these subsequent iterations is re-trained with full set of all data collected so far with one subtle difference. If the collected data point is within ±20 kPa on both pressure values and ±1 %-excess air of an already existing data point, that data point is replaced with the updated input values and

output thermal efficiency. This is a further evolution of the predictive nature of the algorithm to increase the efficacy and adaptivity to changing environmental conditions, process fluid(s), and fuel composition.

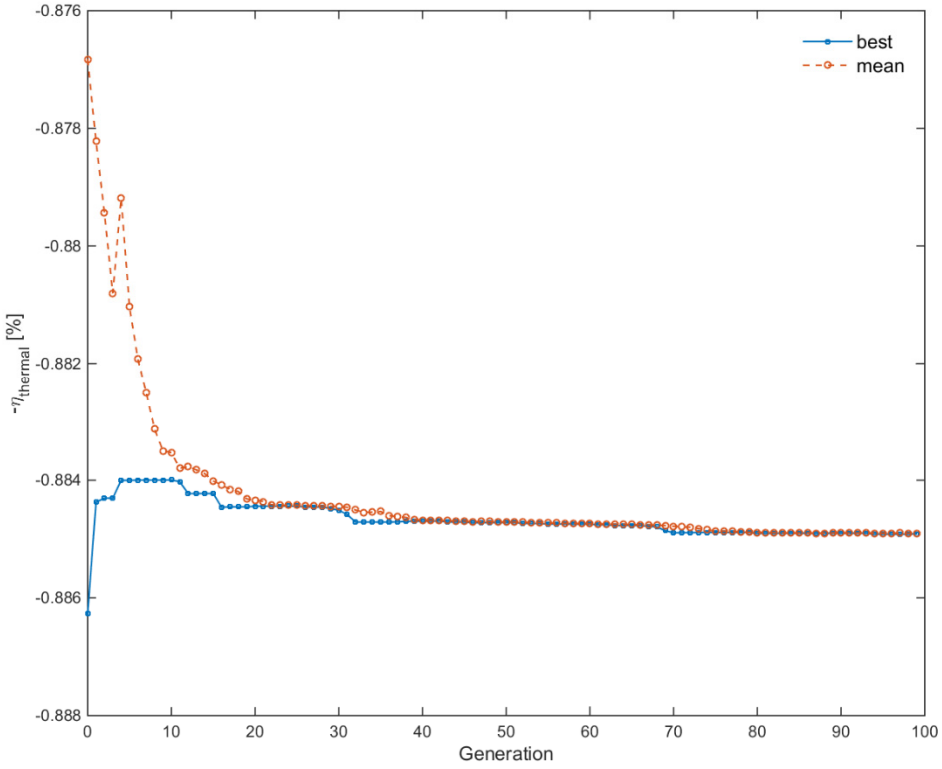

FIGURE 5.9: Progress of genetic algorithm optimization, offline-online results.

TABLE 5.8: Constraints after first iteration, offline-online experiment.

Physical Quantity	Constraint	Units
Fuel Pressure	$p_f \in [138, 253]$	kPa
Atomizing Air Pressure	$p_a \in [138, 277]$	kPa
Exhaust Composition (O_2)	$\gamma \in [15, 21]$	%-excess air

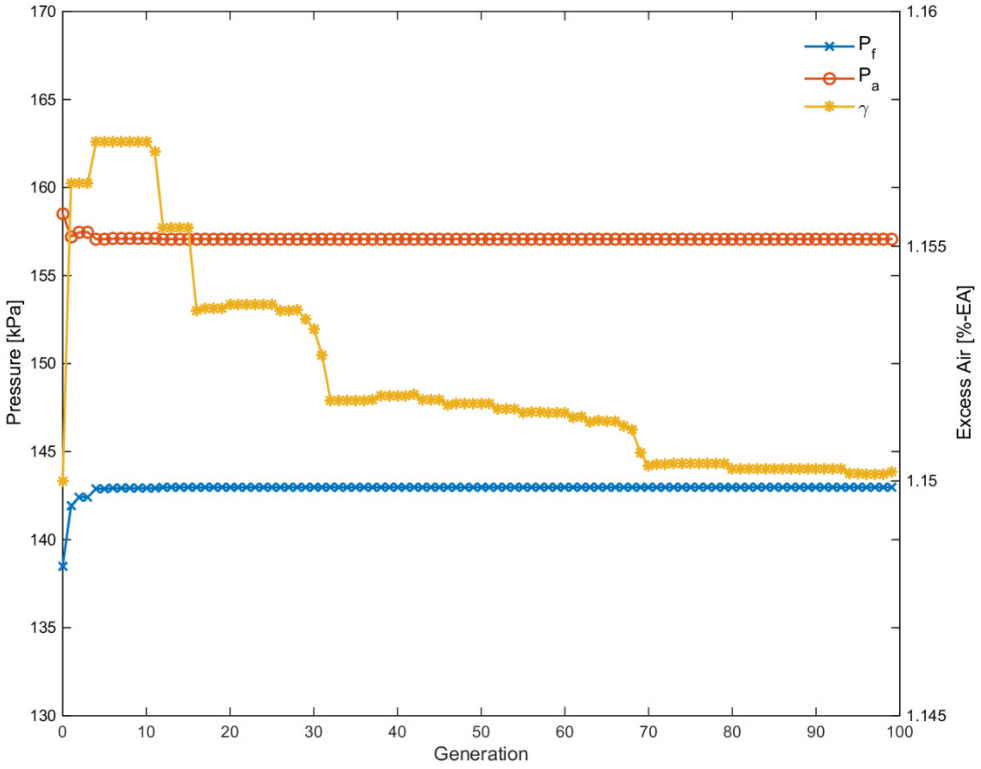

FIGURE 5.10: Evolution of input parameters during optimization, offline-online results.

The final input operating state values and the final optimal predicted thermal efficiency calculated via the genetic algorithm and the updated artificial neural network after three iterations is summarized in Table 5.9. These input operating state values only varied slightly from those in the first iteration. The final predicted efficiency did vary over about a range of approximately 1 percent with the increased data density about the optimum input states. This is because of the increased predictive accuracy of the artificial neural network in that region as more data was collected about that optimum point as the search space was constrained.

TABLE 5.9: Summary of optimization results after three iterations.

Physical Quantity	Value	Units
Fuel Pressure	139	kPa
Atomizing Air Pressure	158	kPa
Exhaust Composition (O_2)	1.15	%-excess air
Thermal Efficiency	87.35	%

5.4 Additional Observations

The optimum theoretical exhaust composition remains at the lower boundary of the global constraints. Lowering the boundary any further than this limit produces an intermittent sooty flame, observed through the flue gas color, due to the oscillatory nature of the damper angular position control. This in turn negatively affects the heat transfer to the process heater in the long term, known from experiential knowledge at GenTex. The coils become *sooted* from too rich of combustion, coating the surfaces of the three coils in carbon-rich partially-pyrolyzed diesel fuel. This increases the resistance to heat transfer of the coils and lowers the thermal efficiency of the process heater as well as fouling the atomizer nozzle and affecting the spray patternization.

While it is currently not possible to know with absolute certainty what is occurring within the process heater during the optimization, a hypothesis can be formed from the data collected during the testing of the algorithm.

From data collected during a study [28] previous to this work and given that the operation of a Y-type atomizer is well documented [13], increasing the atomizing air pressure in this type of atomizer should lead to a smaller droplet diameter. The 'classic' D^2-law [65], [66] simply states that the finer the droplet, the faster the rate of combustion. Logically, it then follows that this leads to a shorter and more intense/higher temperature flame within the process heater for

increasingly small droplet sizes and higher atomizing air pressures. This is, of course, given that all other settings remain constant.

An analysis of the heat transfer modes in another previous study on a GenTex 70M process heater [67] during typical operating conditions where the fuel and atomizing air pressures were held equal. This analysis determined that approximately 25 percent of the gross heat transfer is to the inner coil of the heater via radiation, with an additional 15 percent of the gross heat transfer occurring via convection to the inner coil. The remaining 60 percent of the heat transferred is to the outer and intermediate coils through convection.

An observation as to the internal physical operation of the process heater can be accomplished using the data reported in Sections 5.2 and 5.3 in conjunction with two cases that exist in the collected data: (a) the fuel pressure is higher than the atomizing air pressure; and (b) the fuel pressure is lower than the atomizing air pressure. With all else remaining equal and the fuel pressure remaining constant, the heat transferred to the outer coil, courtesy of the measured temperatures, decreases between the first and second case. Conversely, the heat transfer to the process fluid in the inner coil increases between the two cases. This leads to the observation that an increase in heat transfer to the inner coil correlates with an increase in efficiency. As the majority of heat transferred to the inner coil is radiative, this most likely represents an increase in the radiative properties of the flame and combustion gases (*i.e.,* a more intense and/or luminous flame). Without additional sensor packages (*e.g.,* an infrared indirect temperature sensor) or further testing, it cannot be known absolutely whether the increase in thermodynamic efficiency is through an increase in radiative heat transfer, convective heat transfer, or both.

The genetic algorithm seemingly encouraged the 'shift' in heat transfer to the inner coil by adjusting the atomizing air and fuel pressures. Further alteration of testing conditions and apparatus, outlined is Section 6.2, may support and more accurately define this conclusion.

5.5 Closure

Two separate experiments were performed to test different implementations of the algorithm. The first test involved an offline implementation of the algorithm with a very limited data set collected from the process heater. The non-physical predicted efficiencies from this test, led to improvements to the second offline-online experiment. While some issues did occur during the completely online implementation of the algorithm, the second experiment, it was observed that the algorithm produces results consistent with experiential observations during the timeline of this work. Several conclusions and recommendations from the outcome of these experiments are covered in the Chapter 6.

Chapter 6

Conclusions & Recommendations

In this thesis, an adaptive and predictive optimal control methodology is developed and tested on a diesel-fueled oilfield process heater. The development portion of this body of work is divided into two key parts: development of an algorithm to predict and optimize the operating efficiency of the heater; and physical implementation of the sensors, actuators, and computing equipment needed to implement the algorithm. The algorithm developed is comprised of three iterative components: (a) an artificial neural network for adaptivity and prediction; (b) a genetic algorithm for optimization of the operating states participating with the artificial neural network; and (c) a refinement of the operating state search space to complement the other two components. This research is an important advancement on the state-of-the-art in industrial combustion control, since this marks the first attempt to implement an artificial neural network and genetic algorithm prediction/control strategy on liquid-fueled process heaters of this scale. Several challenges during the implementation on the experimental apparatus were also uncovered, namely the selection of the diesel fuel flow rate sensor and actuator used to modulate the combustion air damper position.

Two experiments to test the performance of the algorithm were carried out. The first experiment was a wholly offline test that initially evaluated the optimization of the algorithm and synergy between the three components through one iteration of the algorithm. The second experiment, recovering from difficulties in the implementation on the PLC hardware, incorporated an online component and completed three full iterations of the algorithm including refinement operations. The algorithm and the iterative methodology were consistent with

empirical observations made throughout the duration of this study on the operating process heater.

Additional analysis was performed to better understand the operating physics of the heater during the optimization. It was discovered that there is a correlation between the optimal operating state and increases to the quantity of heat transferred to the process fluid flowing through the inner coil. While radiation is the predominant mode of heat transfer to the inner coil, it is not understood, given the current sensor package, if this shift is an increase in the gross heat transfer to the inner coil or an increase in just radiative heat transfer within the inner coil. Additional testing with a different sensor selection is needed to better elucidate this observation.

6.1 Recommendations

The difficulties with implementing both the physical apparatus and the algorithm is well documented throughout this work. Given that the experimental apparatus and algorithm were intended to be released to customers on production process heaters, several recommendations are warranted. To refine the conclusions and continue with the research performed, recommendations and future work are separated into two categories: (1) further testing and; (2) alterations to experimental the apparatus and algorithm.

6.1.1 Further testing

Given the current form of the algorithm, a wider range and more extensive testing period is both necessary and recommended before this algorithm can be released to customers. Due to a limited experimentation time frame, and the length of time required to collect a single operating state, it is necessary to collect more data points to train the ANN. As was mentioned in Chapter 5, the twenty initial data points, used to train the artificial neural network, is quite small relative to what is

typical for ANNs of similar complexity. Further data points will allow the hyper-surface, fit to this data by the artificial neural network, to be more accurately predictive of the process heater operation. This is especially critical as the optimized thermodynamic efficiency is maximized with the target exhaust composition input parameter at the lower global constraint. Further data collection about this optimized input parameter may allow a better prediction of the process heater operation.

All testing was done at the same altitude and at similar ambient temperatures and humidity ranges. The fuel, while most likely not the exact same mixture, is also assumed to be from the same 'batch' and supplier. These two variables (environmental factors and diesel fuel blend), are expected to have an impact upon the results. The algorithm is designed to compensate for these factors and to optimize the operating state of the heater in spite of changes to these condition, but this capability has not been tested and completely proven. Testing under drastically different environmental conditions, especially at higher and lower ambient air temperatures, is recommended.

To further test at drastically different input conditions for the process heater, it was planned (but not undertaken) during the duration of this work, to test the algorithm with Jet A or similar blend of fuel in place of diesel fuel. While the Jet A fuel is not used by customers or in industry for process heating, it was suggested that testing on an entirely different blend of fuel than what the process heater was designed for may carry merit to test the adaptive capabilities of the algorithm. This testing should still be performed and data collected to observe the response of the process heater and algorithm to this new fuel. Specifically, observing the predicted operating efficiencies with similar input operating states. Testing could be performed entirely on the alternate fuel or by beginning with 'pure' diesel fuel and progressively blending additional quantities of Jet A fuel with the diesel over a long testing period.

Further testing is also needed to refine the global constraints on the algorithm. The algorithm operation ignores decreases in the life cycle of components within the process heater and the global constraints were determined from 'typical' input operating parameters for this process heater. As this study highlighted that the optimized thermal efficiency is at a non-typical input operating state, the long-term effects of this on the process heater is unknown.

Finally, this thesis dealt solely with a GenTex 70M TEXHEATER. The experimental apparatus and algorithm can be applied to other process heaters made by GenTex, each of which have different designs and operating physics. The capabilities of the algorithm can be further explored on these different heaters.

6.1.2 Alterations to methodology

The difficulties of implementing the algorithm on the *ifm electronic* PLC were expounded in Section 5.3. While this hardware is necessary for the safety controls of the heater, it is recommended that an additional controller/computer be added to the system to manage the operation of the algorithm. The existing PLC and HMI would remain to control sensor and actuator input and outputs and safety related operations; this would also continue with the modularity and upgradeability of customer systems for the algorithm and related hardware. Within this study, the new additional hardware would replace the offline computer component in the testing and allow a full online operation. Communication between the *ifm* CR0232 PLC and the additional computer hardware is necessary, but is a minor concern as the PLC is CANopen, a CAN bus specification for automation and embedded systems, compliant. Initially, before the use of *ifm electronic* hardware was finalized, the National Instrument CompactDAQ system, specifically cDAQ-9132 or similar, was considered in place of a PLC. With the option to expand with different input-output modules, this hardware may still be feasible as the additional/alternative computing hardware in this use.

Alternative algorithms for modeling the process heater and carrying out the optimization could also be explored. The artificial neural network is known to be computationally complex and resource heavy during training of the network. Increasing the number of inputs and outputs, the data set size, and/or the number of free parameters all contribute to increasing the computational difficulty. A possibility considered late in this study is the direct replacement of the ANN with a reduced-order proper orthogonal decomposition (POD) model. The use and development of a POD models has been covered in various other research areas with work by Chen *et al.* [68], Radermacher *et al.* [69], and Wang *et al.* [70]. Ideally, the use of a reduced-order POD model would optimize the capturing of the trend of the responses of the process heater to the varied input operating states at the sacrifice of absolute predictive accuracy. The computational workload of solving the model should decrease and the computational efficiency of the whole algorithm should increase.

Currently, the genetic algorithm only optimizes the thermodynamic efficiency of the process heater. Implementing, the originally planned multi-objective optimization, including pollutant minimization and/or thermal output, is a possibility for future work.

Lastly, improving the control of the combustion air damper position and exhaust gas oxygen content control is necessary. As has been mentioned several times earlier in the work, the time delay between changes in the sensed oxygen content of the exhaust gas and changes made to the combustion air damper position causes a stable but oscillatory control application to the actuator of the damper. The optimized exhaust gas composition is at the lower constraint value which cannot be further lowered due to this oscillatory response. Improving the damper angular position control loop, or using an entirely different control method, may lead to even greater efficiencies by lowering the lower global constraint value on the exhaust gas composition parameter.

References

[1] V. Havlena and J. Findejs, "Application of model predictive control to advanced combustion control," *Control Eng. Pract.*, vol. 13, no. 6, pp. 671–680, Jun. 2005.

[2] D. St. John and G. S. Samuelsen, "Active, optimal control of a model industrial, natural gas-fired burner," *Symp. Int. Combust.*, vol. 25, no. 1, pp. 307–316, 1994.

[3] O. Delabroy, E. Haile, F. Lacas, S. Candel, A. Pollard, A. Sobiesiak, and H. A. Becker, "Passive and active control of NOx in industrial burners," *Exp. Therm. Fluid Sci.*, vol. 16, no. 1–2, pp. 64–75, Jan. 1998.

[4] S. Candel, "Combustion dynamics and control: Progress and challenges," *Proc. Combust. Inst.*, vol. 29, no. 1, pp. 1–28, 2002.

[5] A. D. Risi, T. Donateo, and D. Laforgia, "Optimization of the Combustion Chamber of Direct Injection Diesel Engines," SAE International, Warrendale, PA, SAE Technical Paper 2003-01-1064, Mar. 2003.

[6] E. Haile, F. Lacas, and S. Candel, "Active combustion control through pulsed fuel injection," *Comptes Rendus Acad. Sci. Ser. IIB Mech. Phys. Chem. Astron.*, vol. 325, no. 4, pp. 203–209, 1997.

[7] C. Hantschk, J. Hermann, and D. Vortmeyer, "Active instability control with direct-drive servo valves in liquid-fueled combustion systems," *Twenty-Sixth Symp. Combust.*, vol. 26, no. 2, pp. 2835–2841, 1996.

[8] O. Bolland and P. Mathieu, "Comparison of two CO2 removal options in combined cycle power plants," *Energy Convers. Manag.*, vol. 39, no. 16, pp. 1653–1663, 1998.

[9] A. R. Dinicolantonio, "Flue gas recirculation for NOx reduction in premix burners," US5092761 A, 03-Mar-1992.

[10] E. Haile, O. Delabroy, D. Durox, F. Lacas, and S. Candel, "Combustion Enhancement by Active Control," in *Flow Control*, M. Gad-el-Hak and A. Pollard, Eds. Springer Berlin Heidelberg, 1998, pp. 467–499.

[11] N. Docquier and S. Candel, "Combustion control and sensors: a review," *Prog. Energy Combust. Sci.*, vol. 28, no. 2, pp. 107–150, 2002.

[12] R. C. Dorf, *Modern control systems*, 8th ed. Menlo Park, Calif; Harlow, England: Addison-Wesley, 1998.

[13] S. B. Londerville and C. E. Baukal, *The Coen & Hamworthy combustion handbook : fundamentals for power, marine & industrial applications*. Boca Raton: CRC Press, 2013.

[14] G. M. Shaver, J. C. Gerdes, and M. Roelle, "Physics-based closed-loop control of phasing, peak pressure and work output in HCCI engines utilizing variable valve actuation," in *American Control Conference, 2004. Proceedings of the 2004*, 2004, vol. 1, pp. 150–155.

[15] A. Widd, "Physics-Based Model Predictive Control of HCCI Combustion Phasing Using Fast Thermal Management and VVA," *IEEE Trans. Control Syst. Technol.*, vol. 20, no. 3, pp. 688–699, May 2012.

[16] G. M. Shaver, J. C. Gerdes, and M. J. Roelle, "Physics-based modeling and control of residual-affected HCCI engines," *J. Dyn. Syst. Meas. Control*, vol. 131, no. 2, 2009.

[17] K. R. McManus, T. Poinsot, and S. M. Candel, "A review of active control of combustion instabilities," *Prog. Energy Combust. Sci.*, vol. 19, no. 1, pp. 1–29, 1993.

[18] J. M. Cohen, N. M. Rey, C. A. Jacobson, and T. J. Anderson, "Active Control of Combustion Instability in a Liquid-Fueled Low-NOx Combustor," *J. Eng. Gas Turbines Power*, vol. 121, no. 2, pp. 281–284, Apr. 1999.

[19] T. N. Demayo, V. G. McDonell, and G. S. Samuelsen, "Robust active control of combustion stability and emissions performance in a fuel-staged natural-gas-fired industrial burner," *Proc. Combust. Inst.*, vol. 29, no. 1, pp. 131–138, 2002.

[20] A. Banaszuk, K. B. Ariyur, M. Krstić, and C. A. Jacobson, "An adaptive algorithm for control of combustion instability," *Automatica*, vol. 40, no. 11, pp. 1965–1972, 2004.

[21] A. Banaszuk, Y. Zhang, and C. A. Jacobson, "Adaptive control of combustion instability using extremum-seeking," in *American Control Conference, 2000. Proceedings of the 2000*, 2000, vol. 1, pp. 416–422.

[22] J. Brouwer, B. A. Ault, J. E. Bobrow, and G. S. Samuelsen, "Active control for gas turbine combustors," in *International Symposium on Combustion*, 1991, vol. 23, pp. 1087–1092.

[23] C. O. Paschereit, B. Schuermans, and D. Buche, "Combustion process optimization using evolutionary algorithm," in *ASME Turbo Expo 2003, collocated with the 2003 International Joint Power Generation Conference*, 2003, pp. 281–291.

[24] R. Blonbou, A. Laverdant, S. Zaleski, and P. Kuentzmann, "Active control of combustion instabilities on a rijke tube using neural networks," *Proc. Combust. Inst.*, vol. 28, no. 1, pp. 747–755, 2000.

[25] A. Steinboeck, D. Wild, T. Kiefer, and A. Kugi, "A mathematical model of a slab reheating furnace with radiative heat transfer and non-participating gaseous media," *Int. J. Heat Mass Transf.*, vol. 53, no. 25–26, pp. 5933–5946, Dec. 2010.

[26] K. Chenoweth, A. C. T. van Duin, S. Dasgupta, and W. A. Goddard III, "Initiation Mechanisms and Kinetics of Pyrolysis and Combustion of JP-10 Hydrocarbon Jet Fuel," *J. Phys. Chem. A*, vol. 113, no. 9, pp. 1740–1746, 2009.

[27] P. A. Ioannou and B. Fidan, *Adaptive control tutorial*. Philadelphia, PA: Society for Industrial and Applied Mathematics, 2006.

[28] K. J. Daun, S. Hajitaheri, and J. L. Wright, "Numerical Simulation of the GenTex 50M TexHeater," University of Waterloo, Canada, Internal Report, 2011.

[29] S. Hajitaheri, "Design Optimization and Combustion Simulation of Two Gaseous and Liquid-Fired Combustors," M.A.Sc., University of Waterloo, Canada, 2012.

[30] M. Nikolaou, "Model predictive controllers: A critical synthesis of theory and industrial needs," *Adv. Chem. Eng.*, vol. 26, pp. 131–204, 2001.

[31] S. S. Haykin, *Neural networks : a comprehensive foundation*, 2nd ed. Upper Saddle River, NJ: Prentice Hall, 1999.

[32] J.-Z. Chu, S.-S. Shieh, S.-S. Jang, C.-I. Chien, H.-P. Wan, and H.-H. Ko, "Constrained optimization of combustion in a simulated coal-fired boiler using artificial neural network model and information analysis," *Fuel*, vol. 82, no. 6, pp. 693–703, Apr. 2003.

[33] M. G. Allen, C. T. Butler, S. A. Johnson, E. Y. Lo, and F. Russo, "An imaging neural network combustion control system for utility boiler applications," *Combust. Flame*, vol. 94, no. 1, pp. 205–214, 1993.

[34] M. Benammar, "Techniques for measurement of oxygen and air-to-fuel ratio using zirconia sensors. A review," *Meas. Sci. Technol.*, vol. 5, no. 7, p. 757, Jul. 1994.

[35] E. Ivers-Tiffée, K. H. Härdtl, W. Menesklou, and J. Riegel, "Principles of solid state oxygen sensors for lean combustion gas control," *Electrochimica Acta*, vol. 47, no. 5, pp. 807–814, Dec. 2001.

[36] L. C. de Lima, H. A. Carmona, C. V. M. da Silva, and F. S. Cavalcante Junior, "Oxygen Excess Control of Industrial Combustion Through the Use of Automotive Lambda Sensor," *Int. Trans. J. Eng. Manag. Appl. Sci. Technol.*, vol. 3, no. 2, pp. 365–373, 2011.

[37] K. Benson, J. D. Thornton, D. L. Straub, E. D. Huckaby, and G. A. Richards, "Flame Ionization Sensor Integrated Into a Gas Turbine Fuel Nozzle," *J. Eng. Gas Turbines Power*, vol. 127, no. 1, pp. 42–48, Feb. 2005.

[38] D. Buche, P. Stoll, R. Dornberger, and P. Koumoutsakos, "Multiobjective evolutionary algorithm for the optimization of noisy combustion processes," *Syst. Man Cybern. Part C Appl. Rev. IEEE Trans. On*, vol. 32, no. 4, pp. 460–473, 2002.

[39] D. Büche, P. Stoll, and P. Koumoutsakos, "An evolutionary algorithm for multi-objective optimization of combustion processes," *Cent. Turbul. Res. Annu. Res. Briefs*, vol. 2001, pp. 231–239, 2001.

[40] K. H. Yu, "Active control of engine dynamics: fundamentals and fluid dynamics," in *Proceedings of the VKI Special Course Active control of engine dynamics*, Rhode Saint Genese, Belgium, 2001.

[41] J. Hermann, S. Gleis, and D. Vortmeyer, "Active Instability Control (AIC) of Spray Combustors by Modulation of the Liquid Fuel Flow Rate," *Combust. Sci. Technol.*, vol. 118, no. 1–3, pp. 1–25, Sep. 1996.

[42] W. M. Budzianowski and R. Miller, "Towards Improvements in Thermal Efficiency and Reduced Harmful Emissions of Combustion Processes by Using Recirculation of Heat and Mass: A Review," *Recent Pat. Mech. Eng.*, vol. 2, no. 3, pp. 228–239, Nov. 2009.

[43] J. Baltasar, "Flue gas recirculation in a gas-fired laboratory furnace: measurements and modelling," *Fuel*, vol. 76, no. 10, pp. 919–929.

[44] S. C. Wood, "Select the Right NOX Control Technology," *Chem. Eng. Prog.*, vol. 90, no. 1, pp. 32–38, 1994.

[45] K. T. Padmanabhan, C. T. Bowman, and J. D. Powell, "An adaptive optimal combustion control strategy," *Combust. Flame*, vol. 100, no. 1–2, pp. 101–110, Jan. 1995.

[46] "Diesel fuel characteristics and resources." [Online]. Available: http://www.ufa.com/petroleum/resources/fuel/diesel_fuel_resources.html. [Accessed: 03-Jan-2015].

[47] W. Yuan, A. Hansen, Q. Zhang, and Z. Tan, "Temperature-dependent kinematic viscosity of selected biodiesel fuels and blends with diesel fuel," *J. Am. Oil Chem. Soc.*, vol. 82, no. 3, pp. 195–199, 2005.

[48] "Accurate Presentation of Turbine Flow Meter Calibration Data," Cox Instruments, LLC, White Paper.

[49] J. Frederick, "Single Fluid Universal Viscosity Curve: A Concept Not Always Used or Understood By Calibration Laboratories," Flow Dynamics Inc., White Paper.

[50] "Turbine Flowmeter Fuel Flow Calculation," SAE International, SAE Aerospace Recommended Practice ARP4990, 1997.

[51] A. Trigas, "Practical Aspects of Turbine Flow Meters Calibration and UVC Principles," TrigasFI GmbH, White Paper, 2008.

[52] L. M. Sonneborn and F. S. van Vleck, "The Bang-Bang Principle for Linear Control Systems," *J. Soc. Ind. Appl.*, vol. Mathematics, p. SeriesA:Control2,151, 1964.

[53] T. Le, "Actuation + Sensors," 28-Mar-2014.

[54] R. Blonbou, A. Laverdant, S. Zaleski, and P. Kuentzmann, "Active Adaptive Combustion Control Using Neural Networks," *Combust. Sci. Technol.*, vol. 156, no. 1, pp. 25–47, 2000.

[55] M. T. Hagan, *Neural network design*. Boston: PWS Pub, 1996.

[56] S. A. Kalogirou, "Artificial intelligence for the modeling and control of combustion processes: a review," *Prog. Energy Combust. Sci.*, vol. 29, no. 6, pp. 515–566, 2003.

[57] *NeuroShell 2 Manual*. Ward Systems Group Inc., 2008.

[58] D. J. C. MacKay, "A Practical Bayesian Framework for Backpropagation Networks," *Neural Comput.*, vol. 4, no. 3, pp. 448–472, May 1992.

[59] J. Poland, "On the Robustness of Update Strategies for the Bayesian Hyperparameter α." 2001.

[60] D. E. Goldberg, *Genetic algorithms in search, optimization, and machine learning*. Reading, Mass; Don Mills, Ont: Addison-Wesley PubCo, 1989.

[61] K. Deb, *Multi-objective optimization using evolutionary algorithms*, 1st ed. Chichester, England ; New York: John Wiley & Sons, 2001.

[62] A. Horsman, "Design Optimization of a Porous Radiant Burner," M.A.Sc., University of Waterloo, Waterloo, Ontario, 2010.

[63] E. Canada, "Historical Climate Data - Environment Canada," 15-Mar-2015. [Online]. Available: http://climate.weather.gc.ca/climateData/dailydata_e.html?StationID=51440&Month=3&Day=13&Year=2015&timeframe=2. [Accessed: 15-Mar-2015].

[64] *MATLAB 2014b*. Natick, Massachusetts: The MathWorks, Inc., 2015.

[65] M. Renksizbulut, "ME 557 Combustion Lecture Notes - Winter 2012." University of Waterloo, 2012.

[66] M. Matalon, "Lecture 13: Droplet Combustion and Spray Modeling," Princeton CEFRC, 2011.

[67] K. J. Daun, "Heat Transfer Analysis of the GenTex 70M Process Heater," Dec. 2009.

[68] X. Chen and A. Kareem, "Proper orthogonal decomposition-based modeling, analysis, and simulation of dynamic wind load effects on structures.(Author Abstract)," *J. Eng. Mech.*, vol. 131, no. 4, p. 325, 2005.

[69] A. Radermacher, S. Reese, and A. M. D. H. Hadoush, "Selective proper orthogonal decomposition model reduction for forming simulations," *PAMM*, vol. 13, no. 1, pp. 115–116, 2013.

[70] Q. Wang, Z. X. Wang, J. J. Song, Y. Xu, and J. Z. Xu, "Study on a new aerodynamic model of HAWT based on panel method and Reduced Order Model using Proper Orthogonal Decomposition," *Renew. Energy*, vol. 48, pp. 436–447, 2012.

Appendix A

ecomat100
Control systems

ifm electronic

CR0232

Mobile controller
ExtendedController

32-bit processor

32 inputs
48 outputs

4 CAN interfaces

CODESYS 2.3

10...32 V DC

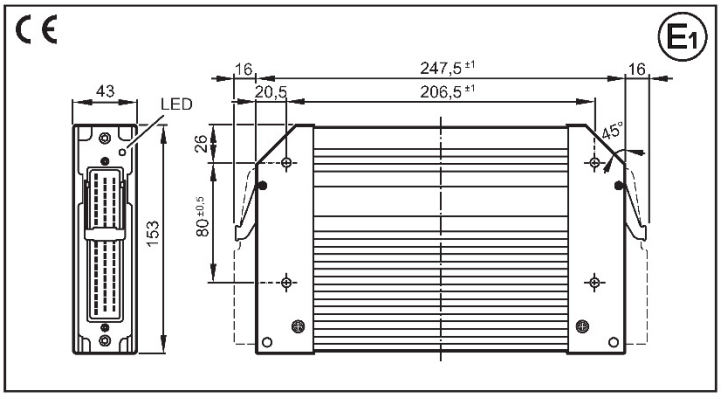

Technical data	Controller as black-box system to implement a central or decentralised system design
Mechanical data	
Housing	Closed, screened metal housing with flange fastening
Dimensions (H x W x D)	153 x 247.5 x 43 mm
Installation	Screw connection by means of 4 M5 x L screws to ISO 7380, DIN 7984 or DIN 7500 Mounting position horizontal or vertical to the mounting wall
Connection	2 55-pin connectors, latched, protected against reverse polarity, type AMP or Framatome AMP junior timer contacts, crimp connection 0.5/2.5 mm²
Weight	1.6 kg
Housing/storage temperature	– 40...85 °C (depending on the load) / – 40...85 °C
Protection rating	IP 67 (for inserted connector with individually sealed cores, e.g. EC2084)
Electrical data	
Input/output channels (total)	80 (32 inputs / 48 outputs)
Inputs	Configurable Digital for positive/negative sensor signals, positive with diagnostic capabilities Analogue (0...10 / 32 V, 0...20 mA, ratiometric) Frequency (≤ 30 kHz)
Outputs type 1	Configurable Digital positive/negative switching (high/low side) PWM output (20...250 Hz, 16 x max. 4 A, 16 x max. 2 A) Current-controlled (16 x 0.02...4 A, 16 x 0.01...2 A)
Outputs type 2	Digital, positive switching (high side, 8 x max. 2 A)
	For the number of inputs/outputs and configuration options also see the wiring diagrams
Operating voltage Overvoltage Input voltage gradient	10...32 V DC 36 V for t ≤ 10 s > 1.3 V/s
Reverse polarity protection	yes
Current consumption	≤ 320 mA (without external load at 24 V DC)
CAN interfaces 1...4 Baud rate Communication profile	CAN Interface 2.0 A/B, ISO 11898 50 Kbits/s...1 Mbit/s (default 125 Kbits/s) CANopen, CiA DS 301 V4.01, CiA DS 306 V1.3 or SAE J 1939 or free protocol
Serial interface Baud rate Topology Protocol	RS-232 C 9.6...115.2 Kbits/s (default 115.2 Kbits/s) Point-to-point (max. 2 participants); master-slave connection Predefined ifm protocol (INTELHEX)

ecomat100
Control systems

ifm electronic

CR0232	Technical data
Virtual COM port	USB, max. 1 MBaud
Processor	32-bit CPU Infineon TriCore 1796
Device monitoring	Undervoltage monitoring Watchdog function Checksum test for program and system Excess temperature monitoring
Process monitoring concept	Second switch-off mode for 8 outputs each via a relay
Physical memory	Flash: 2 Mbytes RAM: 2 Mbytes Remanent memory: 128 Kbytes
Memory allocation	See system manual www.ifm.com → Data sheet search → CR0232 → More information
Software/programming	
Programming system	CODESYS version 2.3 (IEC 61131-3)
Indicators	
Status LED	Three-colour LED (R/G/B)

Operating states

No longer valid if the colours and/or flashing modes are changed by the application program.

LED colour	Status	Description
–	off	No operating voltage or fatal error
Yellow	1 x on	Initialisation or reset checks
Orange	on	Error in the start-up phase
Green	5 Hz	No operating system loaded
	2 Hz	Run
	on	Stop
Red	2 Hz	Run with error
	on	Fatal error or stop with error

ecomat100
Control systems

ifm electronic

CR0232	Technical data	
Test standards and regulations		
CE marking	EN 61000-6-2	Electromagnetic compatibility (EMC) Noise immunity
	EN 61000-6-4	Electromagnetic compatibility (EMC) Emission standard
	EN 61010	Safety requirements for electrical equipment for measurement, control and laboratory use
E1 marking	UN/ECE-R10	Emission standard Noise immunity with 100 V/m
Electrical tests	ISO 7637-2	Pulse 1, severity level: IV; function state C Pulse 2a, severity level: IV; function state A Pulse 2b, severity level: IV; function state C Pulse 3a, severity level: IV; function state A Pulse 3b, severity level: IV; function state A Pulse 4, severity level: IV; function state A Pulse 5, severity level: III; function state C (data valid for the 24V system) Pulse 4, severity level: III; function state C (data valid for the 12 V system)
Climatic tests	EN 60068-2-30	Damp heat, cyclic upper temperature 55°C, number of cycles: 6
	EN 60068-2-78	Damp heat, steady state Test temperature 40°C / 93% RH, Test duration: 21 days
	EN 60068-2-52	Salt spray test Severity level 3 (vehicle)
Mechanical tests	ISO 16750-3	Test VII; vibration, random Mounting location: vehicle body
	EN 60068-2-6	Vibration, sinusoidal 10...500 Hz; 0.72 mm/10 g; 10 cycles/axis
	ISO 16750-3	Bumps 30 g/6 ms; 24,000 shocks

ecomat100
Control systems

ifm electronic

CR0232	St side / input characteristics	
I00...15 **Multifunction inputs with supply voltage independent levels for frequency measurement**	Resolution	12 bits
	Accuracy	± 1 % FS (in the measuring range 0...20 mA: ± 2 % FS)
	Measuring ranges	0...10 V, 0...32 V, 0...20 mA, ratiometric
Current input 0...20 mA (A)	Input resistance	390 Ω
	Input frequency	≤ 1 kHz (default 35 Hz)
Voltage input 0...10 V (A)	Input resistance	65.6 kΩ
	Input frequency	≤ 1 kHz (default 35 Hz)
Voltage input 0...32 V (A)	Input resistance	50.7 kΩ
	Input frequency	≤ 1 kHz (default 35 Hz)
Voltage input ratiometric (A)	Input resistance	50.7 kΩ
	Input frequency	≤ 1 kHz (default 35 Hz)
Frequency input (FRQ)	Input resistance	3.2 kΩ
	Input frequency	≤ 30 kHz
	Switch-on level	> 0.35...0.55 U_B
	Switch-off level	< 0.29 U_B
Digital input ($B_{L/H}$)	Input resistance	3.2 kΩ
	Input frequency	≤ 1 kHz (default 35 Hz)
	Switch-on level	> 0.7 U_B
	Switch-off level	< 0.3 U_B
	Diagnostics* Short circuit to VBB	> 0.95 U_B
	Diagnostics* Short circuit to GND / wire break	< 1 V
	*) only binary low-side (B_L)	
Note		
Test input (pin 50)	During the test mode (e.g. programming) the connector pin must be connected to VBB_S (10...32 V DC). For the "RUN" mode, connect the test input to GND.	
	Observe the notes on the configuration of the inputs/outputs! (system manual "ExtendedController CR0232")	
Abbreviations	A Analogue B_H Binary high side B_L Binary low side FRQ Frequency / pulse inputs with levels depending on the supply voltage H H-bridge function PWM Pulse width modulation VBB_O Supply outputs VBB_S Supply sensors/module VBB_R Supply via relay	

ecomat100
Control systems

ifm electronic

CR0232	St side / output characteristics	
Q00...03 Q08...11 Digital/PWM outputs (type 1)	Protective circuit for inductive loads	Integrated
	Diagnosis wire break	via current feedback
	Diagnosis short circuit	via current feedback
Digital output (B_H and B_{HL})	Switching voltage	10...32 V DC
	Switching current	0.01...2 A / 0.02...4 A (of which 4 with H-bridge function)
PWM output (PWM)	Output frequency	20...250 Hz (per channel)
	Pulse/pause ratio	1...1000 ‰ (adjustable via software)
	Resolution	1 ‰
	Switching current	0.01...2 A / 0.02...4 A (of which 4 with H-bridge function)
Current-controlled output (PWM_I)	Output frequency	20...250 Hz (per channel)
	Control range	0.01...2 A / 0.02...4 A
	Setting resolution	1 mA
	Control resolution	1 mA / 2 mA
	Load resistance	≥ 6 Ω / ≥ 3 Ω (at 12 V DC) ≥ 12 Ω / ≥ 6 Ω (at 24 V DC)
	Accuracy	± 2 % FS (for inductive loads)
Q04...07 Q12...15 Digital/PWM outputs (type 1)	Protective circuit for inductive loads	Integrated
	Diagnosis wire break	via current feedback
	Diagnosis short circuit	via current feedback
Digital output (B_H)	Switching voltage	10...32 V DC
	Switching current	0.01...2 A
PWM output (PWM)	Output frequency	20...250 Hz (per channel)
	Pulse/pause ratio	1...1000 ‰ (adjustable via software)
	Resolution	1 ‰
	Switching current	0.01...2 A
Current-controlled output (PWM_I)	Output frequency	20...250 Hz (per channel)
	Control range	0.01...2 A
	Setting resolution	1 mA
	Control resolution	1 mA
	Load resistance	≥ 3 Ω / (at 12 V DC) ≥ 6 Ω / (at 24 V DC)
	Accuracy	± 2 % FS (for inductive loads)

ecomat100
Control systems

ifm electronic

CR0232	St side / output characteristics
Reference voltage V_{REF} OUT (sensor supply)	For sensors and joysticks 5/10 V, 400 mA, accuracy ± 7 % Short-circuit proof and overload protected (10 V reference only from a supply voltage U_B ≥ 13 V)
Internal relays	NO contacts for the second switch-off way of the outputs. One relay in series of 8 semiconductor outputs each. Forced control via the hardware and additional control via the user program. The relays must always be switched without load!
Load current per output group (VBB_R, VBB_O)	≤ 12 A (for continuous operation ≤ 6 A; i.e. operation ≥ 10 min)
Overload protection (valid for all outputs)	≤ 5 minutes (at 100% overload)
Short-circuit strength to GND	Switch-off of the outputs is carried out via the output driver

Switching current	0.1...15 A
Overload current	20 A
Number of operating cycles (without load)	≥ 10^6
Switching time constant	≤ 3 ms

Abbreviations

A	Analogue
B_H	Binary high side
B_L	Binary low side
FRQ	Frequency / pulse inputs with levels depending on the supply voltage
H	H-bridge function
PWM	Pulse width modulation
VBB_O	Supply outputs
VBB_S	Supply sensors/module
VBB_R	Supply via relay

ecomat100
Control systems

ifm electronic

CR0232	Ex side / input characteristics

I00_E...15_E
Analogue / digital inputs

Resolution	12 bits
Accuracy	± 1 % FS (in the measuring range 0...20 mA: ± 2 % FS)
Measuring ranges	0...10 V, 0...32 V, 0...20 mA, ratiometric

Current input 0...20 mA (A)

Input resistance	390 Ω
Input frequency	≤ 1 kHz (default 35 Hz)

Voltage input 0...10 V (A)

Input resistance	65.6 kΩ
Input frequency	≤ 1 kHz (default 35 Hz)

Voltage input 0...32 V (A)

Input resistance	50.7 kΩ
Input frequency	≤ 1 kHz (default 35 Hz)

Voltage input ratiometric (A)

Input resistance	50.7 kΩ
Input frequency	≤ 1 kHz (default 35 Hz)

Frequency input (FRQ)
only I00_E...15_E

Input resistance	3.2 kΩ
Input frequency	≤ 30 kHz
Switch-on level	> 0.35...0.55 U_B
Switch-off level	< 0.29 U_B

Digital input ($B_{L/H}$)

Input resistance	3.2 kΩ
Input frequency	≤ 1 kHz (default 35 Hz)
Switch-on level	> 0.7 U_B
Switch-off level	< 0.3 U_B
Diagnostics* Short circuit to VBB	> 0.95 U_B
Diagnostics* Short circuit to GND / wire break	< 1 V

*) only binary low-side (B_L)

ecomat100
Control systems

ifm electronic

CR0232	Ex side / output characteristics	
Q00_E...03_E Q08_E...11_E Digital/PWM outputs (type 1)	Protective circuit for inductive loads	Integrated
	Diagnosis wire break	via current feedback
	Diagnosis short circuit	via current feedback
Digital output (B_H and B_{HL})	Switching voltage	10...32 V DC
	Switching current	0.01...2 A / 0.02...4 A (of which 4 with H-bridge function)
PWM output (PWM)	Output frequency	20...250 Hz (per channel)
	Pulse/pause ratio	1...1000 ‰ (adjustable via software)
	Resolution	1 ‰
	Switching current	0.01...2 A / 0.02...4 A (of which 4 with H-bridge function)
Current-controlled output (PWM_I)	Output frequency	20...250 Hz (per channel)
	Control range	0.01...2 A / 0.02...4 A
	Setting resolution	1 mA
	Control resolution	1 mA / 2 mA
	Load resistance	≥ 6 Ω / ≥ 3 Ω (at 12 V DC) ≥ 12 Ω / ≥ 6 Ω (at 24 V DC)
	Accuracy	± 2 % FS (for inductive loads)
Q04_E...07_E Q12_E...15_E Digital/PWM outputs (type 1)	Protective circuit for inductive loads	Integrated
	Diagnosis wire break	via current feedback
	Diagnosis short circuit	via current feedback
Digital output (B_H)	Switching voltage	10...32 V DC
	Switching current	0.01...2 A
PWM output (PWM)	Output frequency	20...250 Hz (per channel)
	Pulse/pause ratio	1...1000 ‰ (adjustable via software)
	Resolution	1 ‰
	Switching current	0.01...2 A
Current-controlled output (PWM_I)	Output frequency	20...250 Hz (per channel)
	Control range	0.01...2 A
	Setting resolution	1 mA
	Control resolution	1 mA
	Load resistance	≥ 3 Ω / (at 12 V DC) ≥ 6 Ω / (at 24 V DC)
	Accuracy	± 2 % FS (for inductive loads)

ecomat100
Control systems

ifm electronic

CR0232	Ex side / output characteristics
Q16_E...Q31_E Digital outputs (type 2)	
Digital output (B_H)	Switching voltage: 10...32 V DC Switching current: 8 x 0.01...2 A Diagnosis via voltage feedback: Wire break/short circuit
Internal relays	NO contacts for the second switch-off way of the outputs. One relay in series of 8 semiconductor outputs each. Forced control via the hardware and additional control via the user program.
	The relays must always be switched without load!
Load current per output group (VBB_1, VBB_2, VBB_3)	≤ 12 A (for continuous operation ≤ 6 A; i.e. operation ≥ 10 min)
Overload protection (valid for all outputs)	≤ 5 minutes (at 100% overload)
Short-circuit strength to GND	Switch-off of the outputs is carried out via the output driver

ecomat100
Control systems

ifm electronic

CR0232 | **Technical data**

Wiring | St side

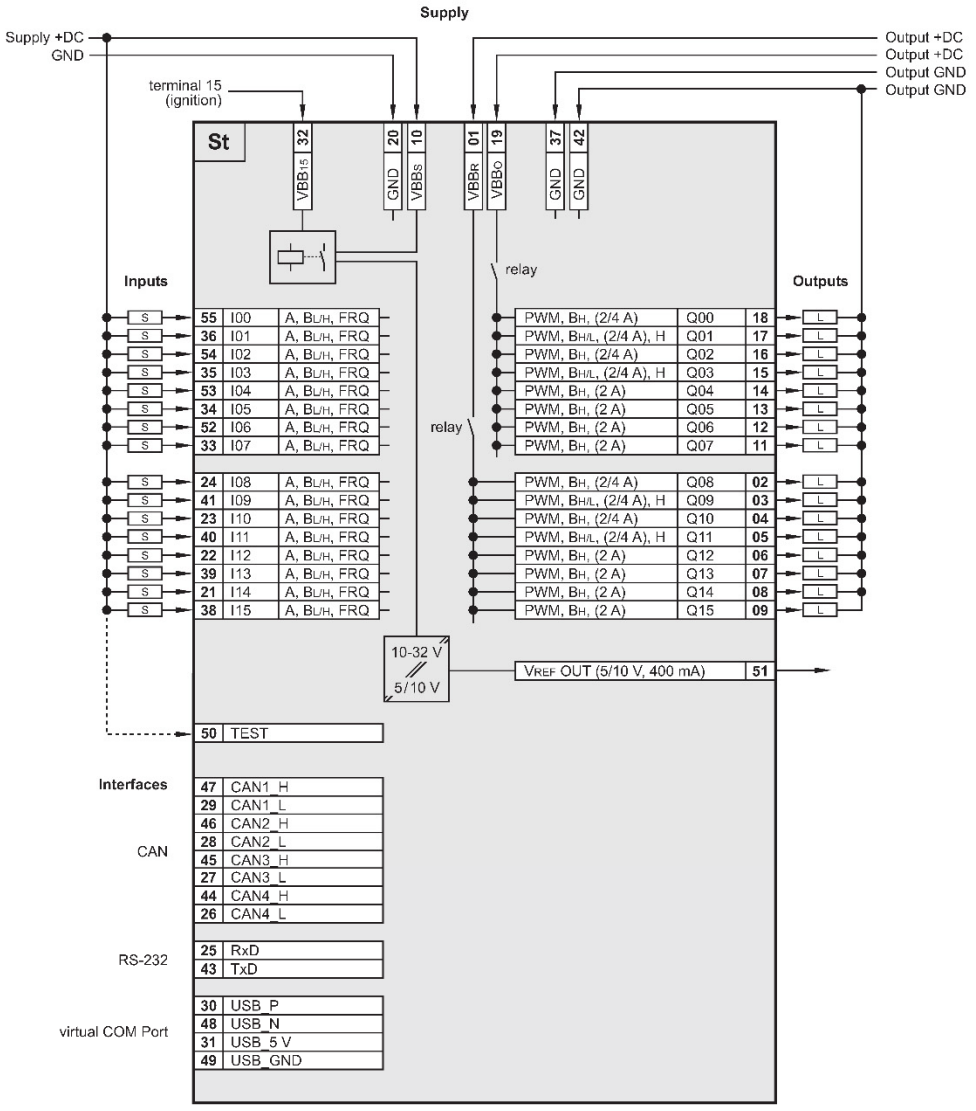

Abbreviations

A	Analogue
B_H	Binary high side
B_L	Binary low side
FRQ	Frequency / pulse inputs with levels depending on the supply voltage
H	H-bridge function
PWM	Pulse width modulation
VBB_O	Supply outputs
VBB_S	Supply sensors/module
VBB_R	Supply via relay
St	Standard side
Ex	Extended side

ecomat100
Control systems

ifm electronic

CR0232 | **Technical data**

Wiring | Ex side

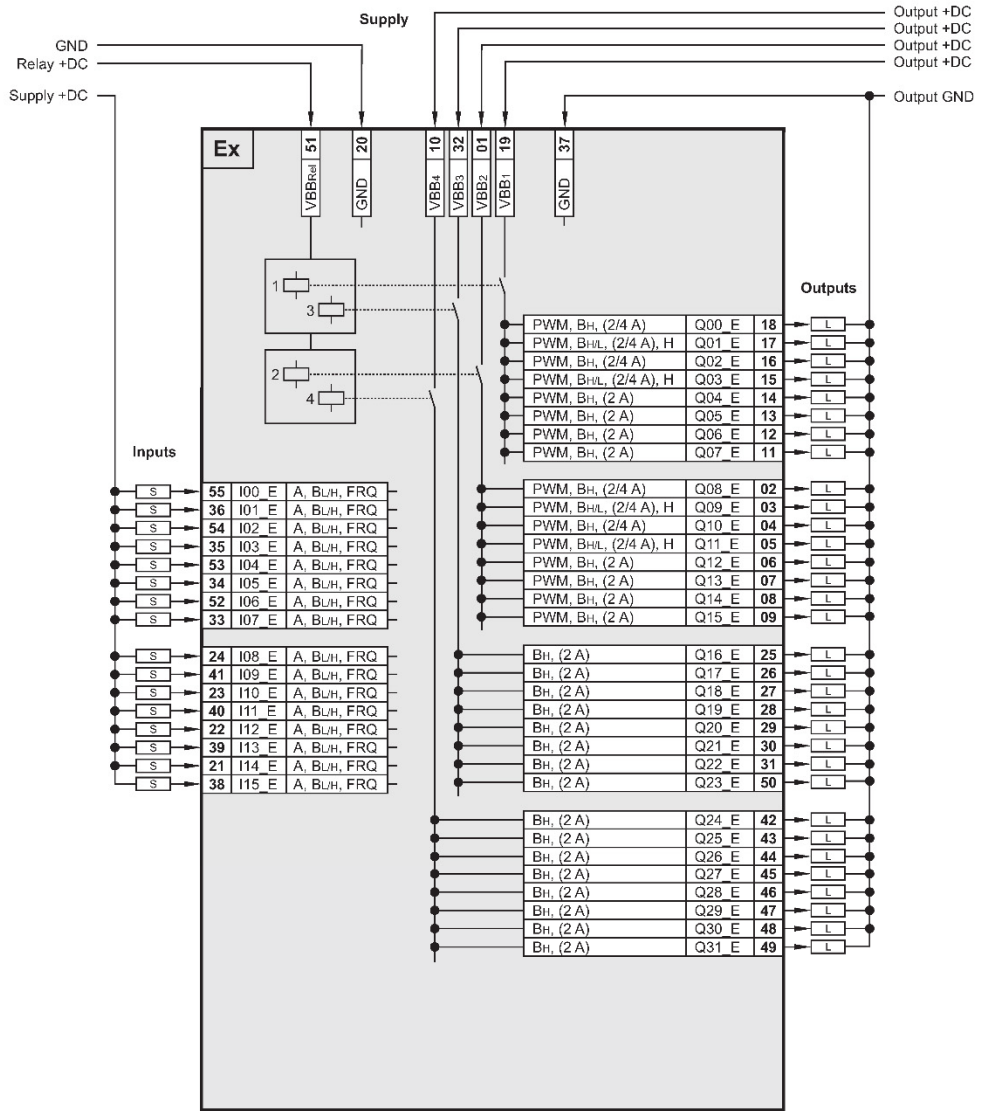

Abbreviations

A	Analogue
B_H	Binary high side
B_L	Binary low side
FRQ	Frequency / pulse inputs with levels depending on the supply voltage
H	H-bridge function
PWM	Pulse width modulation
VBB_O	Supply outputs
VBB_S	Supply sensors/module
VBB_R	Supply via relay
St	Standard side
Ex	Extended side

ecomat100
Control systems

ifm electronic

CR1081

Process and dialogue module
PDM360 NG

7" colour display

9 freely programmable
backlit
function keys

rocker switch
with pushbutton

1 input / 1 output

10...32 V DC

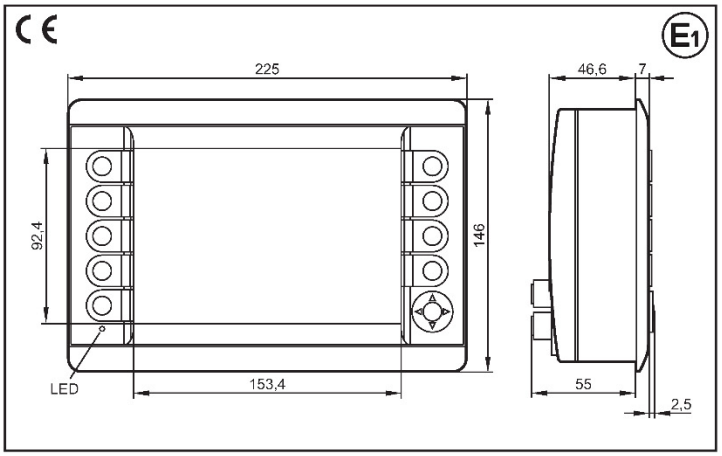

Technical data	Programmable graphic display for controlling, parameter-setting and operation of mobile machines and plants
Display	
Display	TFT LCD colour display
Format	15:9 (wide VGA), 153.4 x 92.4 mm, 7" diagonal
Resolution	800 x 480 pixels
Alignment	horizontal
Surface	glass, anti-reflective (coating) based on the principle of optical interference
Colours	262.144 (18 bits)
Background illumination	LED (lifetime ≥ 20,000 h, typically 30,000 h)
Brightness	≥ 350 cd/m², typically 400 cd/m² (adjustable 0...100%, increments 1%)
Contrast ratio	≥ 250:1, typically 400:1
Character sets	can be uploaded individually and is freely scalable preinstalled: ifm ISO fonts with vehicle-specific symbols, Arial, Courier
Mechanical data	
Mounting variants	panel mounting with mounting frame surface mounting with RAM® mount system (mounting accessories not included)
Dimensions (W x H x D)	225 x 146 x 64.5 mm
Cutout for panel mounting (W x H)	183 ± 0.5 x 136 ± 0.5 mm
Housing material	die-cast aluminium housing, powder coating (RAL 9005)
Pushbuttons	9 function keys (silicone keyboard) with tactile feedback freely programmable (softkey function) lifetime ≥ 1,000,000 activations
Rocker switch	cursor function (up, down, left, right) with tactile feedback and with central mechancial pushbutton lifetime ≥ 1,000,000 activations
Background illumination operating elements	LED (brightness adjustable 0...100%, individual control)
Protection rating	IP 67 (with mounted connectors and/or protective caps)
Operating temperature	-30...65° C
Storage temperature	-30...80° C
Weight	approx. 1.5 kg

ecomat100
Control systems

ifm electronic

CR1081	Technical data		
Electrical data			
Operating voltage	10...32 V DC		
Overvoltage detection Overvoltage shutdown Undervoltage detection Undervoltage shutdown Accuracy	at U_B > 32 V at U_B > 34 V (hysteresis 1 V, i.e. switching on again at U_B < 33 V) at U_B < 10 V at U_B < 8 V (hysteresis 1 V, i.e. switching on again at U_B > 9 V) 3 % FS		
Current consumption	300 mA (without external load at 24 V DC)		
Short-circuit / reverse polarity protection	electronic		
Processor	MPC5121, 32 bits, 400 MHz		
Total memory	256-Mbyte RAM / 128-Mbyte flash / 1-Gbyte internal mass storage		
Memory allocation	see system manual PDM360 NG www.ifm.com → Data sheet direct: → CR1081 → Additional data		
Interfaces			
CAN 1...4	CAN interface 2.0 A/B, ISO 11898 50 Kbits/s...1 Mbit/s (default 125 Kbits/s) CANopen, CiA DS 301 version 4, CiA DS 401 version 1.4 or SAE J 1939 or free protocol (Raw CAN) max. current load VBB_C ≤ 400 mA (protected by multi fuse)		
Ethernet	transmission rate 10/100 Mbits/s		
USB	2 x USB 2.0 full speed, transmission rate up to 12 Mbit/s USB master operation (service and maintenance connection for keyboard, mouse etc.) output current per interface ≤ 500 mA		
Analogue video input	–		
Input	configurable digital for positive / negative sensor signals analogue 0...10, 0...32 V, 0...20 mA, ratiometric		
Output	digital, positive switching (high side) supply via terminal 30		
Characteristics of the input		Resolution	8 bits
		Accuracy	± 3 % FS
Current input 0...20 mA		Input resistance	390 Ω
		Input frequency	10 Hz
Voltage input 0...10 V		Input resistance	65.6 kΩ
		Input frequency	10 Hz
Voltage input 0...32 V		Input resistance	50.7 kΩ
		Input frequency	10 Hz
Voltage input ratiometric		Input resistance	50.7 kΩ
		Input frequency	10 Hz
Digital input		Input resistance	3.2 kΩ
		Input frequency	10 Hz
		Switch-on level	> 0.7 U_B
		Switch-off level	< 0.3 U_B
Characteristics of the output		Switching voltage	10...32 V DC
		Switching current	≤ 1 A
		Free-wheeling diodes	integrated
Software/programming			
Operating system	Embedded Linux 2.6		
Programming system	CoDeSys version 2.3 (IEC 61131-3)		
Graphic functions	via integrated target visualisation		

ecomat100
Control systems

ifm electronic

CR1081	Technical data		
Other features			
Acoustic signal output	integrated buzzer tone duration and pitch programmable		
Temperature monitoring	2 integrated sensors for measuring the temperature inside the housing		
Brightness adaptation	light sensor in the front of the device to adapt the brightness of the display and the operating elements		
Clock / Battery	real-time clock (RTC), battery buffered / CR2032 (3 V, 230 mAh)		
Status LED	RGB LED, colours and states programmable by means of the application software		
Operating states (preset)	**Colour** / **Status** / **Description** – / permanently off / no operating voltage green / 5 Hz / boot process application green / 2 Hz / application running (RUN) or set-up running green / permanently on / application has stopped (STOP) or no project available red / 2 Hz / application is running with an error (RUN with error) red / permanently on / system error (fatal error), device is in reset (e.g. internal voltage error) red/orange / 2 Hz colour change / overtemperature/undertemperature, device is in reset until temperature in normal range orange / 5 Hz / boot process system recovery/update orange / 2 Hz / system recovery/update running orange / briefly on / System reset		
Test standards and regulations			
CE marking		EN 61000-6-2: 2005	Electromagnetic compatibility (EMC) Noise immunity
		EN 61000-6-4: 2007	Electromagnetic compatibility (EMC) Emission standard
		EN 61010-1: 2001	Safety requirements for electrical equipment for measurement, control and laboratory use
E1 marking		UN/ECE-R10	Emissions Noise immunity with 100 V/m
Electrical tests		ISO 7637-2: 2004	Pulse 1, severity level: IV; function state C Pulse 2a, severity level: IV; function state A Pulse 2b, severity level: IV; function state C Pulse 3a, severity level: IV; function state A Pulse 3b, severity level: IV; function state A Pulse 4, severity level: IV; function state A Pulse 5, severity level: III; function state C data valid for the 24V system
Climatic tests		EN 60068-2-30: 2006	Damp heat, cyclic upper temperature 55°C, number of cycles: 6
		EN 60068-2-78: 2002	Damp heat, constant test temperature 40°C / 93% RH, test duration: 21 days
		EN 60068-2-52: 1996	Salt spray test severity level 3 (motor vehicle)
Mechanical tests		ISO 16750-3: 2007	Test VII; Vibration, random mounting location: vehicle body
		EN 60068-2-6: 2008	Vibration, sinusoidal 10...500 Hz; 0.72 mm/10 g; 10 cycles/axis
		ISO 16750-3: 2007	Bumps 30 r/6 ms; 24,000 shocks

ecomat100
Control systems

ifm electronic

CR1081	Technical data

Back of the unit

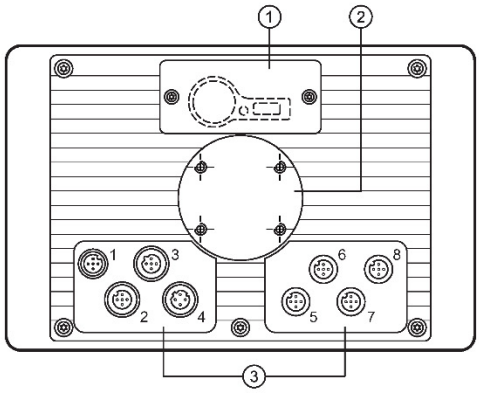

1: Service cover for USB connection, battery and watchdog reset
2: Locator for RAM® mount system and mounting frame
3: M12 connector (fig. shows max. number of connectors)

M12 connector

1	2, 5, 6, 7, 8	3	4
Connector A-coded, 5 poles	Socket A-coded, 5 poles	Socket B-coded, 5 poles	Socket D-coded, 4 poles
			

Wiring

(1) Supply, input/output	
1	10...32 V DC (clamp 30) (IN)
2	IN
3	GND (clamp 31) (IN)
4	OUT
5	10...32 V DC (clamp 15) (IN)

(2) CAN1	
1	Shield
2	VBB_c (OUT)
3	CAN1_GND (OUT)
4	CAN1_H
5	CAN1_L

(3) USB	
1	+5 V DC
2	-Data
3	+Data
4	ID
5	GND

(4) Ethernet	
1	TxD+
2	RxD+
3	TxD-
4	RxD-
	Housing = screen

(5) CAN2	
1	Shield
2	VBB_c (OUT)
3	CAN2_GND (OUT)
4	CAN2_H
5	CAN2_L

(6) CAN3/4	
1	CAN3_H
2	CAN3_L
3	CAN3/4_GND (OUT)
4	CAN4_H
5	CAN4_L

(7) N/A	
1	
2	
3	
4	
5	

(8) N/A	
1	
2	
3	
4	
5	

ecomat100

Control systems

ifm electronic

CR3101

CANmem
Data memory and logger
for CANopen systems

Use of SD/MMC cards
and memory cards
to PCMCIA standard

Parameter setting
to IEC 61131

10 ... 30 V DC

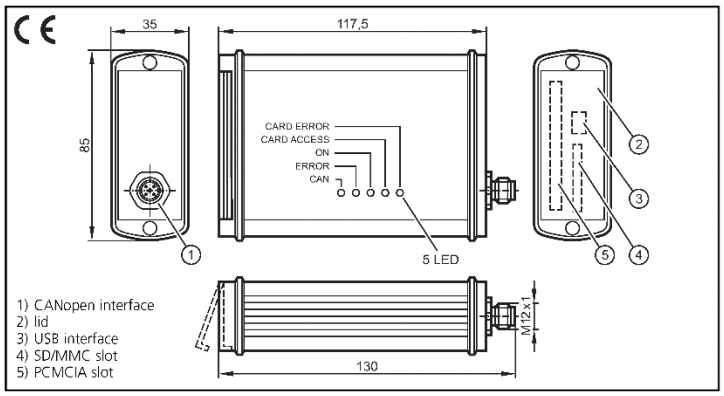

Application	e.g. parameter setting of mobile machines and installations storage of remote diagnostic data or alarm and error messages
Mechanical data	
Housing	aluminium
Dimensions (w x h x d)	117.5 x 85 x 35 mm
Mounting	with mounting bracket (prepared mounting bores on the sides, see mounting variants)
Protection	IP 65
Operating temperature (device)	-20 ... +80 °C (memory card depending on the type)
Storage temperature (device)	-40 ... +80 °C (memory card depending on the type)
Weight	250 g
Electrical data	
Operating voltage	10...30 V DC supply via M12 plug
Current consumption	120 mA (at 24 V DC)
Interfaces	
CAN interface	CAN interface 2.0 B, ISO 11898 M12 plug for operating voltage and CAN bus, 5 pins (type Lumberg) CAN electrically separated
Baud rate	20 Kbits/s...1 Mbits/s (default setting 125 Kbits/s)
Communication profile	CANopen, CiA DS 301 version 3.0
Node ID (default)	hex 20 (= 32)
USB interface	USB type mini B (female) (for PC communication, configuration and firmware update)
SD/MMC slot	Secure Digital (SD) or Multi Media Card (MMC)
PCMCIA slot	for SRAM PC card type I up to 16 Mbytes (preferably 1 Mbyte)
Other	
Integrated real-time clock	enables exact data evaluation by time stamp, e.g. for use as error memory or crash recorder (black box)
Display (status LEDs)	Memory card error (CARD ERROR) Memory card access (CARD ACCESS) Operating voltage (ON) Communication fault (ERROR) CAN mode (CAN)

\DATEN\100\DB-FORM—PZD/03/12/96

ecomat100®

Control systems

ifm electronic

CR3101

Mounting variants

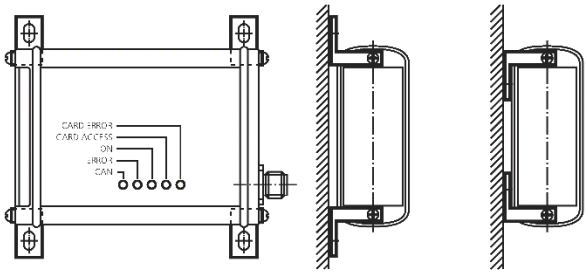

Variante A Variante B

Wiring CAN
(5 pole M12 plug)

Description	Pin	Potential
Operating voltage	1	GND
	2	10...30 V DC
CAN interface	3	CAN_GND
	4	CAN_H
	5	CAN_L

Wiring USB
(5 pole type mini B)

Pin	Potential
1	+ 5 V
2	Data –
3	Data +
4	ID (n.c.)
5	GND

Accessories
(to be ordered separately)

USB cable
type A – type mini B
length 1.8 m
Order no. EC2058

SRAM memory card (PCMCIA type 1) MByte
Order no. EC1020

Software

CANmem
(configuration and evaluation software)
Order no. CP9012

Note

The software can be obtained on request
or downloaded via the Internet (www.ifm-electronic.com) free of charge.

efector600

TA3333

TA-060FLDN14-A-ZVG/US/

Temperature sensors

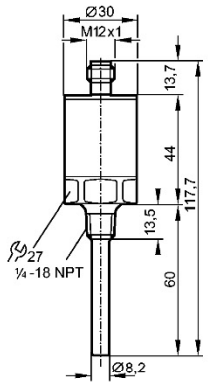

Made in USA

Product characteristics			
Temperature transmitter			
Quick disconnect			
Process connection: ¼" NPT			
Installation length EL: 60 mm			
Max. medium temperature			
150°C / 302°F (max. 40 perc)			
Analog output			
Measuring range: -17.8...148.9 °C / 0...300 °F			
Measuring element: 1 x Pt 1000, to DIN EN 60751, class A			
Application			
Application		liquids and gases	
Minimum installation depth	[mm]	15	
Electrical data			
Electrical design		DC	
Operating voltage	[V]	10...30 DC	
Protection class		III	
Reverse polarity protection		yes	
Outputs			
Output		Analog output	
Output function		4...20 mA analog	
Overload protection		yes	
Analog output		4...20 mA; Rmax: 500 Ω	
Measuring / setting range			
Measuring range		-17.8...148.9 °C	0...300 °F
Resolution			
Analog output	[K]	< 0.02	
Accuracy / deviations			
Analog output	[K]	± 0.4	
Temperature coefficients (in % of the span per 10 K)		< ± 0.1 *****)	

efector600

TA3333

TA-060FLDN14-A-ZVG/US/

Temperature sensors

Reaction times		
Dynamic response	T05 / T09 [s]	1 / 3 *)
Environment		
Pressure rating	[bar]	300
Ambient temperature	[°C]	-25...70
Storage temperature	[°C]	-40...100
Protection		IP 68 / IP 69K
Tests / approvals		
EMC		EN 61000-4-2 ESD: 4 kV CD / 8 kV AD EN 61000-4-3 HF radiated: 10 V/m EN 61000-4-4 Burst: 2 kV EN 61000-4-5 Surge: 1 kV EN 61000-4-6 HF conducted: 10 V
Shock resistance		DIN EN 60068-2-27: 50 g (11 ms)
Vibration resistance		DIN EN 60068-2-6: 10 g (10...2000 Hz)
MTTF	[Years]	1119
Mechanical data		
Process connection		¼" NPT
Materials (wetted parts)		stainless steel 316L / 1.4404
Probe length L	[mm]	46.5
Installation length EL	[mm]	60
Housing materials		stainless steel 316L / 1.4404; stainless steel (304S15); stainless steel (303S22); PA
Weight	[kg]	0.124
Electrical connection		
Connection		M12 connector; gold-plated contacts

Wiring

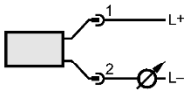

Remarks		
Remarks		cULus - Class 2 source required *) according to DIN EN 60751 *****) In case of deviation from the reference condition 25 ± 5 °C The values for accuracy apply to flowing water.
Pack quantity	[piece]	1

TEMPERATURE SENSORS

Vibration Resistant and Bendable RTD (Pt100) Probes with M12 Connector and Mounting Threads, Standard Sizes

PR-26 Series

ACCURACY IEC CLASS A (±0.15°C @ 0°C) Up to 300°C

ACCURACY IEC CLASS B (±0.30°C @ 0°C) 300 to 500°C

- All Welded 316L Stainless Steel Housing
- Operating Temperature Range: -50 to 500°C (-58 to 932°F) Sensing End, -50 to 250°C (-58 to 482°F) at Connector
- Available With or Without Mounting Thread (¼, ⅜ and ½ NPT Mounting Threads Available)
- Pt100 or Pt1000 4-Wire Platinum RTD Elements (IEC60751) Class A from -50 to 300°C, Class B from 300 to 500°C
- Integral 4-Pin M12 Connector for Easy Connection
- ¼" Diameter Standard
- 2½" Minimum Length
- Bendable Probes (After the First 2½" of Probe Tip) Using a Minimum Suggested Bend Radius of 2x the Probe Diameter
- Vibration Tested to MIL-STD-202G, Method 204D, Test Condition A, 10g's from 10 to 500 Hz (6" Long or Shorter)

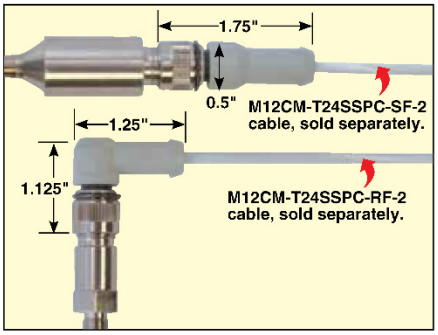

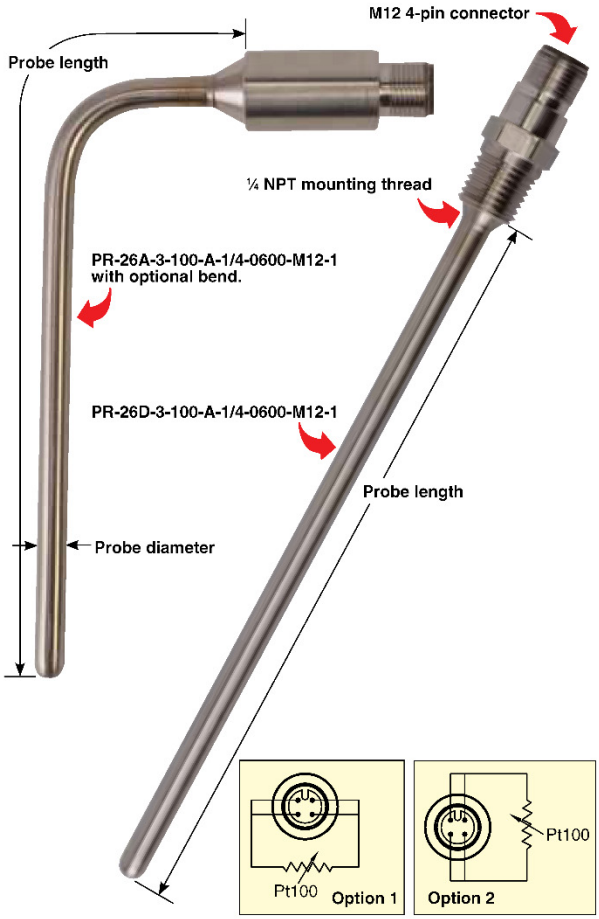

To Order

Model Number	Element	Length (inch)	Mounting Thread
PR-26A-3-100-A-1/4-0600-M12-1	Pt100, Class A	6.00	None
PR-26B-3-100-A-1/4-0600-M12-1	Pt100, Class A	6.00	½ NPT
PR-26C-3-100-A-1/4-0600-M12-1	Pt100, Class A	6.00	⅜ NPT
PR-26D-3-100-A-1/4-0600-M12-1	Pt100, Class A	6.00	¼ NPT
PR-26A-3-1000-A-1/4-0600-M12-1	Pt1000, Class A	6.00	None
PR-26B-3-1000-A-1/4-0600-M12-1	Pt1000, Class A	6.00	½ NPT
PR-26C-3-1000-A-1/4-0600-M12-1	Pt1000, Class A	6.00	⅜ NPT
PR-26D-3-1000-A-1/4-0600-M12-1	Pt1000, Class A	6.00	¼ NPT

*For lengths other than 6", change **"0600"** in model number to required length and add additional cost per inch greater than 6" (example: 9" = **0900**, 4½" = **0450**).*

*For option 2 wiring change **"-1"** to **"-2"**, no additional charge.*

***Ordering Examples: PR-26A-3-100-A-1/4-0600-M12-1,** ¼" diameter probe, 6" long with Pt100, Class A element, no mounting thread, with M12 connector.*

***PR-26D-3-100-A-1/4-0600-M12-1,** ¼" diameter probe, 6" long with Pt100, Class A element, ¼ NPT mounting thread, with M12 connector.*

Mini Temperature Transmitter
With M12 Connectors

C

TX-M12-RTD Series

- **M12 Connectors for Fast Connection of Sensors and Intrumentation**
- **Use with 2, 3 or 4-Wire Pt100, Pt500 or Pt1000 Sensors**
- **-40 to 85°C (-40 to 185°F) Ambient Operating Temperature**
- **-200 to 850°C (-328 to 1862°F) Measurement Range**
- **Small, 38 mm Diameter Housing; Weighing Just 100 Grams**
- **4 to 20 mA or 0 to 10 Vdc Output Models**
- **IP67 Stainless Steel Enclosure**

OMEGA's TX-M12-RTD Series transmitters offer improved performance over conventional in-head transmitters yet are a fraction of their size and weight. Integral M12 connectors maintain IP67 protection and connection integrity whilst allowing for a quick and simple change of sensor. Two models are available with either 4 to 20 mA or 0 to 10 Vdc output. Default scaling for the full output is 0 to 100°C (32 to 212°F), other ranges can be scaled at time of purchase for an additional charge; or the optional USB programming module (USB-CONFIG-UNIT) will allow the end user to perform scaling.

The TX-M12-RTD transmitter is ideal for use with OMEGA's PR-21 and PR-22 Series RTD probes, or any RTD probes with an M12 "A" coded Pin style connector which connects directly to theTX-M12-RTD sensor input. Other RTD probes may be easily connected using the M12-R-M-FM or M12-S-M-FM plug style field mountable connectors which have screw terminals connections

TX-M12-RTD-C transmitter shown larger than actual size.

Dimensions: mm (in) Ø = diameter

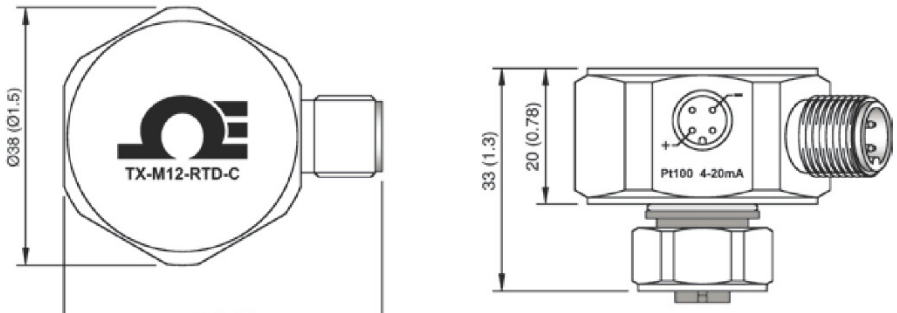

C-1

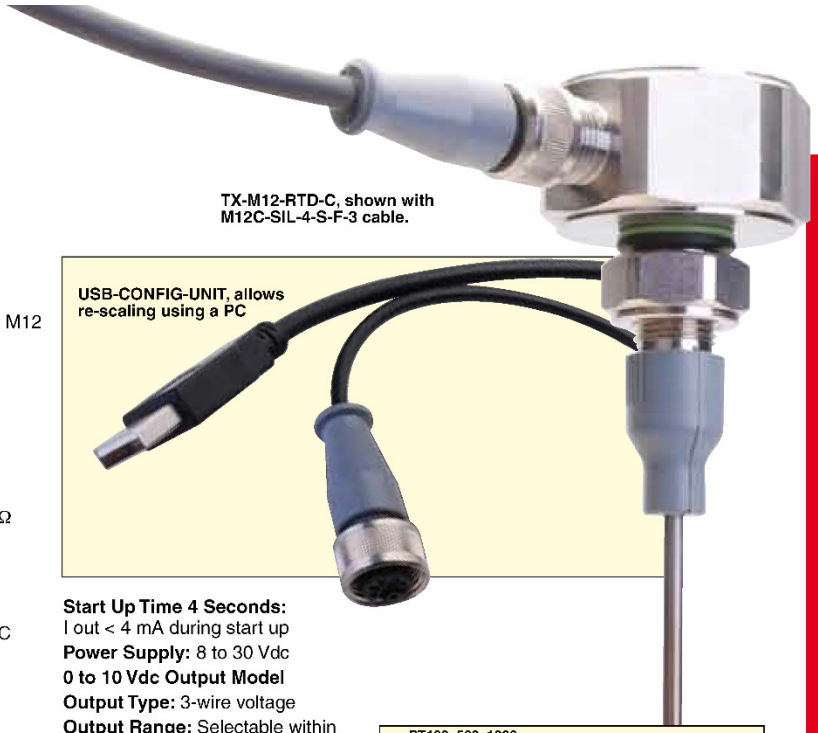

TX-M12-RTD-C, shown with M12C-SIL-4-S-F-3 cable.

USB-CONFIG-UNIT, allows re-scaling using a PC

C

Specifications

Update Time: 200 mS
Response Time: 0.5 seconds
Warm-up Time: 1 minute to full accuracy
Sensor Connection: 2, 3 or 4-wire M12
Minimum Span: 25°C
Thermal Drift
Pt100: 0.013 Ω/°C
Pt500/Pt1000: 0.063 Ω/°C
Accuracy: ±0.2°C + (0.05%) + output accuracy
Excitation Current: <200 uA
Lead Resistance Effect: 0.002°C/Ω
Maximum Lead Resistance: 20 Ω per leg
Operating Ambient: -40 to 85°C; 10 to 90% RH (non condensing)
Configuration Ambient: 10 to 30°C
Weight: Approx 100 g

4 to 20 mA Output Model
Output Type: 2-wire, 4 to 20 mA current loop
Output Range: 4.0 to 20.0 mA
Output Connection: M12 connector
Output Limits: 3.8 to 21.5 mA
Accuracy: mA output/2000 or 5 uA (whichever is the greater)
Loop Voltage Effect: 0.2 uA/V
Thermal Drift: 1 uA/°C
Maximum Output Load: [(Vsupply-10)/20] KΩ
Start Up Time 4 Seconds: I out < 4 mA during start up
Power Supply: 8 to 30 Vdc

0 to 10 Vdc Output Model
Output Type: 3-wire voltage
Output Range: Selectable within 0 to 10V
Current Drive: 2 mA max
Output Connection: M12 connector
Output Limits: -0.1 to 10.5V
Accuracy: Voltage output/1000 or 5 mV (whichever is the greater)
Thermal Drift: 1 mV/°C
Minimum Output: Load 5000 Ω
Power Supply: 12 to 30 Vdc

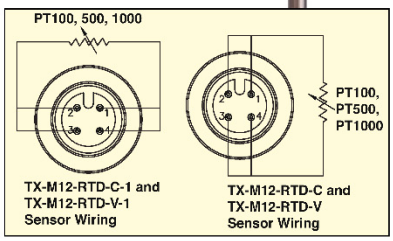

To Order	
Model Number	**Description**
TX-M12-RTD-C	4 to 20 mA output, connect to PR-21, -2 wiring, PR-22 and P-L-M12 sensors
TX-M12-RTD-C-1	4 to 20 mA output, connect to PR-21, -1 wiring, PRS-M12 and PR-25AP sensors
TX-M12-RTD-V	0 to 10 Vdc output, connect to PR-21, -2 wiring, PR-22 and P-L-M12 sensors
TX-M12-RTD-V-1	0 to 10 Vdc output, connect to PR-21, -1 wiring, PRS-M12 and PR-25AP sensors
M12C-SIL-4-S-F-3	Extension cable with straight socket M12 connector and 3 meters of silicone insulation cable
PR-22-3-100-A-1/8-0600-M12	Pt100 RTD probe, 1/8" diameter x 6" L with overmolded M12 plug connector
Accessories	
Model Number	**Description**
USB-CONFIG-UNIT	Software and interface/cable to allow scaling of transmitters with a PC
FS20	Factory scaling chargefor ranges other than the 0 to100°C, please specify range required

Comes complete with transmitter and operator's manual (USB-CONFIG-UNIT interface cable sold separately).

***Ordering Examples: TX-M12-RTD-C,** RTD transmitter set for a Pt100 sensor input, and 4 to 20 mA output over the range of 0 to 100°C (32 to 212°F).*

***TX-M12-RTD-V,** RTD transmitter set for a Pt100 sensor input, with a 0 to 10 Vdc output over the temperature range of 0 to 100°C (32 to 212°F) and **M12C-SIL-4-S-F-3,** M12 extension cable with 4-conductor #24 AWG stranded, silicone insulated and jacketed wire, straight socket style A-coded M12 connector one end, stripped leads the other, 3 meters long.*

C-2

efector500

PT3553

PT-025-SBG14-A-ZVG/US/ /W

Pressure sensors

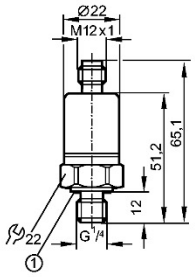

1: FKM seal / DIN 3869-14
tightening torque 25 Nm

Made in Germany

Product characteristics		
Electronic pressure sensor		
for mobile applications		
e1 compliant		
Process connection: G ¼ A		
Analogue output		
Measuring range: 0...25 bar		
Application		
Application		Type of pressure: relative pressure Liquids and gases
Pressure rating	[bar]	60
Bursting pressure min.	[bar]	600
Medium temperature	[°C]	-25...90 ****)
Electrical data		
Electrical design		DC
Operating voltage	[V]	8.5...36 DC
Insulation resistance	[MΩ]	> 100 (80 V DC)
Protection class		III
Reverse polarity protection		yes
Outputs		
Output		Analogue output
Output function		4...20 mA analogue
Analogue output		4...20 mA
Max. load	[Ω]	(Ub - 8.5 V) x 50; 775 at Ub = 24 V
Measuring / setting range		
Measuring range	[bar]	0...25
Accuracy / deviations		
Accuracy / deviations (in % of the span)		
Characteristics deviation *)		< ± 1.8
Linearity		< ± 0.25 (BFSL) / < ± 0.5 (LS)
Hysteresis		< ± 0.2
Repeatability **)		< ± 0.1

efector500

PT3553

PT-025-SBG14-A-ZVG/US/ /W

Pressure sensors

Long-term stability ***)		< ± 0.1	
Temperature coefficients (TEMPCO) in the temperature range -25...90° C (in % of the span per 10 K)			
Greatest TEMPCO of the zero point		< ± 0.1	
Greatest TEMPCO of the span		< ± 0.1	
Reaction times			
Step response time analogue output	[ms]	8	
Environment			
Ambient temperature	[°C]	-25...90 ****)	
Storage temperature	[°C]	-40...100	
Protection		IP 67 / IP 69K	
Tests / approvals			
EMC		EN 61000-4-2 ESD: noise immunity ISO 11452-2 ISO 11452-4 ISO 7637-2 radiation of interference EN 61000-6-1 EN 61000-6-4	4 kV CD / 8 kV AD according to the automotive directive 95/54/EC 04/104EC / 05/83EC 100 V/m 100 mA / severity level 4 severity level 4 according to CISPR 25
Shock resistance		DIN IEC 68-2-27:	50 g (11 ms)
Vibration resistance		DIN IEC 68-2-6:	20 g (10...2000 Hz)
MTTF	[Years]	1494	
Mechanical data			
Process connection		G ¼ A	
Materials (wetted parts)		stainless steel 316L / 1.4404; sealing: FPM (Viton)	
Housing materials		stainless steel 316L / 1.4404; TROGAMID	
Min. pressure cycles		50 million	
Weight	[kg]	0.08	
Electrical connection			
Connection		M12 connector	

Wiring

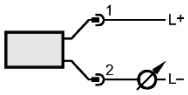

Remarks		
Remarks		*) incl. drift due to tightening torque, zero and span error **) with temperature fluctuations < 10 K ***) in% of the span / 6 months ****) -40...100°C upon request BFSL = Best Fit Straight Line / LS = Limit Value Setting
Pack quantity	[piece]	1

FLOMEC

DUALPULSE – insertion flowmeters

DP490 & DP525 are cost effective stainless steel flowmeters for measuring the flow of water, fuels & other low viscosity liquids in pipes sizes 1.5"~100" *(40~2500mm).* Insertion flowmeters are installed with the metering head 1/8th into the pipe resulting in very little pressure drop. They do not require external power when used with the Flomec rate totalizers, however some options such as high temperature & non-magnetic models require external power.

Applications include HVAC, hot & chilled water, fire systems, water distribution (management & treatment), boiler feed water & hydrant flow testing.

FEATURES:

- IP68 (NEMA6) submersible 316SS construction.
- Low cost of ownership, wide flow range.
- Rugged & compact design.
- Intrinsically safe hazardous area versions.
- Integral or remote pre-amplifiers & flow instruments.
- DP525 version suitable for "hot tap" installation.
- Quadrature pulse output option & Bi-Directional Flow Measurement
- Integral 4-20mA output option

General Specifications

Model Prefix	DP490	DP525
Suit pipe sizes	40~900mm (1.5" ~ 35")	50~2500mm (2"~100")
Pipe connection	1.5" or 2" BSPT or NPT male	2" BSPT or NPT male
Flow range	0.25 ~ 6300 litres/sec (4 ~ 99600 USGM)	0.4 ~ 49000 litres/sec (6 ~ 780000 USGM)
Flow velocity range	0.3 ~ 10 metres/sec (1 ~ 33 feet/sec)	
Linearity	typically ± 1.5% with well-established flow profile	
Temperature range	-40ºC ~ +150ºC (-40ºF ~ +300ºF)	
Maximum pressure	*80 bar (1160 psig)*	
Materials	316ss body & rotor shaft, PVDF rotor (PEEK rotor optional)	
Pulse Outputs		
Reed switch	30Vdc x 200mA (max.), Nom. 0 ~ 80hz*	
Hall effect	3 wire NPN, 5 ~ 24 VDc, 20mA (max.) Nom. 0 ~ 240hz	
Voltage Pulse	Self-Generated voltage. Nom. 0 ~ 240hz	
Non-magnetic sensor	3 wire NPN, 5~24Vdc max., 20mA max. Nom. 0 ~ 240hz	
Optional outputs	4~20mA, scaled pulse, quadrature pulse, flow alarms or two stage batch control	
Protection class	IP68 (NEMA6), integral ancillaries can be supplied I.S. (intrinsically safe)	
Overall dimensions	Refer over page	

* Reed Switch resolution is 1/3rd that of the NPN Hall Effect or Voltage pulse outputs.

FLOMEC

Over all Dimensions:

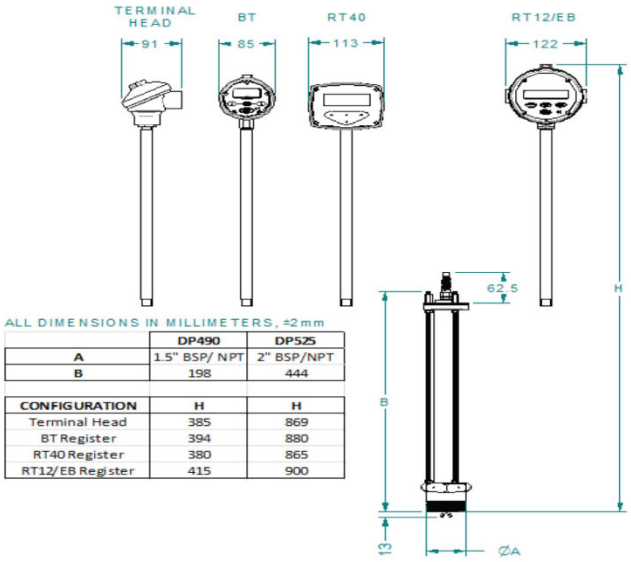

ALL DIMENSIONS IN MILLIMETERS, ±2mm

	DP490	DP525
A	1.5" BSP/ NPT	2" BSP/NPT
B	198	444

CONFIGURATION	H	H
Terminal Head	385	869
BT Register	394	880
RT40 Register	380	865
RT12/EB Register	415	900

Standard Installation:

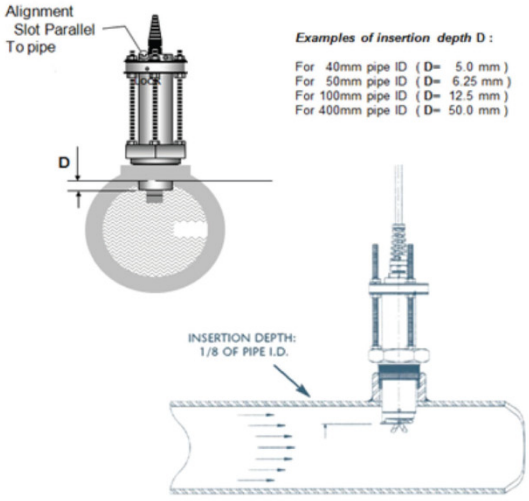

Examples of insertion depth D :

For 40mm pipe ID (**D=** 5.0 mm)
For 50mm pipe ID (**D=** 6.25 mm)
For 100mm pipe ID (**D=** 12.5 mm)
For 400mm pipe ID (**D=** 50.0 mm)

FLOMEC

Model Coding – Dual Pulse Insertion Flowmeters:

DP490	1.5 to 36" pipes *(40 ~ 900mm)*
DP525	2 to 100" pipes *(50 ~ 2500 mm)* suitable for "hot-tap" installations *(valve not included)*

Body material

S	316 Stainless Steel

Rotor & bearing materials

1	PEEK high temperature rotor with stainless steel rotor shaft; - 150°C *(300°F)*
2	PVDF rotor with 316 stainless steel rotor shaft *(standard)*; 100°C (212°F)

O-ring materials

1	Viton (standard); -15°C *(5°F) minimum*
2	EPR *(Ethylene Propylene Rubber): -40~+125°C (-40~+260°F)*
3	Teflon encapsulated viton or application specific; -15°C (5°F) minimum
4	Buna-N *(Nitrile)*, -40~+100°C (-40~+212°F)

Temperature limits

5	100°C (212°F) standard, *(85°C [185°F] maximum for non magnetic output type 4) and FI 4-20mA*
2	125°C (260°F) - *available with electrical connections 5 & 6 & PEEK rotor only*
3	150°C (300°F) - NPN output only *(available with electrical connection 5 & PEEK rotor only)*

Process connections

-	**1**	BSPT male thread - *1½" (DP490)* 2" *(DP525)*
-	**2**	NPT male thread - *1½" (DP490)* 2" *(DP525)*
-	**3**	2" BSPT male thread on the DP490
-	**4**	2" NPT male thread on the DP490

Pick-up type

1	NPN open collector & voltage pulse *(standard)*
2	NPN open collector(s) only (*for temp code 3 or QP option*)
3	Reed switch only *(may be used with an I.S. barrier or instrument in hazardous areas)*
4	Non magnetic rotor with NPN output *(for liquids with ferrous impurities, needs power)*
8	NPN open collector & Reed Switch

Electrical connections

1	3 metres cable [10ft] *(standard)*
2	10 metres cable [33ft]
3	20 metres cable [66ft]
4	50 metres cable [164ft] *(for longer lengths refer to factory)*
5	Terminal box on stem kit *(add this for integral output option FI, 4~20mA output)*
6	Stem kit *(price included with integral options B2, B3, R2, R3 & E0)*

Integral options

	QP	Quadrature pulse output (*requires PD2 for bi-directional flow capability*)
with scaleable pulse output	**B2**	BT11 dual totaliser *(with scaleable pulse output)*
IECEX & ATEX approved	**B3**	I.S. intrinsically safe BT11 including output
scaled pulse, alarms & 4~20mA	**R0**	RT12 rate totaliser with all outputs (Alloy housing)
scaled pulse, alarms & 4~20mA	**R2**	RT12 rate totaliser with all outputs
IECEX & ATEX approved	**R3**	I.S. intrinsically safe RT12 with all outputs
scaled pulse + backlighting	**R4**	* RT40 large LCD flow rate totaliser
	FI	Loop powered 4~20mA analog output *(also add elec. connection 5 terminal box on stem kit)*
	E0	Ecobatch dc powered two stage batch controller
	SB	Specific build requirement

max Max Machinery, Inc.
an ISO 9001:2008 certified company

Model 214 Piston Flow Meter (Analog)
5 cc/min to 10,000 cc/min

SPECIFICATIONS

Flow Range	5 cc/min to 10,000 cc/min
Accuracy (at 3 cP)	± 0.2% of reading over a 200:1 range, or ± 2mV (or 4µA), whichever is greater
Maximum Operating Pressure	70 bar or 210 bar (1000 or 3000 psi)
Displacement	10.5 cc/rev
Weight	3.7 kg
Recommended Filtration	10 micron
Port Size(s)	3/8" NPT, #6 SAE or manifold mount
Fluids	Most non aqueous, hydrocarbon based fluids

MATERIALS OF CONSTRUCTION

Body	Stainless steel, type 303
Pistons	Nitride hardened stainless steel, type 303
Crankshaft	Stainless steel
Bearings	All ball bearings, 440C stainless steel
O Rings	Viton®- standard • Teflon®, Perfluoro elastomer

ANALOG TRANSMITTER

Output Signal	Any range of ± 10V or ± 20mA Linearized and damped with anti-dither protection
Power Supply Requirements	Two Models: 12Vdc @ 90 mA, 24Vdc @ 45 mA
Ambient Operational Range	-40°C to 80°C, Single piece – Two piece to 110°C
Metered Liquid Temp Range (based on 20° ambient)	-40°C to 90°C, Standard model -40°C to 225°C, Two piece high temperature model
Compliance	CE Certified, Ex-proof version available with ATEX/IECEx II 2 G Ex d IIB Tx Gb as well as UL, cUL certification for Class 1, Division 1, Groups C and D, Tx

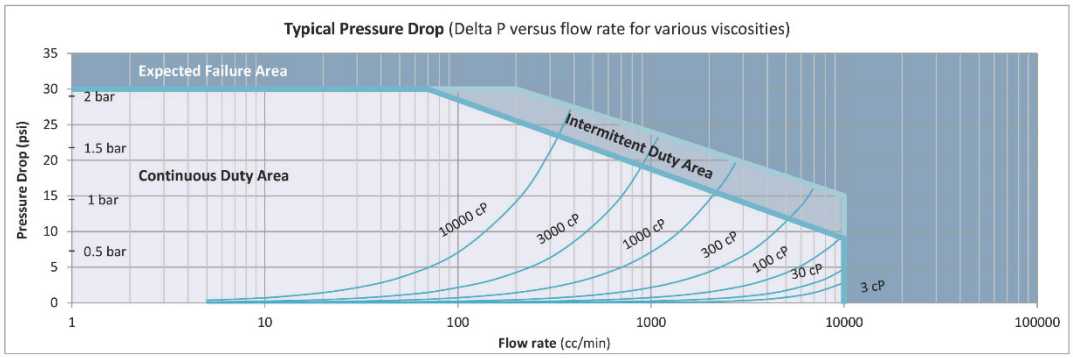

Model 214 Flow Meter (Analog)

CONNECTIVITY/DIMENSIONS (Not to scale)

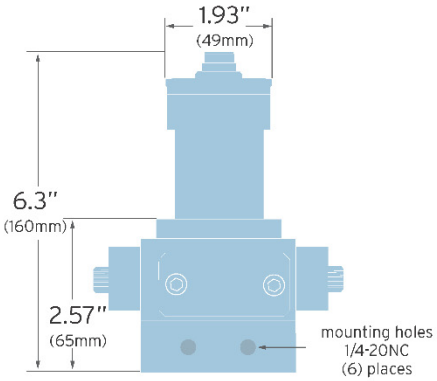

MODEL 214 WITH INDUSTRIAL HOUSING TRANSMITTER

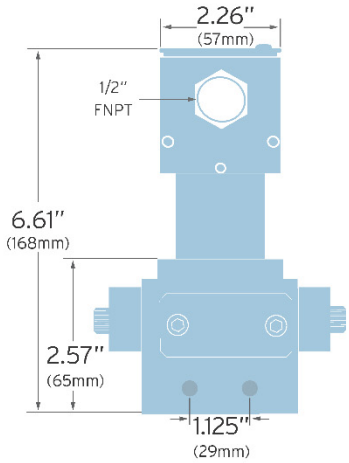

MODEL 214 WITH EX-PROOF HOUSING TRANSMITTER

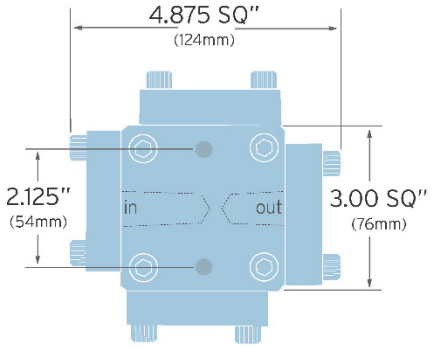

ELECTRICAL CONNECTION – ANALOG TRANSMITTERS

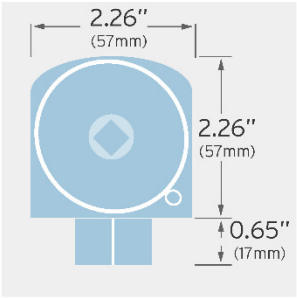

EX-PROOF HOUSING TOP VIEW

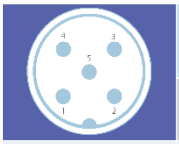	Turck® Connector		
	Pin #	Mating Cable Wire Color	NPT model
Case Ground	3	Blue	Case
Common	4	Black	Com
Power *	1	Brown	V+
Signal Output (+)	5	Grey	Sig
Signal Output (–)	2	White	Ret

* Please specify 12Vdc or 24Vdc operation

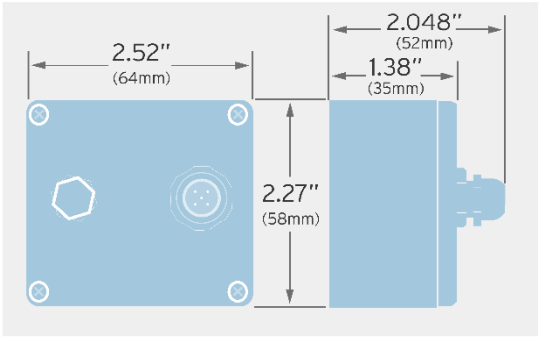

REMOTE PCA ENCLOSURE FOR HIGH TEMPERATURE TRANSMITTERS

Max Machinery, Inc.
maxmachinery.com
33A Healdsburg Avenue
Healdsburg, CA 95448
T +1 707.433.2662
F +1 707.433.1818

Bosch Motorsport | Lambda Sensor LSU 4.9

Lambda Sensor LSU 4.9

www.bosch-motorsport.com

BOSCH
Invented for life

- Application: lambda 0.65 to ∞
- Wide band
- Exhaust gas temperature range (max.) for short time ≤ 1,030°C
- Max. Hexagon temperature 600°C

This sensor is designed to measure the proportion of oxygen in exhaust gases of automotive engines (gasoline or Diesel).
The wide band lambda sensor LSU 4.9 is a planar ZrO_2 dual cell limiting current sensor with integrated heater. Its monotonic output signal in the range of lambda 0.65 to air makes the LSU 4.9 capable of being used as a universal sensor for lambda 1 measurement as well as for other lambda ranges. The connector module contains a trimming resistor, which defines the characteristic of the sensor.
The main benefit of the LSU 4.9 is the robust design combined with the high Bosch production quality standard.
This lambda sensor operates only in combination with a special LSU-IC, used in most Bosch Motorsport ECUs and lambda control units like LT4. You'll find this unit and more on our homepage at Data Logging Systems/ Sensor Interfaces.

Application

Application	lambda 0.65 to ∞
Fuel compatibility	gasoline/Diesel/E85
Exhaust gas pressure	≤ 2.5 bar (higher with decrease accuracy)
Exhaust gas temperature range (operating)	< 930°C
Exhaust gas temperature range (max.) for short time	< 1,030°C
Hexagon temperature	< 600°C
Wire and protective sleeve temperature	< 250°C
Connector temperature	< 140°C
Storage temperature range	-40 to 100°C
Max. vibration (stochastic peak level)	300 m/s^2

Technical Specifications

Variations

LSU 4.9 with automotive connector	
Connector	1 928 404 682
Mating connector	D 261 205 356-01
Pin 1	IP / APE
Pin 2	VM / IPN
Pin 3	Uh- / H-

2 | Lambda Sensor LSU 4.9

Pin 4	Uh+ / H
Pin 5	IA / RT
Pin 6	UN / RE
Wire length L	95.0 cm
LSU 4.9 with motorsports connector	
Connector	AS 6-07-35PN
Mating connector	AS 0-07-35SN
Pin 1	Uh+ / H
Pin 2	Uh- / H-
Pin 3	IP / APE
Pin 4	VM / IPN
Pin 5	UN / RE
Pin 6	IA / RT
Please specify the required wire length with your order.	

Mechanical Data

Weight w/o wire	120 g
Thread	M18x1.5
Wrench size	22 mm
Tightening torque	40 to 60 Nm

Electrical Data

Power supply H+ nominal	7.5 V
System supply voltage	10.8 V to 16.5 V
Heater power steady state	7.5 W
Heater control frequency	≥ 100 Hz
Nominal resistance of Nernst cell	300 Ω
Max current load for Nernst cell	250 µA

Characteristic

Signal output	I_P meas
Accuracy at lambda 0.8	0.80 ± 0.01
Accuracy at lambda 1	1.016 ± 0.007
Accuracy at lambda 1.7	1.70 ± 0.05

I_P [mA]	lambda	U_A [V], v=17	U_A [V], v=8
-2.000	0.650	-	0.510
-1.602	0.700	-	0.707
-1.243	0.750	0.192	0.884
-0.927	0.800	0.525	1.041
-0.800	0.822	0.658	1.104
-0.652	0.850	0.814	1.177
-0.405	0.900	1.074	1.299
-0.183	0.950	1.307	1.409
-0.106	0.970	1.388	1.448
-0.040	0.990	1.458	1.480
0	1.003	1.500	1.500
0.015	1.010	1.515	1.507
0.097	1.050	1.602	1.548
0.193	1.100	1.703	1.596
0.250	1.132	1.763	1.624
0.329	1.179	1.846	1.663
0.671	1.429	2.206	1.832
0.938	1.701	2.487	1.964
1.150	1.990	2.710	2.069
1.385	2.434	2.958	2.186
1.700	3.413	3.289	2.342
2.000	5.391	3.605	2.490
2.150	7.506	3.762	2.565
2.250	10.119	3.868	2.614

Please note: U_A is not an output signal of the lambda sensor, but the output of the evaluation circuit. Only I_P correlates with the oxygen content of the exhaust gas. Amplification factor v=17 is typically used for lean applications (lambda>1), amplification factor v=8 is typically used for rich applications (lambda<1).

Heater Strategy

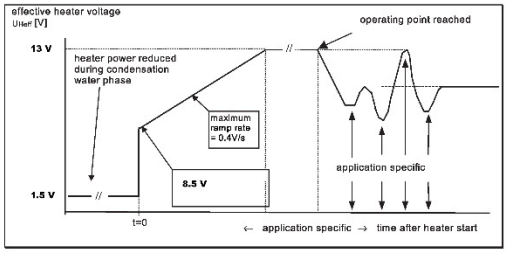

Connectors and Wires

Connector	Please see variations
Mating connector	Please see variations
Sleeve	fiber glass / silicone coated
Wire size	AWG 24
Wire length	Please see variations
Various motorsport and automotive connectors are available on request.	

3 | Lambda Sensor LSU 4.9

Installation Notes

This lambda sensor operates only in combination with a special LSU-IC, used in most Bosch Motorsport ECUs and lambda control units like LT4. You'll find this unit and more on our homepage at Accessories/Expansion Modules.

The lambda sensor should be installed at point which permits the measurement of a representative exhaust-gas mixture, which does not exceed the maximum permissible temperature.

Install at a point where the gas is as hot as possible.

Observe the maximum permissible temperature.

As far as possible install the sensor vertically (wire upwards).

The sensor is not to be fitted near to the exhaust pipe outlet, so that the influence of the outside air can be ruled out.

The exhaust-gas passage opposite the sensor must be free of leaks in order to avoid the effects of leak-air.

Protect the sensor against condensation water.

The sensor is not to be painted, nor is wax to be applied or any other forms of treatment. Use only the recommended grease for lubricating the thread.

Please find further application hints in the offer drawing at our homepage.

Ordering Information

Lambda Sensor LSU 4.9
With automotive connector, wire length 95 cm
Order number **0 258 017 025**

Lambda Sensor LSU 4.9
With motorsports connector. Please specify the required wire length with your order.
Order number **B 261 209 356-05**

Dimensions

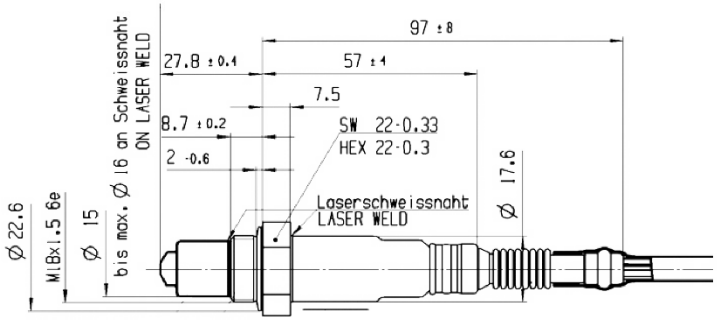

4 | Lambda Sensor LSU 4.9

Mounting recommendation

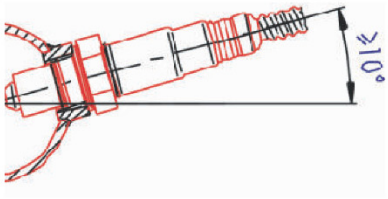

Recommended materials for the mating thread in the exhaust pipe
*: THexagon > 600°C or
TGas > 930°C

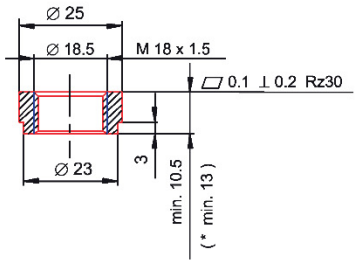

Represented by:

Europe:
Bosch Engineering GmbH
Motorsport
Robert-Bosch-Allee 1
74232 Abstatt
Germany
Tel.: +49 7062 911 79101
Fax: +49 7062 911 79104
motorsport@bosch.com
www.bosch-motorsport.de

North America:
Bosch Engineering North America
Motorsport
38000 Hills Tech Drive
Farmington Hills, MI 48331-3417
United States of America
Tel.: +1 248 876 2977
Fax: +1 248 876 7373
motorsport@bosch.com
www.bosch-motorsport.com

Latin America:
Robert Bosch Ltda
Motorsport
Av Juscelino Kubitscheck de
Oliveira 11800
Zip code 81460-900
Curitiba - Parana
Brasilia
Tel.: +55 41 3341 2057
Fax: +55 41 3341 2779

Asia-Pacific:
Bosch Engineering Japan K.K.
Motorsport
18F Queen's Tower C, 2-3-5 Minato Mirai
Nishi-ku, Yokohama-shi
Kanagawa 220-6218
Japan
Tel.: +81 45 650 5610
Fax: +81 45 650 5611
www.bosch-motorsport.jp

Australia, New Zealand and South Africa:
Robert Bosch Pty. Ltd
Motorsport
1555 Centre Road
Clayton, Victoria, 3168
Australia
Tel.: +61 (3) 9541 3901
motor.sport@au.bosch.com

2779147659 | en, V3, 08. Apr 2015

N. rev. / Rev. N.	Descrizione / Description	Data / Date	Firma / Signature	Contr. da / Ckd. by

LCU-ONE ANALOG PINOUT

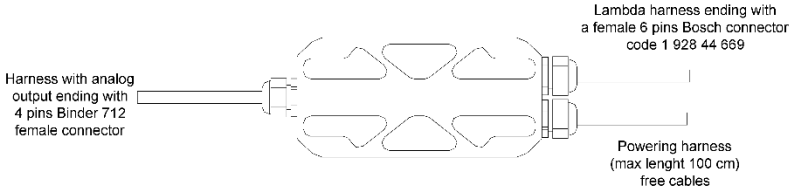

4 pins Binder 712
female connector
front view

6 pins Bosch female connector
code 1 928 404 669
contact insertion view

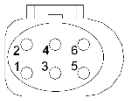

4 pins Binder 712 female connector pinout	
1	Lambda out
2	GND
3	RS232RX PC
4	RS232TX PC

6 pins Bosch female connetor pinout code 1 928 404 669	
1	IP+
2	IP-/VS
3	H-
4	H+
5	Rcal
6	VS+

Powering harness pinout (free cables)	
Cable colour	Function
Red	VBattery
Black	GND
Black	GND

Rif. / Ref.	Q.tà/Q.ty	Material / Material		N. articolo / Item N.	
Progettato da / Designed by	Contr. da / Ckd. by	Approvato da / Approved by	Nome file / File name	Data / Date	Scala / Scale

Racing Data Power

Titolo / Title

Pinout LCU-One Analog

N. disegno / Drawing N.

Rev. / Rev.

Foglio / Sheet
1 of 1

NORGREN

VP10
Electronic Pressure Regulator

- Reliable, rugged proportional I/P and E/P converter
- Suitable for a wide range of applications
- Excellent accuracy
- Minimum vibration effects
- IP65 environmental protection in normal operation

Technical Data

• Medium	Oil free, dry air, filtered to 5microns
• Output Pressure	See product selector
• Flow Capacity	Up to 300Nl/min (10scfm)
• Air Consumption	1.4 l/min (0.06scfm) typical
• Air Supply	At least 0.5bar above maximum required output pressure
• Connections	1/4" NPT or 1/4" BSP, 30mm square connector DIN 43650 provided
• Operating Temperature	-40° to +85°C
• Response Time	<2bar/30psig: less than 0.5seconds (dependent on input for 10-90% step change in outlet pressures) into a 10cc load
• Hysteresis	Maximum 0.35% of span
• Independent Linearity	Maximum 0.5% of span
• Temperature Effect	Average 0.1% of span/ °C for span and zero over operating range
• Supply Sensitivity	Better than 0.075% span output change per % supply pressure change
• Failure Mode	Signal falls to bleed pressure when electrical supply fails
• Mounting Position	Integral surface mounting bracket provided for preferred vertical mounting. 50mm pipe mounting kit available
• Material of Construction	Zinc die-casting passivated with epoxy paint, nitrile diaphragms, Be_2Cu flapper nozzle and supply valve
• Mass	825g

Ordering Information

To order please quote model number from the table overleaf.

Options

Alternative input signal ranges, alternative pressure ranges, conduit entry with flying leads, junction box, intrinsically safe/ ATEX certification, 50mm pipe mounting bracket, 1/8" NPT pneumatic connections, captured exhaust, reverse acting, split range.

For options not shown and any specific requirements please contact Norgren technical department

Symbol

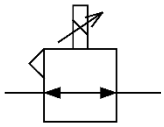

NORGREN

General Dimensions

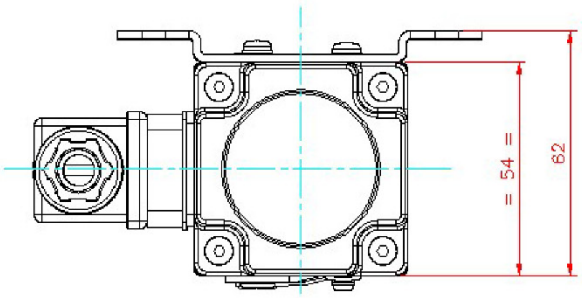

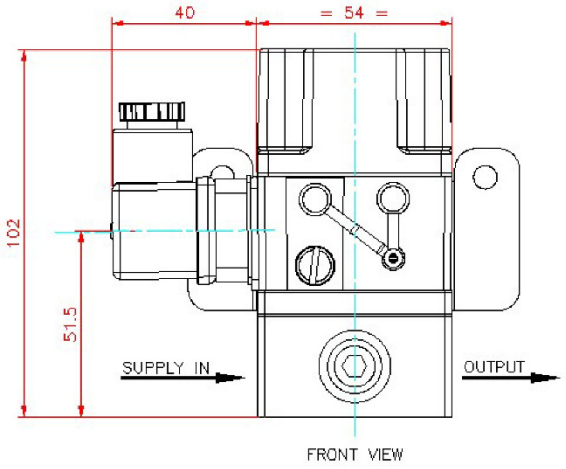

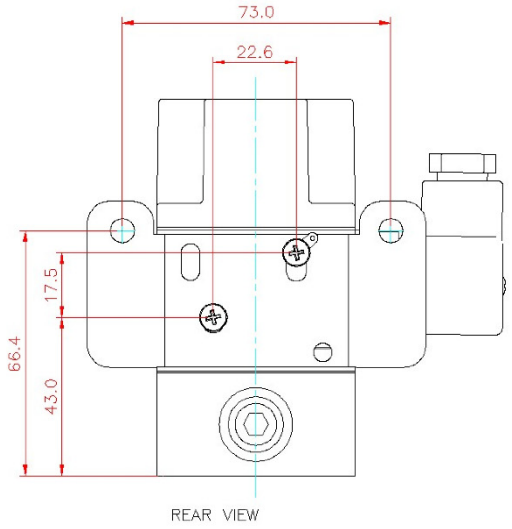

NORGREN

General Information

Product Selector

V P 1 0 * * * * * 0 * A 0 0

Pressure Range
01 (0.2-1bar/3-15psi)
02 (0.2-2bar/3-30psi)
04 (0.2-4bar/3-60psi)
06 (0.2-6bar/3-90psi)
08 (0.2-8bar/3-120psi)

Unit of Pressure
B (Bar Output)
P (PSI Output)

Power Supply
0 Not required (2 wire)
(Below 6bar/90psi requires 2 wires)
1 Required (3 wire)
(Above 6bar/90psi requires 3 wires)

Input Signal
1 (0-10V)
4 (4-20mA)

Port Size
J (1/4" BSP)
K (1/4" NPT)

Eg, Output pressure: 2bar, Port Size: 1/4" BSP, Input: 4-20mA
VP1002BJ400H00

Characteristic Curves

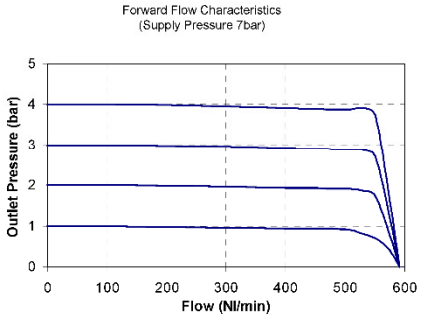

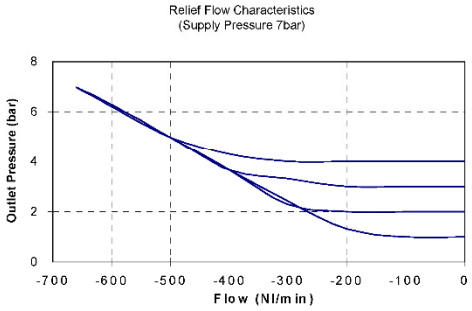

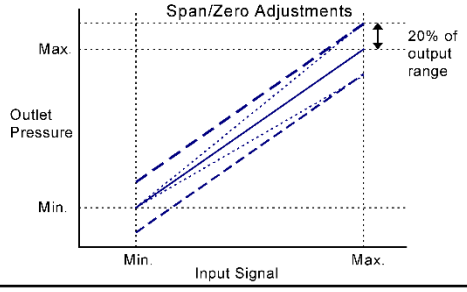

TECHNICAL DATASHEET #TDAX1302XX

PWM to Current (or Voltage) Signal Converter

P/N: AX13020X

PWM to
Current (or Voltage)
Signal Converter

- DIN rail mount
- Single channel
- PWM input
- 0-20 mA, 4-20 mA, 0-5VDC or 0-10VDC output (factory set)
- 12V/24VDC nominal

Description:
Isolated signal converters provide a compact solution for converting digital pulse width modulated (PWM) signal into a current or voltage signal. Current to PWM and Voltage to PWM signal converters are also available.

Applications:
Industrial control panels
Engine control panels

Ordering Part Numbers:

PWM to 0-20 mA output: **AX130200**
PWM to 4-20 mA output: **AX130201**
Open Collector PWM to 4-20 mA Output: **AX130204**
5 Hz PWM to 4-20 mA Output: **AX130206**
PWM to 0-5V output: **AX130202**
PWM to 0-10V output: **AX130203**

Block Diagram

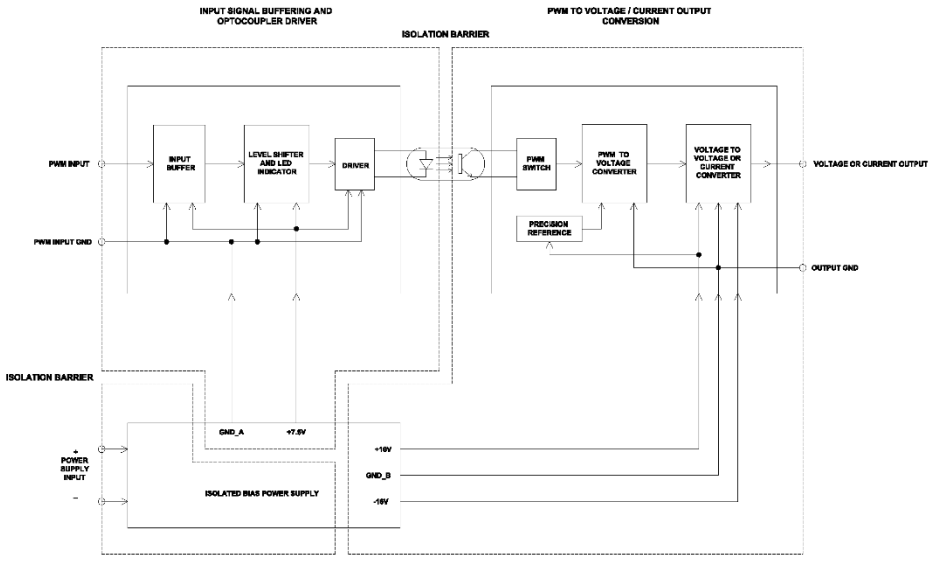

In Europe:
Axiomatic Technologies Oy
Höytämöntie 6
33880 LEMPÄÄLÄ - Finland
Tel. +358 3 3595 600
Fax. +358 3 3595 660
www.axiomatic.fi

In North America:
Axiomatic Technologies Corporation
5915 Wallace Street
Mississauga, ON Canada L4Z 1Z8
Tel. 1 905 602 9270
Fax. 1 905 602 9279
www.axiomatic.com

Technical Specifications:	
All specifications are typical at nominal input voltage and 25 degrees C unless otherwise specified.	
Input Specifications:	
PWM Frequency and Range	Fully isolated *Models AX130200, AX130201, AX130202, AX130203:* PWM 50 Hz to 50 kHz 0-100% Duty Cycle *Model AX130204:* Open Collector PWM Input with 10 kΩ pull- up resistor Model AX130206: 5 Hz to 1 kHz PWM, 0-100% Duty Cycle *Application-specific duty cycles are available on request.* *(A 5 Hz to 50 kHz PWM input model is available on request with a 3 second response time.)*
Input Voltage	Low <1.5V High >3.5V (50V max.) TTL and CMOS compatible
Input Impedance	200kOhm
Output Specifications:	
Voltage Output	Fully isolated Active output AX130202: 0-5 VDC AX130203: 0-10 VDC Accuracy: +/- 0.02V
Output Impedance	1 Ohm Transient protection is provided. Short circuit protection is provided.
Current Output	Fully isolated AX130200: 0-20 mA AX130201: 4-20 mA Accuracy: +/- 0.1 mA
Compliance Voltage	8.8VDC
Maximum Load Resistance	500 Ohms@ 20°C
General Specifications:	
Power Supply	12VDC or 24VDC nominal (8-36VDC range) Transient protection is provided. Overvoltage protection is provided.
Reverse Polarity Protection	Provided
Isolation	500Vrms (5 sec., 0.1 mA maximum)
Response Time	100 mSec.
Power Consumption	50 mA @ 12V; 30 mA @ 24V
Operating Conditions	-40 to 85 degrees C (-40 to 185 degrees F) 0-95% relative humidity
Adjustments	Span and Offset (Zero) are factory set. Trim pots are accessible by opening the front cover. Turn CW to increase. ZERO: Apply 0% PWM signal to the input. Adjust the trim pot to desired min. output. SPAN: Apply 100% PWM signal to the input. Adjust the trim pot to desired max. output.
Electrical connection	#12 to #22 AWG screw terminals
Packaging	PCB is conformal coated Housing (Wieland WEG8), Polyamide 6.6 plastic, UL94V-0 DIN rail mount, 35 mm
Dimensions	60.6 x 90.5 x 28.5 mm (W x H x D) 2.38 x 3.56 x 1.12 inches excluding DIN rail
Weight	0.15 lbs. (0.07 kg)
Protection	IP20
Grounding	The converter provides full isolation between input, output and power. Therefore, grounding is not necessary. If grounding is desired, however, the input, output and power grounds can be tied together. An Earth GND connection is provided for use in noisy environments.

Model	*Range of Zero*	*Range of Span*
AX130200	-0.65 to 1.17 mA	17.92 to 20.17 mA
AX130201	2.95 to 4.81 mA	18.63 to 20.46 mA
AX130202	-0.29 to 0.29 V	4.66 to 5.25 V
AX130203	-0.58 to 0.59 V	9.32 to 10.49 V

Dimensions, Connections and Adjustments

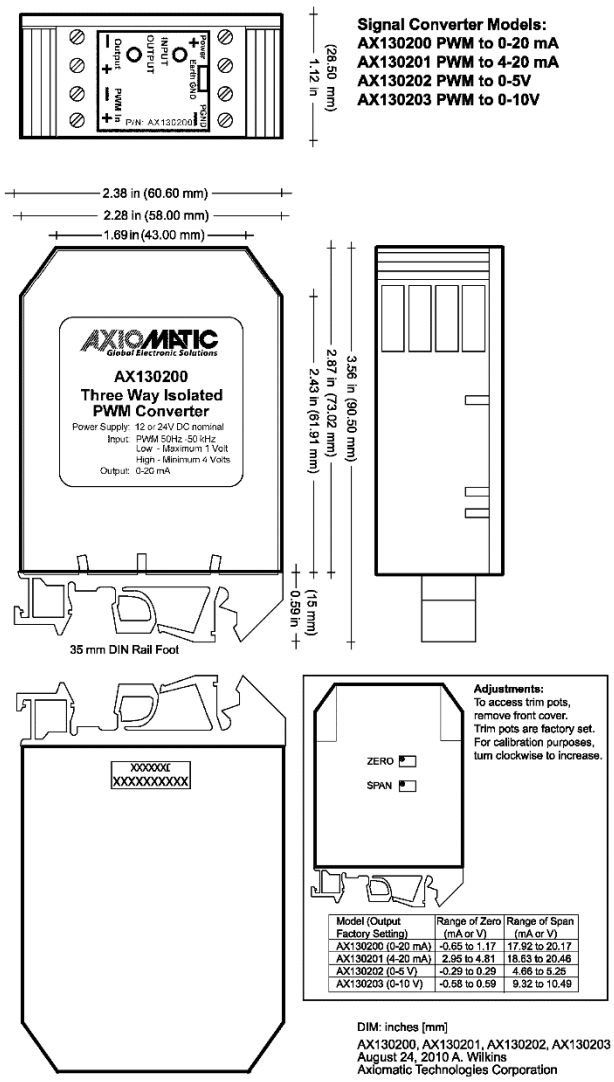

Model (Output Factory Setting)	Range of Zero (mA or V)	Range of Span (mA or V)
AX130200 (0-20 mA)	-0.65 to 1.17	17.92 to 20.17
AX130201 (4-20 mA)	2.95 to 4.81	18.63 to 20.46
AX130202 (0-5 V)	-0.29 to 0.29	4.66 to 5.25
AX130203 (0-10 V)	-0.58 to 0.59	9.32 to 10.49

Specifications are indicative and subject to change. Actual performance will vary depending on the application and operating conditions. Users should satisfy themselves that the product is suitable for use in the intended application.
All our products carry a limited warranty against defects in material and workmanship. Please refer to our Warranty, Application Approvals/Limitations and Return Materials Process as described on www.axiomatic.com/service.html.

Form: TDAX1302XX-11/24/14

snhy.com/FPCC

MODEL
FPCC

Electro-proportional flow control valve - normally closed
CAPACITY: 10 gpm | **CAVITY:** T-13A

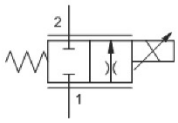

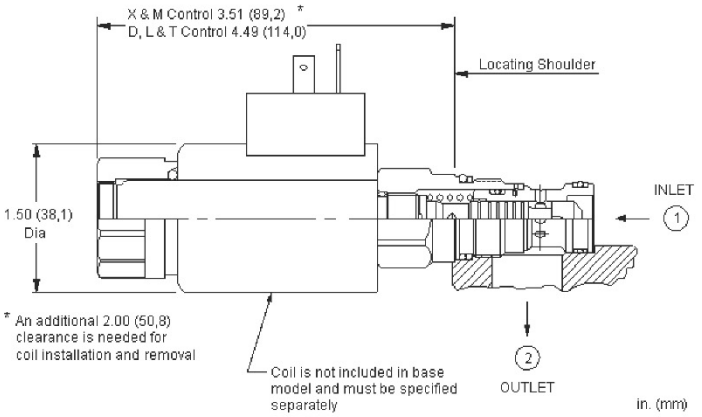

CONFIGURATION

X	Control	No Manual Override
C	Flow Rate	.25 - 7 gpm (1 - 28 L/min.)
N	Seal Material	Buna-N
(none)	Coil	No coil

NOTES

Please verify cartridge clearance requirements when choosing a Sun manifold. Different valve controls and coils require different clearances.

This valve is a normally-closed, electro-proportional throttle. The valve is spring biased closed. Energizing the coil generates an opening force on the spool proportional to the command current and this force is countered by the spring and flow forces. This force balance creates a metering orifice whose effective size is proportional to the current. The valve exhibits a large degree of self-compensation in the 1 to 2 direction and will provide proportional flow control in the 2 to 1 direction with the addition of an external compensator. Full reverse flow (2 to 1) with 100% command in the 2 to 1 direction is possible without a compensator under all conditions.

TECHNICAL DATA

Cavity	T-13A
Series	1
Capacity	10 gpm
Maximum Valve Leakage at 110 SUS (24 cSt)	6 in³/min.@3000 psi
Manual Override Force Requirement	5 lbs/1000 psi @ Port 1
Manual Override Stroke	.10 in.
Solenoid Tube Diameter	.75 in.
Valve Hex Size	7/8 in.
Valve Installation Torque	30 - 35 lbf ft
Model Weight (with coil)	1.10 lb
Seal kit - Cartridge	Buna: 990-413-007
Seal kit - Cartridge	Polyurethane: 990-413-002
Seal kit - Cartridge	Viton: 990-413-006
Seal and nut kit - Coil	Viton: 990-770-006
Model Weight	0.66 lb.

PROPORTIONAL PERFORMANCE DATA

Hysteresis (with dither)	<4%
Hysteresis with DC input	<8%
Linearity (with dither)	<2%

Repeatibility (with dither)	<2%
Recommended dither frequency	140 Hz
Deadband, nominal (as a percentage of input)	25%

SYMBOLS

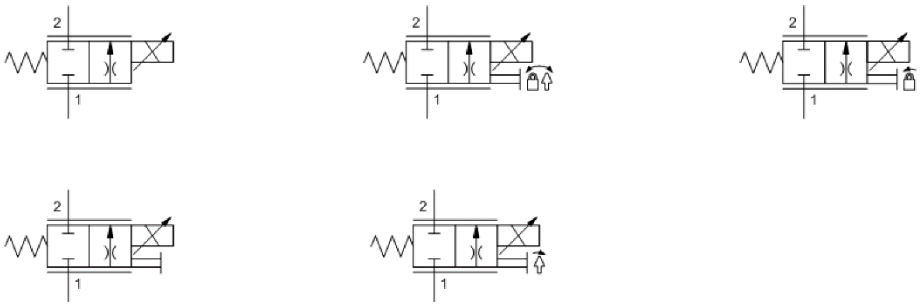

TECHNICAL FEATURES

- Available in either a normally open or normally closed configuration with three different capacity ranges.
- Capable of operating with pressures up to 5000 psi.
- Low leakage levels in the closed position.
- Coils are interchangeable with Sun's other full flow, solenoid-operated valves and can be mounted on the tube in either direction.
- This cartridge has several manual override choices, including no manual override. See Option Configuration.
- For optimum performance, an amplifier with current sensing and adjustable dither should be used. Dither should be adjustable between 100 - 250 Hz.
- On models equipped with the D or L control, the detent mechanism in the manual override is meant for temporary actuation. The D, E, L and T manual control assemblies have a mechanical life expectancy of approximately 7,000 cycles.
- The momentary/twist override option "E" allows the operator to shift the valve by twisting the manual override clockwise 90 degrees.
- Cartridges with EPDM seals are for use in systems with phosphate ester fluids. Exposure to petroleum based fluids, greases and lubricants will damage the seals.
- Incorporates the Sun floating style construction to minimize the possibility of internal parts binding due to excessive installation torque and/or cavity/cartridge machining variations.

PERFORMANCE CURVES

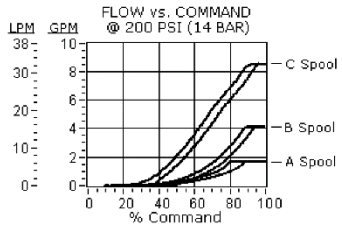

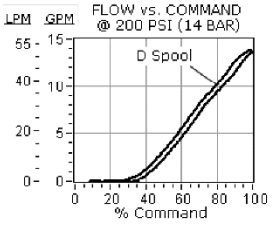

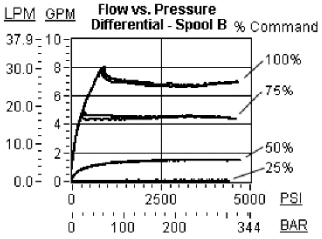

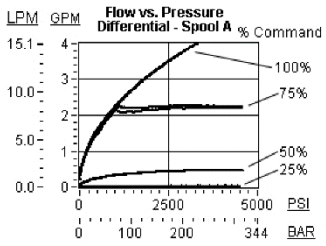

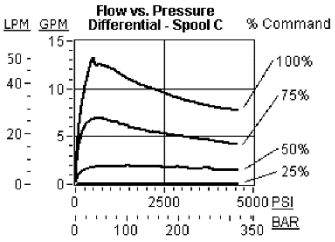

CONFIGURATION OPTIONS

	CONTROL	
Preferred Options	X	No Manual Override
Standard Options	D	Twist/Lock (Dual) Manual Override
	E	Twist (Extended) Manual Override
	L	Twist/Lock (Detent) Manual Override
	M	Manual Override
	T	Twist (Momentary) Manual Override
	FLOW RATE	
Preferred Options	C	.25 - 7 gpm (1 - 28 L/min.)
Standard Options	A	.1 - 1.5 gpm (0,4 - 6 L/min.)
	B	.15 - 3.5 gpm (0,6 - 14 L/min.)
	D	.25 - 10 gpm (1 - 40 L/min.)
	SEAL MATERIAL	
Preferred Options	N	Buna-N
Standard Options	E	EPDM
	V	Viton
	COIL	
		No coil
	212	DIN 43650 3 pin (Hirschman), 12 VDC
	212N	DIN 43650 3 pin (Hirschman), 12 VDC, no transient voltage suppression (TVS) diodes
	214N	DIN 43650 3 pin (Hirschman), 14 VDC, no transient voltage suppression (TVS) diodes
	224	DIN 43650 3 pin (Hirschman), 24 VDC
	224N	DIN 43650 3 pin (Hirschman), 24 VDC, no transient voltage suppression (TVS) diodes
	2B12A	DIN 43650 3 pin (Hirschman), command common on fourth pin, 12 VDC, 0-20 mA
	2B12B	DIN 43650 3 pin (Hirschman), command common on fourth pin, 12 VDC, Bluetooth, all functions enabled
	2B12V	DIN 43650 3 pin (Hirschman), command common on fourth pin, 12 VDC, 0-10V
	2B24A	DIN 43650 3 pin (Hirschman), command common on fourth pin, 24 VDC, 0-20 mA
	2B24B	DIN 43650 3 pin (Hirschman), command common on fourth pin, 24 VDC, Bluetooth, all functions enabled
	2B24V	DIN 43650 3 pin (Hirschman), command common on fourth pin, 24 VDC, 0-10V
	2C12V	DIN 43650 3 pin (Hirschman), +5V reference on fourth pin, 12 VDC, 0-10V
	2C24V	DIN 43650 3 pin (Hirschman), +5V reference on fourth pin, 24 VDC, 0-10V
	2D12A	DIN 43650 3 pin (Hirschman), enable input on fourth pin, 12 VDC, 0-20 mA
	2D24A	DIN 43650 3 pin (Hirschman), enable input on fourth pin, 24 VDC, 0-20 mA
	2D24V	DIN 43650 3 pin (Hirschman), enable input on fourth pin, 24 VDC, 0-10V
	2F12V	DIN 43650 3 pin (Hirschman), programmable ramps, separate rise and fall, 12 VDC
	2F24V	DIN 43650 3 pin (Hirschman), programmable ramps, separate rise and fall, 24 VDC
	4A12A	Deutsch DT04-6P, all functions enabled (separate command common, 5 v reference, and an enable), 12 VDC, 0-20 mA
	4A12B	Deutsch DT04-6P, all functions enabled (separate command common, 5 v reference, and an enable), 12 VDC, Bluetooth, all functions enabled
	4A12V	Deutsch DT04-6P, all functions enabled (separate command common, 5 v reference, and an enable), 12 VDC, 0-10V

Standard Options	4A24A	Deutsch DT04-6P, all functions enabled (separate command common, 5 v reference, and an enable), 24 VDC, 0-20 mA
	4A24B	Deutsch DT04-6P, all functions enabled (separate command common, 5 v reference, and an enable), 24 VDC, Bluetooth, all functions enabled
	4A24V	Deutsch DT04-6P, all functions enabled (separate command common, 5 v reference, and an enable), 24 VDC, 0-10V
	4F12V	Deutsch DT04-6P, programmable ramps, separate rise and fall, 12 VDC
	4F24V	Deutsch DT04-6P, programmable ramps, separate rise and fall, 24 VDC
	524	SAE J858A, 24 VDC
	612	AMP Junior Timer, 12 VDC
	612N	AMP Junior Timer, 12 VDC, no transient voltage suppression (TVS) diodes
	624	AMP Junior Timer, 24 VDC
	624N	AMP Junior Timer, 24 VDC, no transient voltage suppression (TVS) diodes
	712	Twin Lead, 12 VDC
	712N	Twin Lead, 12 VDC, no transient voltage suppression (TVS) diodes
	724	Twin Lead, 24 VDC
	724N	Twin Lead, 24 VDC, no transient voltage suppression (TVS) diodes
	812	Metri-Pack, 12 VDC
	812N	Metri-Pack, 12 VDC, no transient voltage suppression (TVS) diodes
	824	Metri-Pack, 24 VDC
	912	Deutsch DT04-2P, 12 VDC
	912N	Deutsch DT04-2P, 12 VDC, no transient voltage suppression (TVS) diodes
	914	Deutsch DT04-2P, 14 VDC
	914N	Deutsch DT04-2P, 14 VDC, no transient voltage suppression (TVS) diodes
	924	Deutsch DT04-2P, 24 VDC
	924N	Deutsch DT04-2P, 24 VDC, no transient voltage suppression (TVS) diodes
	HN24AA	Hazardous environment duty, 1/2 inch NPT mechanical conduit, 24 VDC, 10 feet twin lead, ATEX Certification Ex mb IIC T3 Gb.
	HN24AB	Hazardous environment duty, 1/2 inch NPT mechanical conduit, 24 VDC, 10 feet twin lead, CSA Certification

RELATED ACCESSORIES

773-812
12 VDC weatherized coil with Metri-Pack, Series 150-2M connector

773-814
14 VDC weatherized coil with Metri-Pack, Series 150-2M connector

773-824
24 VDC weatherized coil with Metri-Pack, Series 150-2M connector

773-828
28 VDC weatherized coil with Metri-Pack, Series 150-2M connector

991-056
T-13A and T-31A cavities, weatherized coil seal kit

991-225
Momentary/twist operation, manual override control kit, T control

991-226
Detent/lock operation, manual override control kit, L control

991-227
Dual twist/lock operation, manual override control kit, D control

991-238
Momentary/twist operation, extended resolution, manual override control kit, E control

991-240
Red momentary/twist operation, manual override control kit, T control

991-241

Red detent/lock operation, manual override control kit, L control

991-242
Red dual twist/lock operation, manual override control kit, D control

991-243
Red momentary/twist operation, extended resolution, manual override control kit, E control

Tritex II DC Linear & Rotary Actuators

No Compromises on Power, Performance or Reliability

With forces to approximately 950 lbs (4kN) continuous and 1,300 lbf peak (6 kN), and speeds to 33 in/sec (800 mm/sec), the DC Tritex II linear actuators also offer a benefit that no other integrated product offers– POWER! No longer are you limited to trivial amounts of force, or speeds so slow that many motion applications are not possible. And the new Tritex II with DC power electronics operates with maximum reliability over a broad range of ambient temperatures: -40°C to +65°C. The DC powered Tritex II actuators contain a 750 W servo amplifier and a very capable motion controller. With standard features such as analog following for position, compound moves, move chaining and individual force/ torque control for each move, the Tritex II Series is the ideal solution for most motion applications.

Tritex II Linear DC Actuator

Tritex II Models

- TDM standard mechanical capacity actuator, 60 and 75 mm
- TDX high mechanical capacity actuator, 60 and 75 mm
- RDM rotary motor, 60, 75 and 90 mm
- RDG rotary gearmotor, 60, 75 and 90 mm

Power Requirements

- DC Power 12-48 VDC nominal
- Connections for external braking resistor

Feedback Types

- Analog Hall with 1000 count resolution
- Incremental encoder with 8192 count resolution
- Absolute Feedback (analog hall with multi-turn, battery backup)

Connectivity

- Internal terminals accessible through removable cover (75 and 90 mm only)
- Threaded ports for cable glands (75 and 90 mm only)
- Optional connectors - M23 Power - M23 I/O
- M8 connector for RS485
- M12 connector for EtherNet options
- Custom connection options
- Embedded leads

Tritex II rotary motor with connectors shown left and Tritex II linear actuator with customer-supplied cable glands ports shown above.

Communications & I/O

Digital Inputs:

9 to 30 VDC Opto-isolated

Digital outputs:

30 VDC maximum
100 mA continuous output
Isolated
Short circuit & over temperature protected

Analog Input DC:

0-10V or +/-10V
0-10V mode, 12 bit resolution
+/-10V mode, 13 bit resolution
assignable to Position, Velocity, Torque or Velocity override command

Analog Output DC:

0-10V
11 bit resolution

IA 4 option

4-20 mA input
16 bit resolution
Isolated
Assignable to Position, Velocity, Torque or Velocity override command
4-20 mA output
12 bit resolution
Assignable to Position, Velocity, Current, Temperature etc

Standard Communications:

- 1 RS485 port, Modbus RTU, opto-isolated for programming, controlling and monitoring

Tritex II DC I/O

	60/75/90 mm frame with SIO, EIP, PIO, TCP	60/75/90 mm frame with IA4	60/75/90 mm frame with CAN
Isolated digital inputs	8	4	4
Isolated digital outputs	4	3	3
Analog input, non isolated	1	0	0
Analog output, non isolated	1	0	0
Isolated 4-20ma input	0	1	0
Isolated 4-20ma output	0	1	0

The IO count and type vary with acuator mode and option module selected.

All models include isolated digital IO, and an isolated RS485 communication port with using Modbus RTU protocol.

Manual Override Options

(Available on 75 & 90 mm linear and 75 & 90 mm rotary only, rotary not shown)

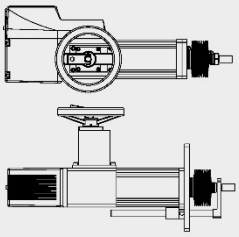

Handwheel
This option gives you a manual engagement switch that can be used to disable the power to the actuator for manual operation without any external tools.

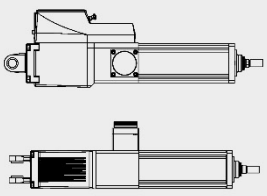

Side Drive
This option allows for emergency operation in a power down condition using a standard socket wrench.

RDM060/RDM075/RDM090 Rotary Actuator Speed vs. Torque Curves

RDM060	RDM075	RDM090

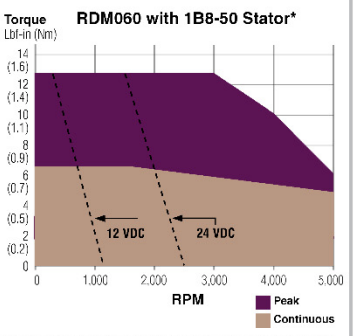

*Using NEMA recommended aluminum heatsink 10x10x1/4 in.

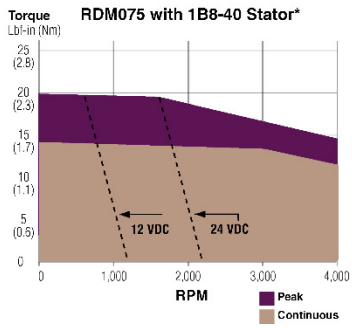

*Using NEMA recommended aluminum heatsink 10x10x3/8 in.

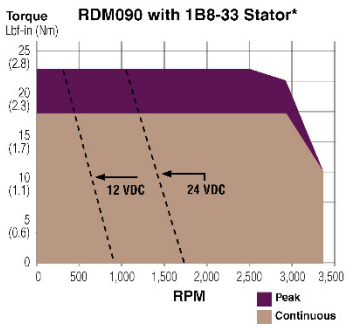

*Using NEMA recommended aluminum heatsink 10x10x3/8 in.

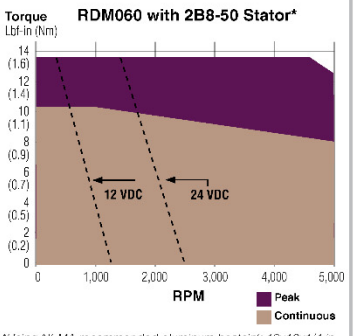

*Using NEMA recommended aluminum heatsink 10x10x1/4 in.

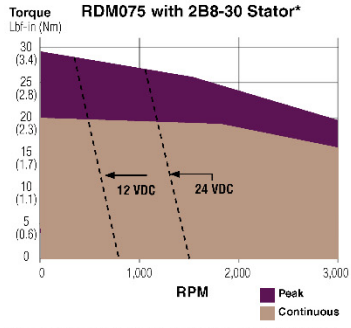

*Using NEMA recommended aluminum heatsink 10x10x3/8 in.

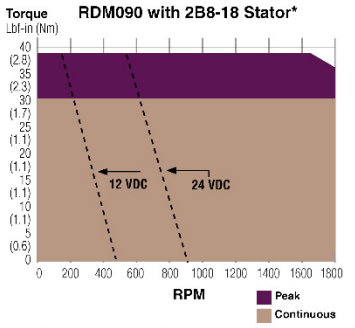

*Using NEMA recommended aluminum heatsink 10x10x3/8 in.

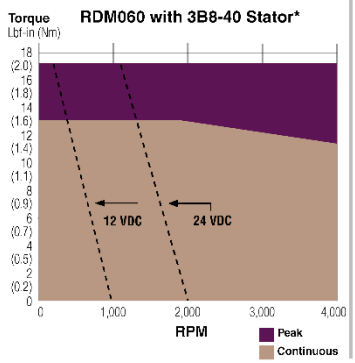

*RDM060 test data derived using NEMA recommended aluminum heatsink 10x10x1/4 in.

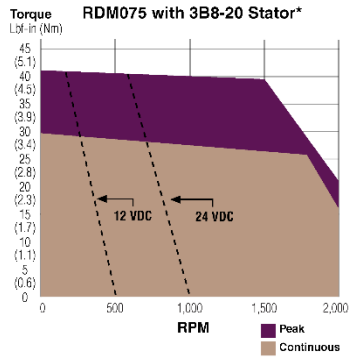

*RDM075 test data derived using NEMA recommended aluminum heatsink 10x10x3/8 in.

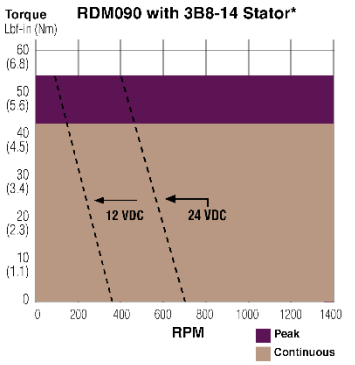

*RDM090 test data derived using NEMA recommended aluminum heatsink 10x10x3/8 in.

For RDG gearmotors, multiply torque by ratio and efficiency. Divide speed by gear ratio.

RDM/RDG060 Rotary Motor/Gearmotor Performance Specifications

RDM060 Rotary Motor Torque and Speed Ratings

	Stator	1 Stack 1B8-50	2 Stack 2B8-50	3 Stack 3B8-40
	RPM at 48 VDC	5000	5000	4000
Continuous Stall Torque	lbf-in (Nm)	6.8 (0.76)	10.5 (1.18)	13 (1.47)
Peak Stall Torque	lbf-in (Nm)	12.8 (1.44)	13.3 (1.5)	17 (1.92)
Drive Current @ Continuous Stall Force	Amps	14.8	21.5	21.5
Operating Temperature Range**	-20 to 65° C (-40°C available, consult Exlar)			
Maximum Continuous Power Supply Current*	Amps	8	11	13

*Power supply current is based on software current limit, not thermal limit. Consideration for peak current should also be considered when sizing power supplies.
For output torque of RDG gearmotors, multiply by ratio and efficiency. Please note maximum allowable output torques found at bottom of page.
**Ratings based on 40° C ambient conditions.

RDM/RDG060 Inertia

	Stator	1 Stack	2 Stack	3 Stack
RDM Motor Armature Inertia (+/-5%)	lb-in-sec² (kg-cm²)	0.000237 (0.268)	0.000413 (0.466)	0.000589 (0.665)
RDG Gearmotor Armature Inertia*	lbf-in-sec² (kg-cm²)	0.000226 (0.255)	0.000401 (0.453)	0.000576 (0.651)

*Add armature inertia to gearing inertia for total inertia.

Radial Load and Bearing Life

RPM	50	100	250	500	1000	3000
RDM060 lbf (N)	250 (1112)	198 (881)	148 (658)	116 (516)	92 (409)	64 (285)
RDG060 lbf (N)	189 (841)	150 (667)	110 (489)	88 (391)	70 (311)	48 (214)

Side load ratings shown above are for 10,000 hour bearing life at 25mm from motor face at given rpm.

RDG060 Gearmotor Mechanical Ratings

Model	Ratio	Maximum Allowable Output Torque-Set by User lbf-in (Nm)	Output Torque at Motor Speed for 10,000 Hour Life		
			1000 RPM lbf-in (Nm)	3000 RPM lbf-in (Nm)	5000 RPM lbf-in (Nm)
RDG060-004	4:1	603 (68.1)	144 (16.2)	104 (11.7)	88 (9.9)
RDG060-005	5:1	522 (58.9)	170 (19.2)	125 (14.1)	105 (11.9)
RDG060-010	10:1	327 (36.9)	200 (22.6)	140 (15.8)	120 (13.6)
RDG060-016	16:1	603 (68.1)	224 (25.3)	160 (18.1)	136 (15.4)
RDG060-020	20:1	603 (68.1)	240 (27.1)	170 (19.2)	146 (16.5)
RDG060-025	25:1	522 (58.9)	275 (31.1)	200 (22.6)	180 (20.3)
RDG060-040	40:1	603 (68.1)	288 (32.5)	208 (23.5)	180 (20.3)
RDG060-050	50:1	522 (58.9)	340 (38.4)	245 (27.7)	210 (23.7)
RDG060-100	100:1	327 (36.9)	320 (36.1)	280 (31.6)	240 (27.1)

Two torque ratings for the RDG gearmotors are given in the table above. The left hand columns give the maximum (peak) allowable output torque for the indicated ratios of each size RDG gearmotor. This is not the rated output torque of the motor multiplied by the ratio of the reducer.

It is possible to select a configuration of the motor selection and gear ratio such that the rated motor torque, multiplied by the gear ratio exceeds these ratings. It is the responsibility of the user to ensure that the settings of the system do not allow these values to be exceeded.

The right hand columns give the output torque at the indicated speed which will result in 10,000 hour life (L10). The setup of the system will determine the actual output torque and speed.

RDG060 Gearing Reflected Inertia

Single Reduction			Double Reduction		
Gear Stages	lbf-in-sec²	(kg-cm²)	Gear Stages	lbf-in-sec²	(kg-cm²)
4:1	0.0000132	(0.149)	16:1	0.0000121	(0.0137)
5:1	0.0000087	(0.00984)	20:1, 25:1	0.0000080	(0.00906)
10:1	0.0000023	(0.00261)	40:1, 50:1, 100:1	0.0000021	(0.00242)

Backlash and Efficiency

	Single Reduction	Double Reduction
Backlash at 1% Rated Torque	10 Arc min	13 Arc min
Efficiency	91%	86%

RDM060 Motor and RDG060 Gearmotor Weights

		RDM060 without Gears	RDG060 with 1 Stage Gearing	RDG060 with 2 Stage Gearing	Added Weight for Brake
1 Stack Stator	lb (kg)	3.0 (1.4)	7.5 (3.4)	9.3 (4.2)	.44 (.2)
2 Stack Stator	lb (kg)	4.1 (1.9)	8.6 (3.9)	10.4 (4.7)	
3 Stack Stator	lb (kg)	5.2 (2.4)	9.7 (4.4)	11.5 (5.2)	

RDM/RDG060 Rotary Motor/Gearmotor Dimensions

RDM060 Dimensions

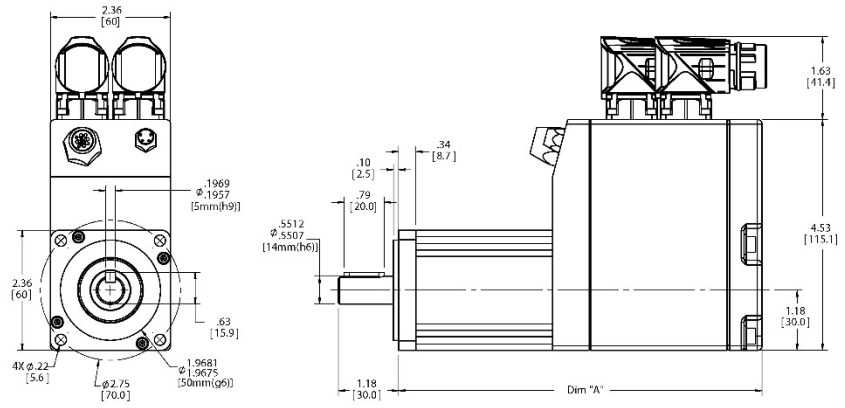

Without Brake Option			
DIM	1 Stack Stator	2 Stack Stator	3 Stack Stator
A	7.146 (185.1)	8.396 (213.3)	9.646 (245.0)

With Brake Option			
DIM	1 Stack Stator	2 Stack Stator	3 Stack Stator
A	7.856 (199.5)	9.106 (231.3)	10.356 (263.0)

RDG060 Dimensions

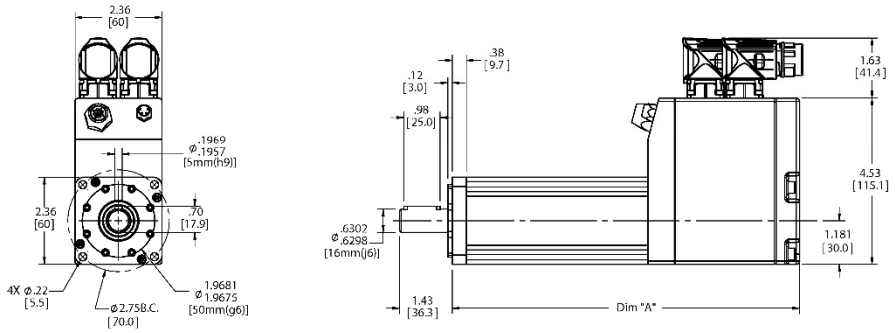

Without Brake Option			
DIM	1 Stack Stator 1 Stage Gearhead	2 Stack Stator 1 Stage Gearhead	3 Stack Stator 1 Stage Gearhead
A	9.434 (240)	10.684 (271)	11.934 (303)
DIM	1 Stack Stator 2 Stage Gearhead	2 Stack Stator 2 Stage Gearhead	3 Stack Stator 2 Stage Gearhead
A	10.479 (266)	11.729 (298)	12.979 (330)

With Brake Option			
DIM	1 Stack Stator 1 Stage Gearhead	2 Stack Stator 1 Stage Gearhead	3 Stack Stator 1 Stage Gearhead
A	10.144 (258)	11.394 (289)	12.644 (321)
DIM	1 Stack Stator 2 Stage Gearhead	2 Stack Stator 2 Stage Gearhead	3 Stack Stator 2 Stage Gearhead
A	11.189 (284)	12.439 (316)	13.689 (348)

Linear Actuator Ordering Guide

Tritex II DC TDM/X Linear Actuator Ordering Information

AAABBB-CCDD-EFG-HH-III-II-JJJ-KKK- (XX..XX - #####)

AAA = Actuator Type
TDM = Tritex II Linear Actuator, standard mechanical capacity
TDX = Tritex II Linear Actuator, high mechanical capacity

BBB = Actuator Frame Size
060 = 60 mm
075 = 75 mm

CC = Stroke Length
03 = 3 inch (76 mm)
06 = 6 inch (150 mm)
10 = 10 inch (254 mm)
12 = 12 inch (305 mm)
14 = 14 inch (356 mm) (75 mm only)
18 = 18 inch (457 mm) (75 mm only)

DD = Lead (linear travel per screw revolution)
01 = 0.1 inch (2.54 mm)
02 = 0.2 inch (5.08 mm)
04 = 0.4 inch (10.16 mm) (60 mm only)
05 = 0.5 inch (12.7 mm) (75 mm only)

E = Connections
G = Std Straight Threaded Port w/internal terminals, M20x1.5 (75 mm only)
N = NPT Threaded Port via Adapter with Internal Terminals, 1/2" NPT (75 mm only)
I = Intercontec Style - Exlar std, M23 Style Connector
B = Embedded Leads, 3 ft. std.
J = Embedded Leads, w/"I" plug, 3 ft. std.
X = Custom Connectivity

F = Mounting
B = Front & Rear Flange
C = Rear Clevis
G = Metric Rear Clevis
D = Double Side Mount
K = Metric Double Side Mount
E = Extended Tie Rod
M = Metric Extended Tie Rod
F = Front Flange
R = Rear Flange
S = Side Mount
J = Metric Side Mount
T = Side Trunnion
Q = Metric Side Trunnion
X = Special

G = Rod End
M = Male US Standard Thread[1]
A = Male Metric Thread[1]
F = Female US Standard Thread[1]
B = Female Metric Thread[1]
W = Male, US Standard Thread SS[10]
R = Male Metric Thread SS
V = Female US Standard Thread SS[10]
L = Female Metric Thread SS[10]
X = Special (please specify)

HH = Feedback Type
HD = Analog Hall Device
IE = Incremental Encoder, 8192 count resolution
AF = Absolute Feedback

III-II = Motor Stator, All 8 Pole
TDM/X060 Stator Specifications
1B8-50 = 1 Stack, 48 VDC, 5000 rpm
2B8-50 = 2 Stack, 48 VDC, 5000 rpm
3B8-40 = 3 Stack, 48 VDC, 4000 rpm[4]
TDM/X075 Stator Specifications
1B8-30 = 1 Stack, 48 VDC, 3000 rpm
2B8-30 = 2 Stack, 48 VDC, 3000 rpm
3B8-20 = 3 Stack, 48 VDC, 2000 rpm[4]

JJJ = Voltage
048 = 12-48 VDC

KKK = Option Board
SIO = Standard IO Interconnect
IA4 = 4-20 mA Analog I/O
COP = CANOpen
CON = CANOpen, non-connecdorized[9]
EIP = SIO plus Ethernet/IP with M12 connector
EIN = SIO plus Ethernet/IP without M12 connector[9]
PIO = SIO plus Profinet IO with M12 connector
PIN = SIO plus Profinet IO without M12 connector[9]
TCP = SIO plus Modbus TCP with M12 connector
TCN = SIO plus Modbus TCP without M12 connector[9]

X..XX = Travel and Housing Options (Multiples Possible)
Travel Options
AR = External Anti-rotate
PF = Preloaded Follower[2]
L1/2/3 = External Limit Switches[6]
RB = Rear Brake
SD = Manual Drive, Side Hex (75 mm)
HW = Manual Drive, Handwheel with Interlock Switch (TDX075 only)
PB = Protective Bellows[8]
SR = Splined Main Rod[7,10]
XT = Special Travel Options, high temp. bellows[8]
Housing Options
P5 = IP65 Sealed Housing (TDM only)
HC = Type III Hard Coat Anodized[3]
FC = White Epoxy Coating[3]
XH = Special Housing Option

Special Motor Options
XL = Special Lubrication[5]
XM = Special Motor Option

= Part Number Designator for Specials
Optional 5 digit assigned PN to designate unique model numbers

NOTES:
1. Chrome-plated carbon steel. Threads not chrome-plated.
2. The dynamic load rating of zero backlash, preloaded screws is 63% of the dynamic load rating of the std non-preloaded screws. The calculated travel life of a preloaded screw will be 25% of the calculated travel life of the same size and lead of a non-pre loaded screw.
3. This housing option may indidate the need for special material main rods or mounting.
4. Not available on 0.1" lead.
5. To achieve -40° C operating temperature, specify -XL in the actuator model mask and define Mobilgrease 28 in order notes. Other special lubricants are also available.
6. Limit switch option requires AR option.
7. This option is not sealed and is not suitable for any environment in which contaminants come in contact with actuator and may enter the actuator.
8. Not available with extended tie rod mounting option.
9. Requires customer supplied Ethernet cable through I/O port for Class 1 Div 2 compliance only.
10. Consult Exlar if ordering splined stainless steel main rod.

Rotary Motor and Gearmotor Ordering Guide

RDM/G AAABBB-CDEF-GG-HHH-HH-III-JJJ (XX...XX) - #####)

Tritex II DC RDM Motor or RDG Gearmotor Ordering Information

RDM/G = Motor Type
RDM = Tritex II DC Rotary Motor
RDG = Tritex II DC Rotary Gearmotor

AAA = Frame Size
060 = 60 mm
075 = 75 mm
090 = 90 mm

BBB = Gear Ratio
Blank = RDM
Single Reduction Ratios
004 = 4:1 005 = 5:1 010 = 10:1
Double Reduction Ratios (NA on 75 mm)
016 = 16:1 020 = 20:1
025 = 25:1 040 = 40:1
050 = 50:1 100 = 100:1

C = Shaft Type
K = Keyed
R = Smooth/Round
X = Special Shaft

D = Connections
G = Std straight threaded port w/internal terminals, M20x1.5 (75 & 90 mm only)
N = NPT threaded port internal terminals, 1/2" NPT (75 & 90 mm only)
I = Intercontec style – Exlar std, M23 Style Connector
B = Embedded Leads, 3 ft. std.
J = Embedded Leads, w/"I" plug, 3 ft. std.
X = Custom Connectivity

E = Housing Options
G = Exlar Standard
H = Type III Hard Coat Anodized
F = White Epoxy Coating
X = Special or Custom

F = Brake Option
S = No Brake, Standard
B = Electric Brake, 24 VDC

GG = Feedback Type
HD = Analog Hall Device
IE = Incremental Encoder, 8192 Count Resolution
AF = Absolute Feedback

HHH-HH = Motor Stators - All 8 Pole
RDM/G060 Stator Specifications
1B8-50 = 1 Stack, 48 VDC, 5000 rpm
2B8-50 = 2 Stack, 48 VDC, 5000 rpm
3B8-40 = 3 Stack, 48 VDC, 4000 rpm
RDM/G075 Stator Specifications
1B8-40 = 1 Stack, 48 VDC, 4000 rpm
2B8-30 = 2 Stack, 48 VDC, 3000 rpm
3B8-20 = 3 Stack, 48 VDC, 2000 rpm
RDM/G090 Stator Specifications
1B8-33 = 1 Stack, 48 VDC, 3300 rpm
2B8-18 = 2 Stack, 48 VDC, 1800 rpm
3B8-14 = 3 Stack, 48 VDC, 1400 rpm

III = Voltage
048= 12-48 VDC

JJJ = Option Board
SIO = Standard I/O Interconnect
IA4 = + 4-20 mA Analog I/O
COP = CANOpen
CON = CANOpen, non-connecdorized[2]
EIP = SIO plus EtherNet/IP with M12 connector
EIN = SIO plus EtherNet/IP without M12 connector[2]
PIO = SIO plus Profinet IO w/M12 connector
PIN = SIO plus Profinet IO without M12 connector[2]
TCP = SIO plus Modbus TCP w/M12 connector
TCN = SIO plus Modbus TCP without M12 connector[2]

XX = Special Travel and Housing Options (multiples possible)
HW = Manual Drive, Handwheel with Interlock Switch (75 & 90 mm only)
SD = Manual Drive, Side (75 & 90 mm only)
XH = Special Housing Options
XM = Special Motor Options
XL = Special Lubrication[1]

= Part Number Designator for Specials
Optional 5 digit assigned PN to designate unique model no.

NOTES:
1. To achieve -40° C operating temperature, specify -XL in the actuator model mask and define Mobilgrease 28 in order notes. Other special lubricants are also available.
2. Requires customer supplied Ethernet cable through I/O port for Class 1 Div 2 compliance only. Also N/A on 60 mm.

BULLETIN 3006-A

Magnatrol VALVE CORP.

BRONZE SOLENOID VALVES

Dependable • Packless

TYPE "A" FULL PORT - NORMALLY CLOSED
1/2" TO 3" PIPE SIZE

NO DIFFERENTIAL PRESSURE REQUIRED TO OPEN

MAX. FLUID TEMP.
212° F
MAX. STATIC PRESSURE
300 PSI
Except valves listed for 500 PSI

OPERATION:
Valve opens when energized and closes when de-energized. When the coil is energized the pilot valve opens, relieving the pressure above the piston, which is then lifted from its seat by the plunger. Upon de-energizing the coil, a spring closes the pilot valve and opens a bleed passageway to permit pressure to build above the piston and seat it.

CONSTRUCTION: (* Wetted parts)
*Valve Body - Cast Bronze, Globe Pattern - NPT ends
*Piston - Bronze
Coil Enclosure - Malleable or Cast Iron, 1/2" NPS conduit conn.
*Plunger - 430 Stainless Steel
*Pilot Valve - 303 Stainless Steel
*Bonnet Tube - 304 Stainless Steel
*Spring - 302 Stainless Steel
*Body Seal - Buna N or Non Asbestos Gasket
*Orifice Seal - Buna N (Viton or Glass Filled Teflon available)
*AC Shading Coil - Copper
*Stem Pin - Inconel
Coil - Encapsulated Class B, 18" leads - (Class H available)

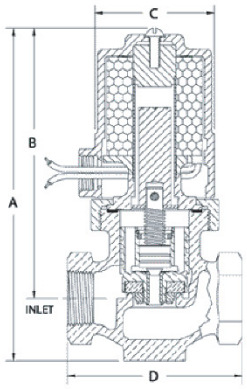

APPLICATION:
To control the flow of Water, Oil, Air, Gas, Solvents, Brine, Vacuum and any other fluids not reactive with construction materials and free of sediment. Valve operates from zero to maximum differential pressure indicated in table. Valve must be mounted in horizontal pipe with solenoid enclosure vertical and on top.

Pipe Size Inches	Max Diff. PSI	Type No.	Watts AC	Amps Hold 120-60	Amps Inrush 120-60	Watts DC	Ship Wt. Lbs.	Dimension In Inches				
								A	B	C	D	D(Flanged) 150#
1/2	110 200 300	18A42 18A32 18A52	25	0.4	1.2	18	8	7	5-7/8	2-3/4	3-1/4	4-3/4
	500	E33A62	45	0.8	2.4	23	16	8	6-7/8	4-1/8	3-1/4	N/A
3/4	50 110	18A23 18A43	25	0.4	1.3	18	8	7-1/8	6	2-3/4	3-1/2	5-1/2
	160	118A43	40	0.6	2.0	28						
	200 300	33A33 33A53	45	0.8	2.6	23	12	8-1/8	7	3-1/2	3-1/2	
	500	E133A63	65	1.2	3.9	33	17	8-1/8	7	4-1/8	3-1/2	N/A
1	50 110	18A24 18A44	25	0.4	1.5	18	10	7-7/8	6-5/8	2-3/4	4-1/8	5
	160	118A44	40	0.6	2.3	28						
	200 300	33A34 33A54	45	0.8	2.8	23	14	8-7/8	7-1/2	4-1/8	4-1/8	
	500	E133A64	65	1.2	4.2	33	19	8-7/8	7-1/2	4-1/8	4-1/8	N/A
1-1/4	50 90	18A25 18A45	25	0.4	1.6	18	12	8-3/8	6-3/4	2-3/4	4-1/2	7
	150	118A45	40	0.6	2.4	28						
	200 300	33A35 33A55	45	0.8	3.0	23	16	9-3/8	7-3/4	3-1/2	4-1/2	
	500	†† 40A65	60	1.2	6.2	N/A	20	10-3/8	8-3/4	4-1/2	4-1/2	N/A
1-1/2	50 115	35A26 35A46	45	0.8	3.2	23	20	10	8-1/8	4	4-7/8	7-3/4
	160	135A46	65	1.2	4.8	33						
	200 300	41A36 41A56	60	1.2	6.7	35	24	11	9-1/8	4-1/2	4-7/8	
	500	141A66	85	2.0	10.0	45						N/A
2	50 100	36A27 36A47	45	0.8	3.5	23	31	11	8-3/4	5-3/8	6	8
	150	136A47	65	1.2	5.0	33						
	200 300	42A37 42A57	60	1.2	7.4	35	36	12	9-3/4	5-3/4	6	
	500	142A67	85	2.0	11.0	45						N/A
2-1/2	50 125 200	43A28 43A48 43A38	60	1.2	8.0	35	43	12-7/8	10-1/8	5-7/8	7-1/4	11
	300	143A58	85	2.0	12.0	45						N/A
3	50 100 200	44A29 44A49 44A39	60	1.2	8.8	35	56	13-3/4	10-1/2	6-5/8	8-3/8	9-1/2
	300	144A59	85	2.0	13.0	45						N/A

FOR OPTIONS & ACCESSORIES SEE PAGES 26 & 27

Strainers are recommended for use with solenoid valves

(See page 19)

When you order please supply the following:

- Pipe Size
- Valve Type
- Voltage (AC or DC)
- Hertz
- Fluid
- Fluid Temperature
- Max. Diff. Pressure
- Optional Features

(See pages 26 & 27)

†† Not available for DC operation

MAGNATROL VALVE CORPORATION
8
Magnatrol Valve Corporation • P.O. Box 17 • 67 Fifth Avenue • Hawthorne • New Jersey • 07507
info@magnatrol.com • Phone: 973-427-4341 • Fax: 973-427-7611 • www.magnatrol.com

INDUSTRIAL FLOW SWITCHES

From 2 to 15 ft/s

FSW-50 Starts at **$180**

MADE IN USA RoHS

- **Rugged Industrial Design**
- **Switch Point Adjustable While Unit is Operating**
- **15 A SPDT Switch Directly Controls Pump**
- **Mounts in Any Position**

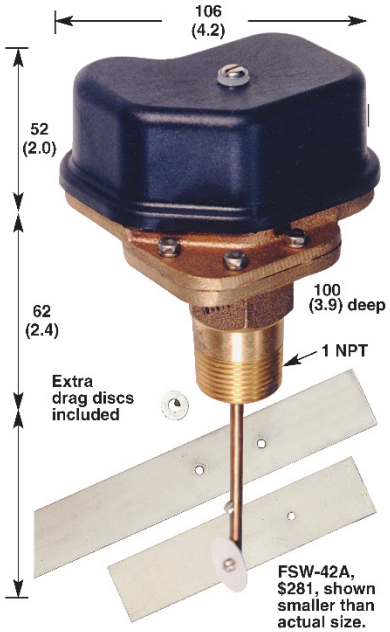

Dimensions:mm (in)
FSW-40A/41A: 38 (1.5)
FSW-42A: 89 (3.5)
FSW-43A: 140 (5.5)

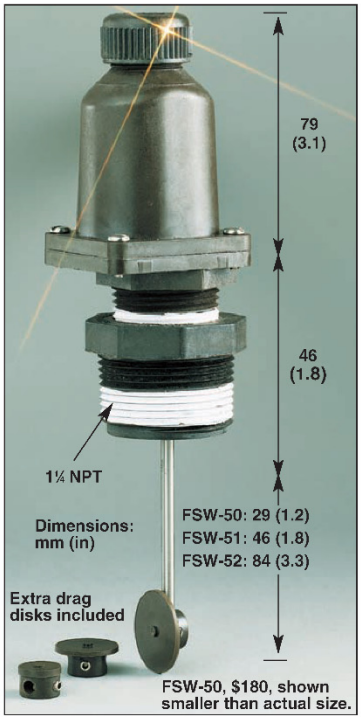

The FSW-40A and FSW-50 Series flow switches feature 15 A SPDT switches and an internal screw adjustment for in-line monitoring of switch points. Multiple drag disks provide incremental switch point adjustment. Their non-magnetic design makes these switches ideal for applications in which rust is a problem. The FSW-40A Series has a brass and stainless steel construction (optional 316 SS), while the FSW-50 Series comes in a plastic/316 SS construction.

The FSW-40A Series is ideal for machine-cutting oils and for sewage applications in which large objects are not caught on the drag disks. Installation "T" fittings are recommended for installing switches for 2" pipe size and below. For other pipe sizes, a "tee" fitting or weld coupling can be used.

SPECIFICATIONS

Relay Switch: SPDT 15 A @ 125 or 250 Vac; 10,000,000 operations median
Nominal Sensitivity (% Flow Change to Activate Switch):
10% @ upper end of range;
30% @ lower end of range
Pressure Drop: 1 to 3" pipe, less than 1 psi; 4" and above, negligible
Max Pressure/Temperature:
FSW-40A Series: 300 psig @ 82°C (180°F)
FSW-50 Series: 100 psig @ 93°C (200°F)
Min Temperature: 4°C (40°F)

Wetted Parts:
FSW-40 Series: Brass, 300 to 304 SS, phosphor bronze and EPDM and cork rubber (other materials are brass body, Noryl® cover, 300 SS and plastic hardware); also available with 316 SS, FKM, and PTFE

FSW-50 Series: Polyphenylene sulfide, 316 SS, FKM; also available with polyphenylene sulfide, Hastelloy C and FKM construction
Electrical Cable Fitting: Water resistant for cable diameters 0.250 ±0.025"
Weight:
FSW-40A Series: 1.59 kg (3.5 lb)
FSW-50 Series: 113 g (4.0 oz)

MOST POPULAR MODELS HIGHLIGHTED!

To Order *(Specify Model Number)*

Model No.	Price	No. of Extra Disks Included	For Pipe Sizes	Switch Point Adjustment Range (fps) Low	High
FSW-40A	**$281**	1	1"	2.0 to 6.0	5.0 to 15.0
FSW-41A	**281**	2	1½ to 2½"	2.0 to 6.0	5.0 to 15.0
FSW-42A	**281**	3	3 to 10"	2.0 to 6.0	5.0 to 15.0
FSW-43A	**281**	3	10 to 48"	2.0 to 6.0	5.0 to 15.0
FSW-50	**180**	1	1"	3.3 to 5.3	7.4 to 11.5
FSW-51	**180**	1	1½ to 2½"	2.7 to 5.4	5.4 to 10.8
FSW-52	**180**	1	3 to 10"	2.0 to 4.0	4.0 to 8.0
ME-0611	**215**	Reference Book: Fluid Mechanics Measurements			

Comes complete with operator's manual.
*For **FSW-40A** series with 316 SS, FKM and PTFE special construction, add suffix "**-SS**" to model number and **$179** to price.*
*For **FSW-50** series with polyphenylene sulfide Hastelloy C and FKM special construction, add suffix "**-HST**" to model number and **$33** to price.*
Ordering Examples: FSW-40A-SS, FSW-40A** flow switch with special 316 SS, FKM and PTFE construction, **$460.
FSW-42A** flow switch for 3 to 10" pipe **$281.

B-79